Tumor cell-intrinsic signals promoting tolerance and adaptation to oncogenic kinase inhibition

by

Cameron Timothy Flower
B.S.E., Biomedical Engineering
University of Connecticut, 2017

Submitted to the Program of Computational and Systems Biology
in Partial Fulfillment of the Requirements for the Degree of
Doctor of Philosophy in Computational and Systems Biology

at the

Massachusetts Institute of Technology

May, 2024

©2024 Cameron Timothy Flower. All rights reserved.
The author hereby grants to MIT a nonexclusive, worldwide, irrevocable, royalty-free license to exercise any and all rights under copyright, including to reproduce, preserve, distribute and publicly display copies of the thesis, or release the thesis under an open-access license.

Signature of Author.....
Cameron T. Flower
Computational and Systems Biology Graduate Program
May 14th, 2024

Certified by .....
Forest M. White, Ph.D.
Ned C. and Janet Bemis Rice Professor of Biological Engineering
Thesis Supervisor

Accepted by .....
Christopher B. Burge, Ph.D.
Professor of Biology
Co-Director, Computational and Systems Biology Graduate Program

Tumor cell-intrinsic signals promoting tolerance and adaptation to oncogenic kinase inhibition

by

Cameron Timothy Flower

Submitted to the Program of Computational and Systems Biology on May 14th, 2024, in Partial Fulfillment of the Requirements for the Degree of Doctor of Philosophy in Computational and Systems Biology

Abstract

Therapeutics targeting oncogenic kinases have offered longer survival and superior quality of life for cancer patients with particular malignancies compared to the preceding standard of care. However, many patients still fail to show a clinically meaningful response to kinase inhibitors prescribed on the basis of tumor genotype, and nearly all responsive patients eventually develop resistance, limiting the curative potential of these agents. A more complete understanding of the molecular basis underlying therapy failure is required for designing new agents and combinations with improved response rates. In this thesis, I explore these issues using tractable experimental models in which genotype-matched kinase inhibitors fail to kill or durably arrest proliferation of cancer cells, with particular focus on the role of cellular signaling networks.

In the first part, I have characterized a panel of human lung cancer cell lines harboring genetic gain-of-function alterations of clinically actionable tyrosine kinases (TKs). Using commonly prescribed TK inhibitors (TKIs), I show that TK genetic status generally predicts whether or not a cell line will show any response to genotype-matched TKI (GM-TKI), but is insufficient to predict *drug tolerance*, the ability of a cell line to sustain proliferation under drug. In drug combination experiments targeting co-mutated pathways, I show that some degree of tolerance to GM-TKI is explained by oncogenic co-mutations, but not across all lines. By leveraging targeted and untargeted mass spectrometry (MS) of endogenous tyrosine-phosphorylated proteins, which enables phosphosite-specific quantification of TK signaling networks, I report several cell line-specific vulnerabilities not predicted to exist at the genetic level, and the consensus observation that sustained activity of SRC family kinases (SFKs), or of the SRC-like kinases ABL1/2, is an important contributor to GM-TKI tolerance in all lines.

In the second part, I have examined the molecular events underlying drug-induced *adaptation*, the process by which drug exposure inadvertently drives upregulation of pro-survival signaling pathways. In a collaborative effort, we report the signaling and transcriptional dynamics underlying early adaptation to oncogenic BRAF inhibition in a patient-derived cell line model of human *BRAF*-mutant melanoma. We show by time-resolved MS of mitogenic signaling networks, computationally integrated with matched mRNA sequencing data, that adaptation to BRAF inhibition in our model system is promoted by early drug-induced compensatory SFK signaling, due in part to accumulation of reactive oxygen species via an impaired NRF2 antioxidant response. This concerted adaptive response promotes sensitivity to SFK inhibition across a panel of patient-derived *BRAF*-mutant melanoma cell lines and in a mouse xenograft model. The work described

in both parts was aided by two MS software solutions I developed: one to automate the generation of targeted acquisition methods for protein phosphosites and pathways of interest, and the other to retain quantitative information from fragment ion spectra with missing values.

Together, this thesis reports new connections between cell signaling and kinase inhibitor response, and offers the intriguing hypothesis that SFK signaling may be a conserved barrier for maximally effective targeted cancer therapy.

Thesis Supervisor: Forest M. White, Ph.D.
Title: Ned C. and Janet Bemis Rice Professor of Biological Engineering

Acknowledgements

I would like to thank my thesis advisor, Prof. Forest White, for his support, enthusiasm, affability, and – perhaps most importantly to me in retrospect – his patience. Early on in my training in his laboratory, when I wanted to change my project to focus on oncogenic signaling and cancer therapy, Forest didn't hesitate to help me chart a new course leading up to my qualifying exam. From this point on, I was grateful to be given a large degree of freedom to take my projects where I wanted, continually being reaffirmed that this is "my Ph.D." Over my six years in the lab, I spent many hours in Forest's office discussing fundamentals of cell signaling, mass spectrometry, and cancer therapy, during which he was patient enough to hear out my various notions about the science even when I was squarely wrong (which happened often). I learned a remarkable amount from these interactions, all of which – held in a friendly space where I could think out loud free of judgement – have made me a better scientist, communicator, and collaborator.

I want to thank my other thesis advisory committee members, Profs. Doug Lauffenburger and Michael Hemann, for agreeing to oversee my work and for their thoughtful feedback during committee meetings. Their previous work on drug resistance and collateral sensitivity in cancer therapy served as early inspiration for me, and I was fortunate to have their input and career guidance throughout my time at MIT. I would also like to thank Dr. Ryan Sullivan of Massachusetts General Hospital for serving on my thesis defense committee; I'm grateful for his clinical perspective on the basic science I report here.

I am indebted to all the members of the White Laboratory with whom I was very fortunate to overlap. Thanks to Drs. Nader Morshed, Ishwar Kohale, Jacqueline Gerritsen, and Antje Dittmann for teaching me phosphoproteomics and for being excellent role models to look up to early on in my training. Thanks to Dr. Lauren Stopfer for allowing me to contribute to the development of SureQuant, an exciting new technology for our field, as a first-year in the lab and for teaching me much in the process. Thanks to Dr. Jason Conage-Pough, alongside whom I learned the ropes of mass spectrometry, for countless fruitful discussions of cancer biology, experimental design, and video games over Domino's and Pit Bosses. Similarly, thanks to Drs. Ryuhjin Ahn, Tigist Tamir, and Sophie Herbst for imparting the wisdom of seasoned biologists onto this very unseasoned trainee. Thanks to Elizabeth Choe and Alicia D'Souza for the many deep conversations, often late into the light in the office, and for infusing such positivity into the group. Thanks to Do Hun (Sean) Kim for the good memories unwinding after hours. Thanks to Owen Leddy, Hui Yan (Jen) Kuang, Yufei Cui, Hannah Boyce, Bokai Song, and Weixi (Vincent) Kang for making me proud to have trained in such an upstanding lab environment. Thanks to the two MIT undergraduates I enjoyed co-supervising on a number of projects, Bridget Li and Joe Faraguna, for giving me the opportunity to step into a rewarding mentorship role during my time in the group.

I would like to thank Isadora Deese for her administrative support, routinely going above and beyond for the lab and fully enabling our terrific science. I would also like to thank Jacquie Carota for all her hard work keeping the CSB graduate program running smoothly.

I would like to thank the individuals I was fortunate to collaborate with over the course of my training. Dr. Chunmei Liu, Prof. Wei Wei, and Prof. James Heath of the Institute for Systems Biology carried out a large portion of the work described in Chapter 3, and without whom that effort would not have been possible. I gained valuable knowledge and perspective on systems biology, epigenetics, and scientific storytelling from our collaboration. I want to thank our collaborators at Thermo Scientific, whose support allowed us to develop powerful new targeted

mass spectrometry workflows and software: Drs. Bhavin Patel, Amirmansoor Hakimi, Aaron Gajadhar, Sebastien Gallien, Daniel Lopez-Ferrer, and Andreas Huhmer. Additionally, I want to thank the following collaborators for involving me in exciting projects not described in this thesis: Drs. Michael Oliphant and Senthil Muthuswamy (HMS); Prof. Benjamin Neel and Dr. Mitchell Geer (NYU); and Prof. Andrei Karginov and Dr. Mark Shaaya (UIC). Thanks to my former colleagues at BioNTech US, especially Dr. Michael Rooney, who gave me a fantastic industry internship experience in the summer of 2022.

I want to thank Prof. Chris Burge for his leadership of the CSB program and for teaching me how to properly read and opine on papers in CSB.100. Thanks to Dr. Victor-Emmanuel Brunel for breaking my fear of statistical rigor in 18.6501. Thanks to Profs. Tyler Jacks and Matt Vander Heiden for their leadership of the Koch Institute, a remarkable environment for PhD training, and for foundational 7.85 lectures that helped solidify my excitement for cancer research early on.

I owe an enormous debt of gratitude to all my close friends from MIT, UConn, NIH, and LSM High for their support in the years leading up to and during my Ph.D. There are too many names to list here, but these individuals know who they are. I want to give a special thanks to Dr. Patrick Lau, whose friendship and support since sharing a freshman dorm room over a decade ago has been a constant. I also would like to thank my former mentors for igniting my interest in research and for helping me get to where I am today: Prof. Pramod Srivastava, Prof. Sahar Al Seesi, Adam Hagymasi, and Tracy Hintz; Drs. Mark Knepper and Chin-Rang Yang; Prof. Ki Chon, Prof. Hugo Posada-Quintero, and Dr. Natasa Reljin; and Prof. Jaci Van Heest.

Finally, I would like to thank my family for their unwavering support and love. My many aunts, uncles, cousins, and grandparents – including Grandpa Rocc and Auntie Barb – cheered me on since the day I set foot on Mass Ave. My sister, Julia, brother-in-law, Jakub, and niece, Maya (our newest member of the family!), have given me endless smiles along the way. My mom and dad gave me all the tools and love I needed to get here from day one, and ask for none of the credit in return. I couldn’t have done this without you.

Table of Contents

List of Figures and Tables

Chapter 1:
Introduction

"Those who have not been trained in chemistry or medicine may not realize how difficult the problem of cancer treatment really is. It is almost – not quite, but almost – as hard as finding some agent that will dissolve away the left ear, say, and leave the right ear unharmed. So slight is the difference between the cancer cell and its normal ancestor."

William Woglom, Ph.D., 1945

Cancer treatment has come a long way. While surgery has remained a pillar of care for centuries, molecular approaches aimed at targeting the root causes of malignancy, hidden within the complexity of cancer cells, have only emerged over the last two decades and are still maturing. Just fifty years prior to the writing of this thesis, no one was aware of the existence of tyrosine kinases, oncogenes, or cellular signaling pathways; since that time, the remarkable pace of discovery in biology continues to inspire confidence that the full extent of cancer's challenges will be met in due course. In this thesis, I describe several new basic research efforts aimed at resolving the fundamental biology underlying two key limitations of today's targeted cancer therapies – drug tolerance and adaptation – in hopes of inspiring further preclinical characterization and potentially toward informing new therapeutic approaches. In this chapter, I will discuss some of the foundational concepts in cell signaling, cancer, and mass spectrometry which are regularly referenced throughout this thesis.

Chapter 1

Cell signaling: proteins and information flow through the cell

The ubiquitous role of proteins in cell biology

The cell is a remarkable innovation of nature. Sculpted by billions of years of dynamic evolutionary pressures, and more versatile and adaptable than the most advanced human technology, cells are the fundamental building blocks of all life on Earth. The conversion of sunlight to chemical energy in plants during photosynthesis, the secretion of pheromones from an insect to its colony in the presence of food, and the neural connections firing in your brain as you read these words, are all coordinated by cells of vastly distinct lineage and of highly specialized function. The cell owes its vast array of capabilities to the biochemical pathways contained within its plasma membrane; this circuitry is largely composed of networks of proteins, and the interactions between them keep the cell alive and allow it to carry out its prescribed functions.

Each protein, encoded by one of the many genes in its host cell (over 20,000 in humans), has a set of functions according to its structure, physiochemical properties, and subcellular localization. Membrane-embedded receptor proteins, for instance, protrude from the cell surface and allow cells to sense their environment and one another. As the structure, chemistry, or location of a given protein molecule changes, so too can its function; as an example, the estrogen receptor resides in the cytosol until it binds estrogen, at which point it translocates into the nucleus and binds DNA to activate the expression of particular target genes.[1] This general property of dynamic and context-dependent protein function is essential for all of cell biology, enabling cells and multicellular organisms to respond to their environment and changing circumstances.

Protein phosphorylation, kinases, and signaling cascades

One way a protein can undergo context-dependent changes to its structure, physiochemistry, or subcellular localization is by covalent modification of its constituent amino acids, an event known as post-translational modification (PTM). There are hundreds of distinct classes of PTMs known to researchers,[2] and likely many more remain undiscovered. The most ubiquitous PTM is phosphorylation, in which the γ-phosphate of adenosine triphosphate (ATP) is transferred to a serine, threonine, or tyrosine residue of the substrate protein (Figure 1.1). Kinases, the proteins responsible for catalyzing this transfer, play an outsized role in the biochemical regulation of the cell by altering the activity of the substrate protein. Enzymes which remove phosphate from proteins by hydrolysis are known as phosphatases; by antagonizing the effect of kinases, phosphatases are generally associated with downregulation of phosphoprotein signaling. The particular functional effect of phosphorylation is highly dependent on the specific amino acid being modified — for example, the MEK1 kinase can be phosphorylated at serine 218 and serine 222, canonically by the RAF-family kinases, and these phosphorylation events strongly promote

MEK1 activity due to their role in opening the kinase activation loop.[3] Following this event, active MEK1 signals to the serine/threonine kinases ERK1 and ERK2 by phosphorylating their activation loops. However, phosphorylation of MEK1 at threonine 286 or threonine 292, often by ERK1/2 and cyclin-dependent kinases (CDKs), constitutes a negative regulatory signal that leads to reduced MEK1 activity.[4] Thus, the phosphosite constitutes the lowest-level regulatory unit of cell signaling.

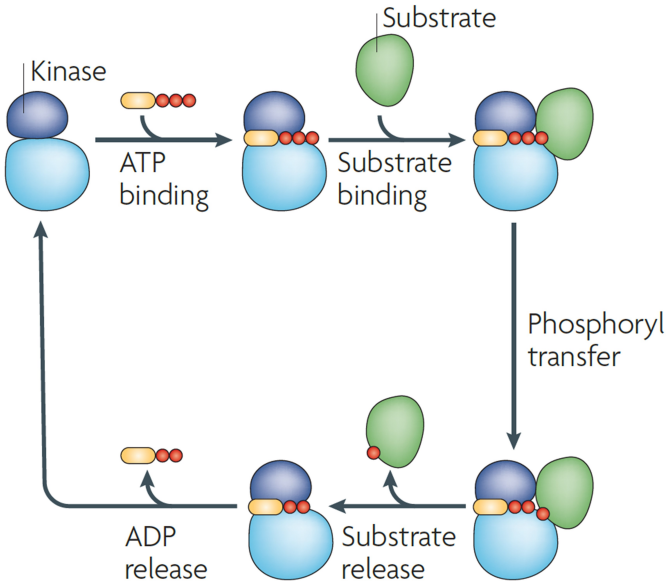

Figure 1.1. The basic mechanism of protein phosphorylation by kinases, taken from ref. 5

Signaling cascades

Together, the genes encoding kinases constitute one of the largest gene families in the human genome, and a subset of kinases are implicated in nearly every aspect of cell behavior. However, they rarely act in isolation of one another; indeed, a kinase can itself serve as a substrate for another kinase, which in turn may also be a substrate for a third upstream kinase, and so on. The resulting system, known as a signaling cascade (also commonly referred to as a signaling pathway or network), enables the flow of complex information through the cell. The earlier example of MEK1 and its phosphosite-specific regulation also invoked the notion of a signaling cascade, whereby MEK1 receives an activation signal from an upstream RAF-family kinase, which itself receives signal from RAS-family proteins in response to growth factor stimulation. MEK1 and the related kinase MEK2 transduce this signal onto ERK1 and ERK2, which serve as

"hub nodes" by phosphorylating hundreds of unique substrates to promote processes such as cell cycle progression, differentiation, and metabolism (Figure 1.2).[6,7]

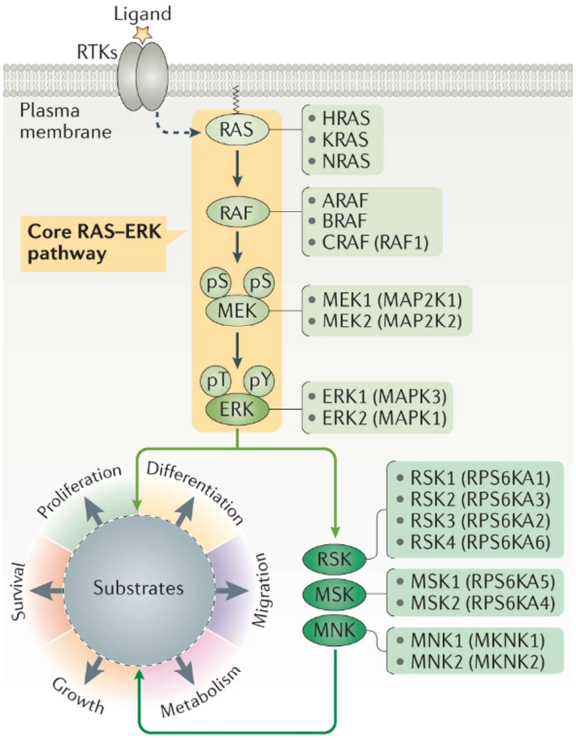

Figure 1.2. The RAS-ERK signaling pathway, taken from ref. 7

Cancer biology: signaling, vulnerabilities, and therapeutic challenges

Oncogenic signal transduction

Mitogenic signaling pathways, such as the RAS-ERK pathway, govern the growth of all dividing cells in the human body. Under normal homeostatic conditions, these systems are tightly regulated by phosphatases and feedback mechanisms, preventing cells from dividing inappropriately. However, if a cell acquires a mutation or epigenetic alteration that leads to heightened activation of RAS-ERK, such as a particular mutation in KRAS or epigenetic overexpression of an upstream receptor tyrosine kinase, the cell may undergo abnormally rapid proliferation. If left unchecked, this cell and its progeny can give rise to cancer. Sustained growth signaling is widely considered to be a so-called "hallmark of cancer";[8] it is thought to be a general feature shared by nearly all cancer types and instances, underscoring its broad importance in malignancy.

Kinase inhibitors and targeted cancer therapy

The importance of dysregulated mitogenic signaling in the initiation and progression of cancer has made kinases attractive drug targets for cancer therapy. The earliest success story in the targeted treatment of cancer using kinase inhibitors was the discovery of imatinib (Gleevec), an ATP-competitive tyrosine kinase inhibitor (TKI) targeting the BCR-ABL1 fusion protein present in nearly every case of chronic myeloid leukemia (CML).[9,10] Since its FDA-approval in 2001, imatinib and later-generation ABL1 inhibitors have transformed a cancer that was once considered a death sentence into a manageable chronic condition.

Beyond its clinical achievements for CML, imatinib inspired researchers to look for similar oncogenic dependencies in other cancer types. Throughout the 2000s and 2010s, efforts to drug hyperactive kinases implicated in the pathogenesis of lung cancer, melanoma, breast cancer, and several other cancer types were rewarded with compounds which outperformed the preceding standard of care in clinical trials. Today, we have over 70 FDA-approved kinase inhibitors for the treatment of many different cancers (Figure 1.3).[11]

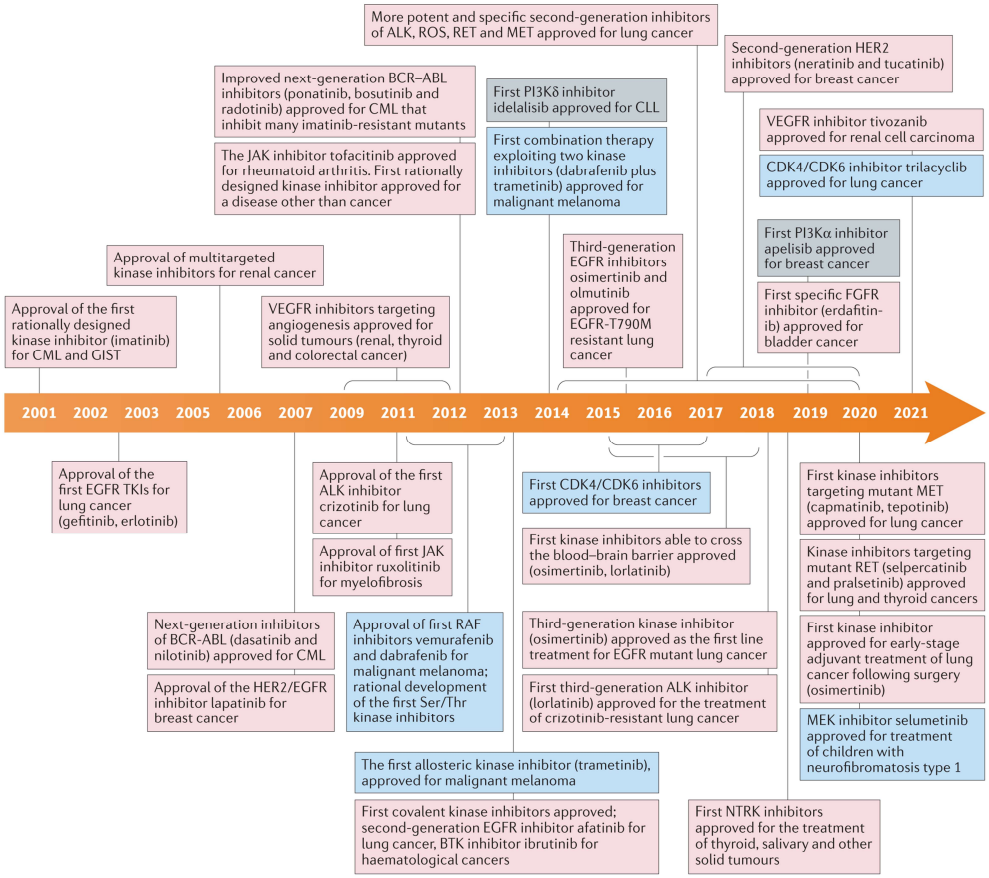

Figure 1.3. Timeline of kinase inhibitor development and approval since imatinib, taken from ref. 11

Therapeutic resistance

Unfortunately, despite the growing number of targeted therapies entering the oncology clinic in recent years, efforts to drug oncogenic kinases – particularly in solid tumors – have largely fallen short of reproducing the astounding clinical success of imatinib. While many patients have enjoyed longer survival and improved quality of life afforded by these drugs, a sizable proportion of patients still show no clinically meaningful response to targeted therapy prescribed on the basis of tumor genotype,[12,13,14,15,16,17] and nearly all responsive patients eventually develop acquired resistance to therapy.[18] We now know that treatment failure is a multifactorial problem stemming from factors including drug-induced adaptive responses and bypass signaling,[19,20] oncogenic co-mutations,[21] and intratumor heterogeneity.[22] However, our current understanding of the processes important for dictating the degree and durability of therapeutic response is incomplete; in particular, it remains unclear whether there are general biochemical mechanisms that confer sensitivity or resistance to therapy, and optimal treatment approaches to maximally sensitize tumors to oncogenic kinase inhibition have not yet been defined.

Mass spectrometry: a key enabling technology

Motivations for MS-based proteomics

To the extent that proteins are indispensable for cell biology, our approaches to detect and accurately quantify them remain equally important. A central technology permitting the analysis of cell-wide protein content, termed the "proteome", is mass spectrometry (MS). MS is an analytical approach that enables the characterization of complex samples of nearly any nature, including protein mixtures from whole-cell lysate or tissue homogenate, by ionizing the chemical constituents of the mixture and measuring their mass-to-charge ratios (*m/z*), which can be used to infer their identity. In cases where a single *m/z* measurement is not sufficient to unambiguously identify a chemical species, the ion may be fragmented and analyzed to produce a tandem (MS/MS) spectrum – akin to taking a specific fingerprint of the analyte. By analyzing complex protein mixtures using MS, researchers have gained valuable new insights into the regulatory roles of protein networks.[23,24]

Direct quantification of cell signaling by MS-based phosphoproteomics

MS applied to phosphoprotein mixtures, known as phosphoproteomics, is a powerful technique for the analysis of large-scale cell signaling networks. In this approach, proteins derived from cell lysate or tissue homogenate are denatured and digested with a protease, producing short peptides (often 10-30 amino acids in length) which are amenable to identification and quantitation by conventional MS. Prior to MS analysis, phosphorylated peptides are enriched using

chromatographic approaches[25] or immunoprecipitation[26], which depletes the highly complex background of non-phosphorylated protein to maximize the likelihood of phosphopeptide ionization and detection. Phosphopeptides are then injected into the mass spectrometer, and information about their identities and abundances are collected in MS/MS spectra. The resulting data can provide a highly detailed map of cell signaling dynamics, and new workflows and reagents are routinely improving the throughput, sensitivity, and quantitative accuracy of this powerful assay.[27]

Basics of MS data acquisition

There are many distinct types of MS instrumentation and architecture, each offering unique advantages for ascertaining the composition of a given sample. For quantification of proteomes – which consist of many thousands of distinct protein species and are therefore considered highly complex – high-resolution accurate mass (HRAM) MS is preferred for its ability to discern between peptides with extremely similar mass. A commonly used method of HRAM mass analysis for proteomics is the Orbitrap, which exploits a simple relationship between ion resonance frequency (ω) and mass-to-charge ratio (m/z):

$$\omega = \sqrt{\frac{k}{m/z}}$$

where k is a constant related to the field curvature within the Orbitrap.[28,29] Paired with the Fast Fourier Transform (FFT) algorithm, a powerful numerical procedure for inferring frequency spectra from mixed signals in the time domain, Orbitrap instruments are able to measure the *m/z* values of chemical species with a high degree of mass accuracy. Quadrupole-Orbitrap hybrid instruments are equipped with a quadrupole upstream of the Orbitrap mass analyzer, which allows the instrument to select ions of particular *m/z* for mass analysis (Figure 4).[30]

During a typical untargeted MS analysis of a mixture of peptides using a quadrupole-Orbitrap hybrid instrument, peptides are separated on the basis of hydrophobicity using a chromatographic gradient of an organic solvent, often acetonitrile, followed by ionization by electrospray ionization (ESI). Following ESI, peptide ions in the gas phase enter the mass spectrometer and are routed to the Orbitrap for mass analysis, at which point the instrument measures and records the *m/z* values and ion currents (or *MS intensities*) of all ions entering the instrument at that time, generating a *full MS* scan. From the full MS scan, the instrument then selects a predefined number of ions to individually isolate (using the quadrupole) and gently fragment (inside the HCD cell or ion routing multipole) using an inert gas, such as N_2. Fragment ions are then analyzed in the Orbitrap. The resulting spectrum, known as an *MS/MS scan*, depicts fragment ion *m/z* values and corresponding MS intensities for a given peptide ion; this spectrum

often contains sufficient information to unambiguously determine the peptide sequence and, in the case of phosphoproteomics, the position of its phosphorylation site(s). Fragment ions are also often used for peptide quantification, especially in the use of tandem mass tag (TMT) reagents for multiplexed relative quantitation. This entire process, known as *tandem MS*, is repeated thousands of times over the course of a typical 1-2 hour MS analysis, resulting in thousands of MS/MS scans for peptide identification and quantitation.

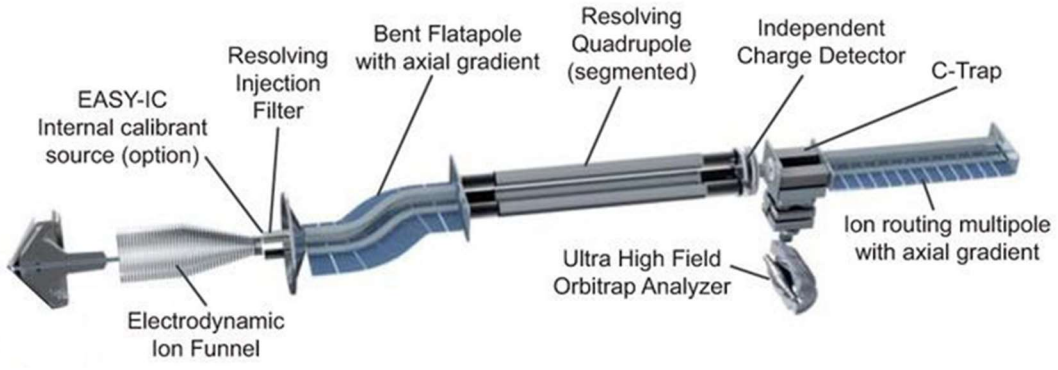

Figure 1.4. Architecture of the mass spectrometer used throughout this thesis (Thermo Scientific Orbitrap Exploris 480), taken from ref. 30

Peptide identification by MS requires that each peptide be amenable to ionization by ESI in order to be detected and fragmented. In a complex mixture of peptides, some may not adequately compete for charge during ESI and are not detected as a result. In addition, peptide ions must have *m/z* within a typical range (350-2000 is conventional) to be considered for fragmentation, and only peptides with relatively comprehensive fragmentation are likely to be identified. These restrictions – which are determined by peptide-specific physiochemical properties, the chemical background of the sample, and the MS acquisition setup and method – can limit which peptides are successfully identified and quantified in an MS-based phosphoproteomics experiment. Despite these limitations, MS-based phosphoproteomics offers multiple key advantages over alternative approaches; most notably is its ability to profile large-scale signaling networks in a hypothesis-free manner, requiring no prior knowledge of the relevant biology. The most widely-used alternative approach, western blot, depends on the selection of particular targets of interest *a priori*. Phosphoproteomics is amenable to both hypothesis-free and hypothesis-driven research via untargeted and targeted acquisition methods, respectively, making it a versatile tool for cell signaling research.[31,32] Additionally, phosphoproteomics affords the ability to accurately quantify cell signaling events, enabling multivariate statistical analyses and computational modeling. Immunoblot approaches are semi-quantitative at best, preventing deep mechanistic or data-driven

analysis. Another considerable limitation of western blotting is its heavy reliance on high-quality phosphosite-specific antibodies, which do not exist for the vast majority of the phosphoproteome. Using MS, phosphosite identification and quantitation is determined from fragmentation patterns recorded by the mass spectrometer, with no requirement for site-specific antibodies.

References

1. Fuentes N., Silveyra P. (2019). Estrogen receptor signaling mechanisms. Adv Protein Chem Struct Biol *116*, 135-170.
2. Khoury G.A., Baliban R.C., Floudas C.A. (2011). Proteome-wide post-translational modification statistics: frequency analysis and curation of the swiss-prot database. Sci Rep *1*, esrep00090.
3. Zheng C.F., Guan K.L. (1994). Activation of MEK family kinases requires phosphorylation of two conserved Ser/Thr residues. EMBO J *13*, 1123-31.
4. Rossomando A.J., Dent P., Sturgill T.W., Marshak D.R. (1994). Mitogen-activated protein kinase kinase 1 (MKK1) is negatively regulated by threonine phosphorylation. Mol Cell Biol *14*, 1594-602.
5. Ubersax J.A., Ferrell J.E. (2007). Mechanisms of specificity in protein phosphorylation. Nat Rev Mol Cell Biol *8*, 530-41.
6. Carlson S.M., Chouinard C.R., Labadorf A., Lam C.J., Schmelzle K., Fraenkel E., White F.M. (2011). Large-scale discovery of ERK2 substrates identifies ERK-mediated transcriptional regulation by ETV3. Sci Signal *4*, rs11.
7. Lavoie H., Gagnon J., Therrien M. (2020). ERK signalling: a master regulator of cell behaviour, life and fate. Nat Rev Mol Cell Biol *21*, 607-632.
8. Hanahan D., Weinberg R.A. (2000). The hallmarks of cancer. Cell *100*, 57-70.
9. Druker B.J., Tamura S., Buchdunger E., Ohno S., Segal G.M., Fanning S., Zimmermann J., Lydon N.B. (1996). Effects of a selective inhibitor of the Abl tyrosine kinase on the growth of Bcr-Abl positive cells. Nat Med *2*, 561-6.
10. Druker B.J., Talpaz M., Resta D.J., Peng B., Buchdunger E., Ford J.M., Lydon N.B., Kantarjian H., Capdeville R., Ohno-Jones S., et al. (2001). Efficacy and safety of a specific inhibitor of the BCR-ABL tyrosine kinase in chronic myeloid leukemia. N Engl J Med *344*, 1031-7.
11. Cohen P., Cross D., Jänne P.A. (2021). Kinase drug discovery 20 years after imatinib: progress and future directions. Nat Rev Drug Discov *20*, 551-569.
12. Soria J.C., Ohe Y., Vansteenkiste J., Reungwetwattana T., Chewaskulyong B., Lee K.H., Dechaphunkul A., Imamura F., Nogami N., Kurata T., et al. (2018). Osimertinib in Untreated EGFR-Mutated Advanced Non-Small-Cell Lung Cancer. N Engl J Med *378*, 113-125.
13. Paik P.K., Felip E., Veillon R., Sakai H., Cortot A.B., Garassino M.C., Mazieres J., Viteri S., Senellart H., Van Meerbeeck J., et al. (2020). Tepotinib in Non-Small-Cell Lung Cancer with MET Exon 14 Skipping Mutations. N Engl J Med *383*, 931-943.
14. Shaw A.T., Kim D.W., Mehra R., Tan D.S., Felip E., Chow L.Q., Camidge D.R., Vansteenkiste J., Sharma S., De Pas T., et al. (2014). Ceritinib in ALK-rearranged non-small-cell lung cancer. N Engl J Med *370*, 1189-97.
15. Soria J.C., Felip E., Cobo M., Lu S., Syrigos K., Lee K.H., Göker E., Georgoulias V., Li W., Isla D., et al. (2015). Afatinib versus erlotinib as second-line treatment of patients with advanced squamous cell carcinoma of the lung (LUX-Lung 8): an open-label randomised controlled phase 3 trial. Lancet Oncol *16*, 897-907.

16. Wolf J., Seto T., Han J.Y., Reguart N., Garon E.B., Groen H.J.M., Tan D.S.W., Hida T., de Jonge M., Orlov S.V., et al. (2020). Capmatinib in MET Exon 14-Mutated or MET-Amplified Non-Small-Cell Lung Cancer. N Engl J Med *383*, 944-957.
17. Shaw A.T., Bauer T.M., de Marinis F., Felip E., Goto Y., Liu G., Mazieres J., Kim D.W., Mok T., Polli A., et al. (2020). First-Line Lorlatinib or Crizotinib in Advanced ALK-Positive Lung Cancer. N Engl J Med *383*, 2018-2029.
18. Camidge D.R., Pao W., Sequist L.V. (2014). Acquired resistance to TKIs in solid tumours: learning from lung cancer. Nat Rev Clin Oncol *11*, 473-81.
19. O'Reilly K.E., Rojo F., She Q.B., Solit D., Mills G.B., Smith D., Lane H., Hofmann F., Hicklin D.J., Ludwig D.L., et al. (2006). mTOR inhibition induces upstream receptor tyrosine kinase signaling and activates Akt. Cancer Res *66*, 1500-8.
20. Niederst M.J., Engelman J.A. (2013). Bypass mechanisms of resistance to receptor tyrosine kinase inhibition in lung cancer. Sci Signal *6*, re6.
21. Skoulidis F., Heymach J.V. (2019). Co-occurring genomic alterations in non-small-cell lung cancer biology and therapy. Nat Rev Cancer *19*, 495-509.
22. Marusyk A., Polyak K. (2010). Tumor heterogeneity: causes and consequences. Biochim Biophys Acta *1805*, 105-17.
23. Zhang Y., Wolf-Yadlin A., Ross P.L., Pappin D.J., Rush J., Lauffenburger D.A., White F.M. (2005). Time-resolved mass spectrometry of tyrosine phosphorylation sites in the epidermal growth factor receptor signaling network reveals dynamic modules. Mol Cell Proteomics *4*, 1240-50.
24. Gerritsen J.S., White F.M. (2021). Phosphoproteomics: a valuable tool for uncovering molecular signaling in cancer cells. Expert Rev Proteomics *18*, 661-674.
25. Ficarro S.B., McCleland M.L., Stukenberg P.T., Burke D.J., Ross M.M., Shabanowitz J., Hunt D.F., White F.M. (2002). Phosphoproteome analysis by mass spectrometry and its application to Saccharomyces cerevisiae. Nat Biotechnol *20*, 301-5.
26. Salomon A.R., Ficarro S.B., Brill L.M., Brinker A., Phung Q.T., Ericson C., Sauer K., Brock A., Horn D.M., Schultz P.G., et al. (2003). Profiling of tyrosine phosphorylation pathways in human cells using mass spectrometry. Proc Natl Acad Sci U S A *100*, 443-8.
27. Li J., Cai Z., Bomgarden R.D., Pike I., Kuhn K., Rogers J.C., Roberts T.M., Gygi S.P., Paulo J.A. (2021). TMTpro-18plex: The Expanded and Complete Set of TMTpro Reagents for Sample Multiplexing. J Proteome Res *20*, 2964-2972.
28. Makarov A. (2000). Electrostatic axially harmonic orbital trapping: a high-performance technique of mass analysis. Anal Chem *72*, 1156-62.
29. Zubarev R.A., Makarov A. (2013). Orbitrap mass spectrometry. Anal Chem *85*, 5288-96.
30. Bekker-Jensen D.B., Martínez-Val A., Steigerwald S., Rüther P., Fort K.L., Arrey T.N., Harder A., Makarov A., Olsen J.V. (2020). A Compact Quadrupole-Orbitrap Mass Spectrometer with FAIMS Interface Improves Proteome Coverage in Short LC Gradients. Mol Cell Proteomics *19*, 716-729.
31. Wolf-Yadlin A., Hautaniemi S., Lauffenburger D.A., White F.M. (2007). Multiple reaction monitoring for robust quantitative proteomic analysis of cellular signaling networks. Proc Natl Acad Sci U S A *104*, 5860-5.

32. Curran T.G., Zhang Y., Ma D.J., Sarkaria J.N., White F.M. (2015). MARQUIS: a multiplex method for absolute quantification of peptides and posttranslational modifications. Nat Commun *6*, 5924.

Chapter 2:
Resolving and exploiting tumor cell-intrinsic signals associated with clonal tolerance to oncogenic tyrosine kinase inhibition

Tyrosine kinase inhibitors (TKIs) are an important therapeutic modality in the treatment of certain cancers, but many patients exhibit an underwhelming response to TKIs prescribed on the basis of tumor genotype. Here, we describe an experimental model system consisting of established non-small cell lung cancer cell lines, each harboring genetic alteration of one of three actionable tyrosine kinases (TKs), and report significant variability in their response to genotype-matched TKIs (GM-TKIs). To examine the molecular basis for tolerance to GM-TKI exposure and nominate alternate signaling axes for co-inhibition, we analyzed the mutations and TK signaling networks in each cell line. We found that oncogenic co-mutations in PI-3-kinase (PI3K) explain some degree of drug tolerance in a subset of lines. Mass spectrometry-based tyrosine phosphoproteomics (pY-MS) revealed several cell line-specific drivers of tolerance, including residual or sustained activity of EGFR and MEK1/2, and showed that high activity of SRC family kinases (SFKs) or the SRC-like kinases ABL1/2 is a shared feature among all drug-tolerant lines. SFK/ABL inhibition was synergistic with GM-TKI and led to durable cell cycle arrest or cell death in all lines. Our findings demonstrate the utility of pY-MS in resolving determinants of sensitivity and tolerance to TKI therapy and suggest that high basal SFK/ABL activity may broadly contribute to TKI tolerance.

Chapter 2

Introduction

Recognition of the oncogenic potential of tyrosine kinases (TKs), beginning with the seminal discovery of *v-Src* and culminating in the landmark identification of *BCR-ABL1* as a highly effective drug target in chronic myeloid leukemia, has placed great emphasis on the role of TK signaling in cancer initiation and progression.[1,2,3,4,5,6] As a result, dozens of TK inhibitors (TKI) are now approved in the U.S. and globally for the clinical management of multiple cancer types, constituting the largest class of molecular targeted therapies.[7] While these drugs have afforded many patients longer survival and higher quality of life compared to the preceding standard of care, response rates for even the most advanced agents still fall far short of 100% (often ranging from 40-80%[8,9,10,11,12,13]), and our understanding of the biological determinants underlying poor initial response to TKI therapy is incomplete.

Tumor cell-intrinsic signaling networks play an important role in targeted therapy response, in large part by dictating the activity of – and by extension, the dependency on – the intended drug target and its downstream pathways; for example, TKI treatment may fail to arrest the growth of tumor cells in which mitogenic signaling can be sustained by an alternate TK.[14] Under sustained drug treatment, drug-tolerant tumor cells can continue evolving toward more aggressive states, in some cases aided by drug-induced hypermutagenic processes,[15,16] emphasizing the importance of early rational intervention in delaying or preventing acquired resistance and aggressive malignancy.

In non-small cell lung cancer (NSCLC), alterations in genes encoding particular receptor TKs (RTKs) are widely recognized driver events and are associated with response to corresponding inhibitors.[12,17,18,19] These qualities have propelled the use of NSCLC-based model systems for the study of general principles of TKI response, extending beyond explicit efforts to improve outcomes in thoracic oncology.[16,20] In this work, we leveraged an experimental model system to investigate the cellular response resulting from inhibition of MET, ALK, and EGFR – three clinically actionable RTKs in the setting of NSCLC and several other cancers. In the clinic, sequencing efforts have found that *MET* gene alterations are observed in approximately 7% of NSCLC patients, most of which consist of genetic amplification or variants that cause inappropriate splicing of exon 14, resulting in impaired negative regulation of the receptor (Figure 2.1).[21] *ALK* alterations occur in 6-7% of NSCLC patients and predominantly involve fusion with the *EML4* gene, producing the EML4-ALK fusion protein which self-oligomerizes in the cytosol and constitutively activates mitogenic pathways.[22,23] *EGFR* mutations, which are largely mutually exclusive with alterations in *MET* and *ALK*, are observed in over a quarter of NSCLC patients and most commonly consist of gain-of-function kinase domain mutations (such as L858R or partial exon 19 deletion), copy number gain, or both.[25] In our model system, established NSCLC cell lines

were paired with FDA-approved TKIs matched on the basis of their mutation status for these three important RTKs (Figure 2.2).

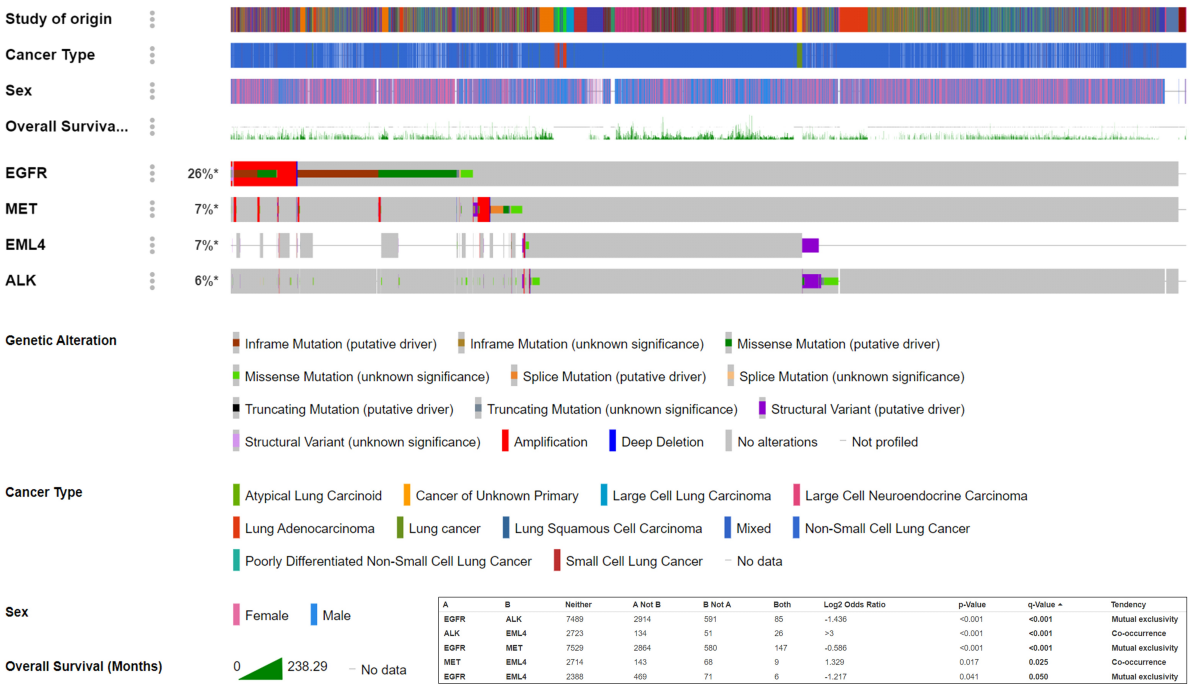

Figure 2.1. Frequencies of common genetic TK alterations implicated in NSCLC
Genetic and clinical data from 9,792 patients collected across 25 clinical sequencing studies. Data were visualized using the cBioPortal.[24]

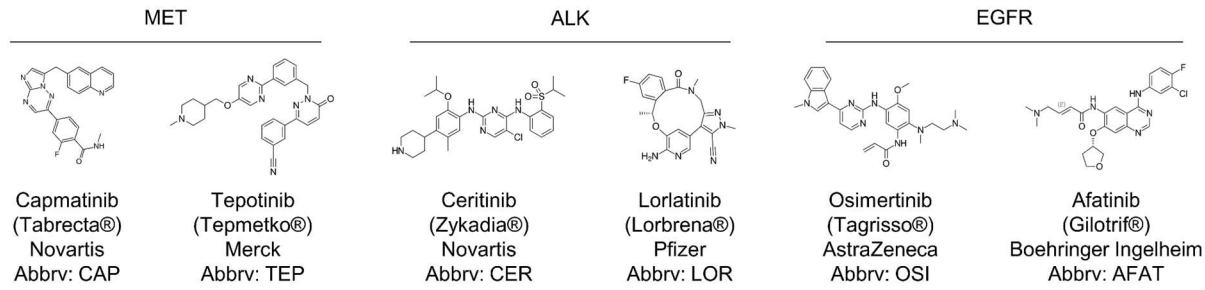

Figure 2.2. FDA-approved TKIs used throughout this study
Chemical structures of TKIs used throughout this study, all of which are commonly used for clinical management of NSCLC. Throughout this work, each drug is referred to using the abbreviation shown, except when being referred to collectively as GM-TKIs.

Results

Assembly and characterization of a panel of oncogenic TK-expressing NSCLC cell lines

To examine the role of TK signaling networks in mediating cellular sensitivity or tolerance to TKI treatment, we assembled a panel of established NSCLC cell lines harboring genetic gain-of-function alterations in the TKs MET, ALK, and EGFR according to the Cancer Dependency Map (DepMap),[26] with two cell lines for each TK (Table 2.1). Under treatment with multiple genotype-matched TKIs (GM-TKIs), we verified that oncogenic TK status is predictive of whether or not a cell line will show any degree of sensitivity within range of the reported IC_{50} for the intended drug target (Figures 2.3A – 2.3C). One notable exception was the response of H1993 to AFAT, an inhibitor of mutant EGFR. Given that AFAT also inhibits wild-type EGFR and other ERBB family members at nanomolar concentration, this result may suggest some degree of dependency on these targets for proliferative signaling in H1993. AFAT also resulted in a more potent reduction in viability in HCC4006 compared to H1975, consistent with its lower activity against $EGFR^{T790M}$.[27]

Cell line	NSCLC subtype of origin	Actionable TK	Oncogenic alteration (DepMap)
H1993	Adenocarcinoma	MET	Amplification
EBC-1	Squamous cell carcinoma	MET	Amplification
H2228	Adenocarcinoma	ALK	*EML4* fusion Variant 3a ($EML4^{M1\text{-}Q222}$-$ALK^{V1058\text{-}P1620}$) Variant 3b ($EML4^{M1\text{-}Q233}$-$ALK^{V1058\text{-}P1620}$)
H3122	Adenocarcinoma	ALK	*EML4* fusion Variant 1 ($EML4^{M1\text{-}K496}$-$ALK^{V1058\text{-}P1620}$)
H1975	Adenocarcinoma	EGFR	Kinase domain mutation (L858R / T790M)
HCC4006	Adenocarcinoma	EGFR	Kinase domain mutation (ΔL747-E749 / A750P)

Table 2.1: Characteristics of NSCLC cell lines used in this study

Though each TK-altered line showed some degree of response to GM-TKI, we noted that for each pair harboring a given oncogenic TK, the two lines displayed a noticeable difference in dose-response. Direct comparison of viability dose-responses between cell lines is challenging due to differences in basal growth rate, which can confound quantification of drug sensitivity.[28] We therefore used time-resolved clonogenic assays by crystal violet cell staining as an orthogonal qualitative approach, and found that each pair of cell lines consisted of one drug-sensitive line

(DSL), which was durably arrested or killed by a moderate (1 μM) dose of GM-TKI, and one drug-tolerant line (DTL), which continued proliferating under drug (Figures 2.3D – 2.3F). A 12-day period of drug washout after an initial 12-day period of exposure confirmed that DSLs underwent significant cell death under GM-TKI, and revealed several instances of subclonal drug tolerance resulting in colony formation from rare surviving cells, which are often termed drug-tolerant persisters (DTPs).[29,30] All DTLs, however, displayed remarkable clonality in their ability to survive and cycle under drug. These properties motivated the use of this cell line panel to identify molecular contributors to poor response to GM-TKI. To distinguish this work from previous studies specifically examining the biology of DTPs, throughout this work we use the term drug tolerance to refer specifically to clonal drug tolerance; we also distinguish drug tolerance from drug resistance, the latter referring strictly to complete insensitivity (e.g. all *MET*-diploid lines under MET inhibition) in this work.

Poor sensitivity to targeted therapy is commonly attributed to low activity of the intended drug target, resulting in reduced cellular dependency on the target for proliferation or survival. To test whether basal activity of each oncogenic TK was sufficient to explain differential sensitivity to GM-TKI, we aimed to quantify the activity of each target across all cell lines by targeted mass spectrometry (MS) of tyrosine-phosphorylated peptides derived from each drug target. Targeted MS requires construction of an acquisition method that provides a list of peptide ions of interest, and the mass-charge ratio (*m/z*) of each, to the mass spectrometer.[31] To facilitate the generation of this list given any set of phosphosites of interest, we designed a user-friendly software tool that maps phosphosites to the corresponding source proteome (for example, all sequences from *Homo sapiens* curated by UniProt/SwissProt[32]), performs an *in silico* digest of these proteins to extract the tryptic phosphopeptide sequence supporting each phosphosite, calculates the corresponding *m/z* values, and returns these values in a precursor ion inclusion list suitable for targeted MS (Figure 2.4A). Our software also returns a FASTA-formatted database containing all targeted peptide sequences, which can be used for peptide identification following MS.

Using our targeted MS acquisition software, paired with tandem mass tag (TMT) reagents for relative phosphopeptide quantification, we quantified basal tyrosine phosphorylation of MET, EML4-ALK, EGFR, and the downstream mitogenic kinases MAPK1 and MAPK3 (commonly known as ERK2 and ERK1, respectively) in all cell lines (Figures 2.4B and 2.4C; see Appendix A for methods details). We confirmed that for each oncogenic TK, activity was usually highest in the cell lines with a genetic alteration of the TK; one exception was H1975, which showed lower EGFR activity compared to the *MET*-amplified H1993 and EBC-1 lines – potentially due to "crosstalk" between MET and EGFR[33,34] – a finding that is consistent with the partial sensitivity of H1993 to AFAT. There was no strong association between oncogenic TK activity and downstream activity of MEK1/2, the endogenous kinases of ERK1/2. We also observed distinct

trends between different phosphosites on the same protein, highlighting the distinct regulatory roles of phosphosites[35,36] and underscoring the importance of phosphosite-specific quantification in the analysis of cell signaling. In the case of EML4 phosphosites in H2228 and H3122, these distinct trends are consistent with known differences in EML4-ALK isoform expression between these two lines.[37]

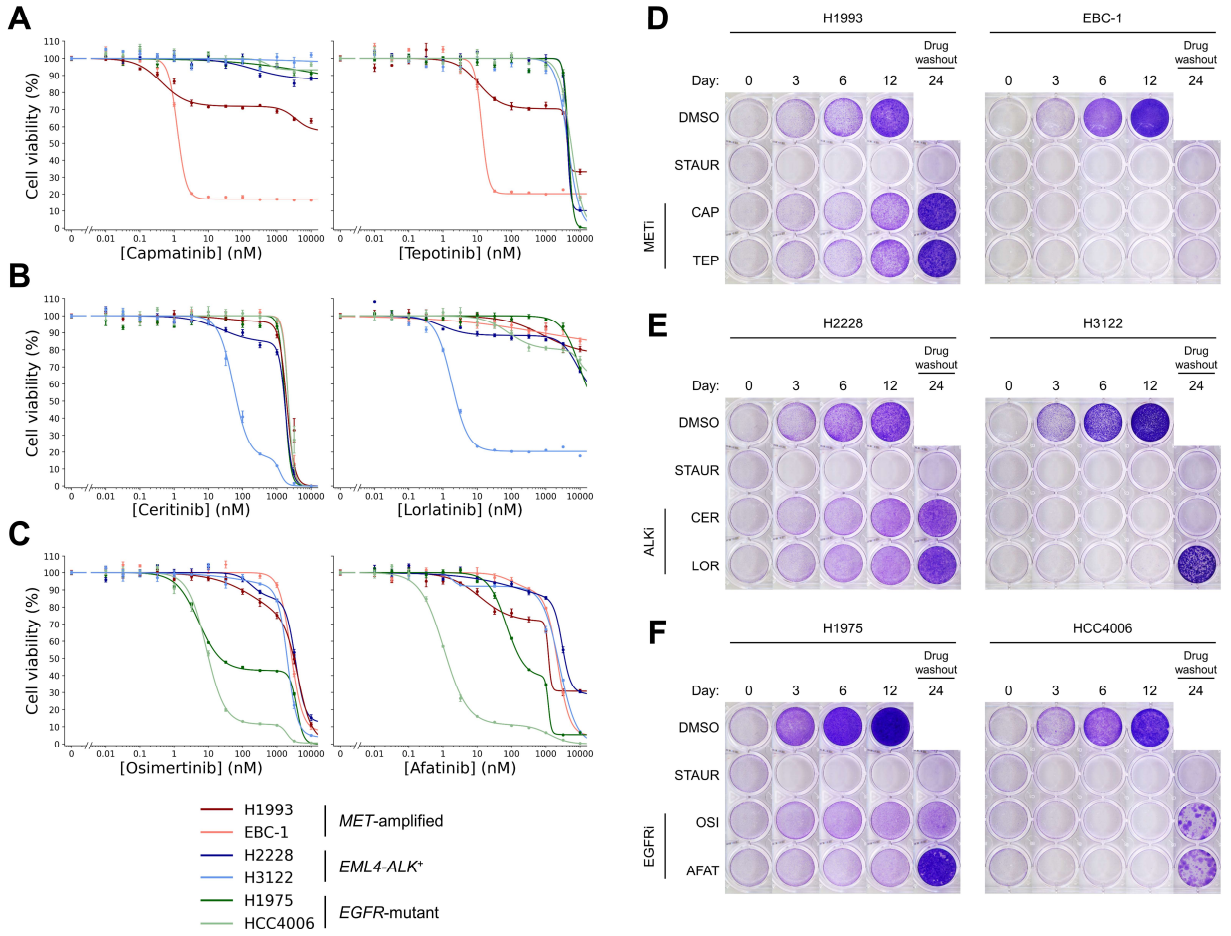

Figure 2.3. Viability response of NSCLC cell lines to GM-TKI

A. Viability dose responses of *MET*-amplified cell lines to MET inhibitors CAP and TEP, measured 72 hours after treatment.
B. Viability dose responses of *EML4-ALK*$^{+}$ cell lines to ALK inhibitors CER and LOR.
C. Viability dose responses of *EGFR*-mutant cell lines to EGFR inhibitors OSI and AFAT.
D. Clonogenic assay of *MET*-amplified cell lines treated with 1 μM of MET inhibitors CAP or TEP, or control compound dimethyl sulfoxide (DMSO) at 0.1% (v/v). 10 μM staurosporine (STAUR), a nonspecific kinase inhibitor with broad cytotoxic activity, was used as a positive control for cell death.
E. Clonogenic assay of *ALK*-rearranged cell lines treated with 0.1% DMSO or 1 μM of ALK inhibitors CER or LOR.
F. Clonogenic assay of *EGFR*-mutant cell lines treated with 0.1% DMSO or 1 μM of EGFR inhibitors OSI or AFAT.

In *MET*- and *EGFR*-altered cell lines, we found that basal target activity was higher in each DSL compared to the corresponding DTL, while this was not the case for *ALK*-rearranged lines (Figure 2.4C). This result suggests that basal drug target activity, like TK mutation status, can be an informative yet imperfect predictor of drug response.

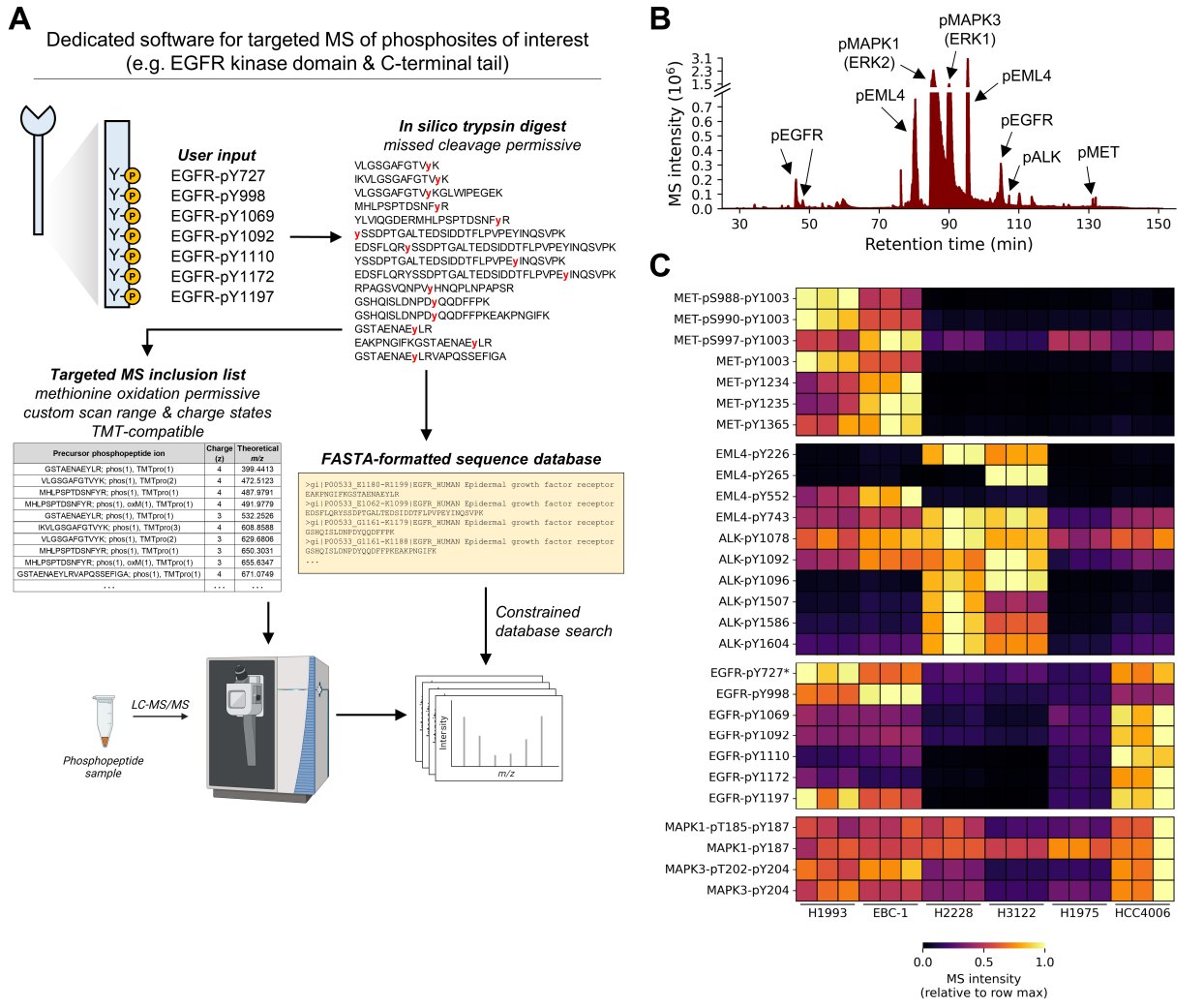

Figure 2.4. Targeted MS analysis of oncogenic TK activity in NSCLC cell lines

A. Workflow schematic detailing the pipeline of an automated software approach for construction of targeted MS acquisition methods from a user-defined set of phosphosites of interest.

B. Chromatogram of the phosphotyrosine immonium ion (m/z = 216.04257, ±10 ppm) in a targeted MS analysis of oncogenic TKs in NSCLC cell lines.

C. Heatmap depiction of the abundances of tyrosine phosphosites on MET, EML4-ALK, EGFR, and the downstream kinases MAPK1/3 (ERK2/1) in NSCLC cells lines, assayed by targeted MS using tandem mass tags (TMT). Abundances are normalized to the maximum value in each row.
*The tryptic phosphopeptide supporting EGFR-pY727 also maps to two other paralogous ERBB family members (ERBB2-pY735 and ERBB4-pY733).

Oncogenic co-mutations in PI3K contribute to drug tolerance in a subset of DTLs

In addition to reduced target activity, another common explanation for tolerance to single-agent targeted therapy is the presence of oncogenic co-mutations, which may reduce the cellular dependency on the intended drug target.[38] Using the DepMap, we found that the DTLs H1993 and H1975 both harbor a mutation in a catalytic domain of the mitogenic phosphoinositide 3-kinase (PI3K), one of which (PIK3CA^{G118D} in H1975) is oncogenic according to OncoKB[39] (Figures 2.5A and 2.5B). The other mutation (PIK3CD^{E320D} in H1993) is not known to be oncogenic; however, mutation of the nearby N334 residue (N334K) is likely oncogenic according to the DepMap, suggesting that E320D may also be a gain-of-function variant.

Figure 2.5. PI3K mutations in H1993 and H1975 and their oncogenic potential

A. PI3K mutations in H1993 and H1975 as reported by the DepMap.
B. The oncogenic potential of PI3K mutations in H1993 and H1975 as reported by OncoKB.

To test whether these PI3K mutations may contribute to drug tolerance, we paired GM-TKI with PI3K inhibitors and performed a checkerboard assay to screen for dose combinations that may show a synergistic effect. We used alpelisib (ALP), an inhibitor of the p110α subunit of PI3K encoded by the PIK3CA gene, and pictilisib (PIC), which has high activity against p110α

and p110δ (encoded by PIK3CD), and moderate activity against the catalytic subunits of other PI3K family members (Figure 2.6A). Cells were treated in a conventional format that allows for detection of dose-resolved drug interactions, including synergy, independence, and antagonism (Figure 2.6B; see Appendix A for methods details). We observed moderate synergy between GM-TKI and PI3K inhibition, suggesting some degree of interaction between PI3K and the co-expressed oncogenic TK (Figures 2.6C and 2.6D). However, the only dose combinations that resulted in widespread cell death were observed at doses much greater (10 μM) than the reported IC_{50} values for their intended targets,[40,41] indicating that these drug combinations are insufficient to kill within 3 days when acting solely through their intended mechanism of action.

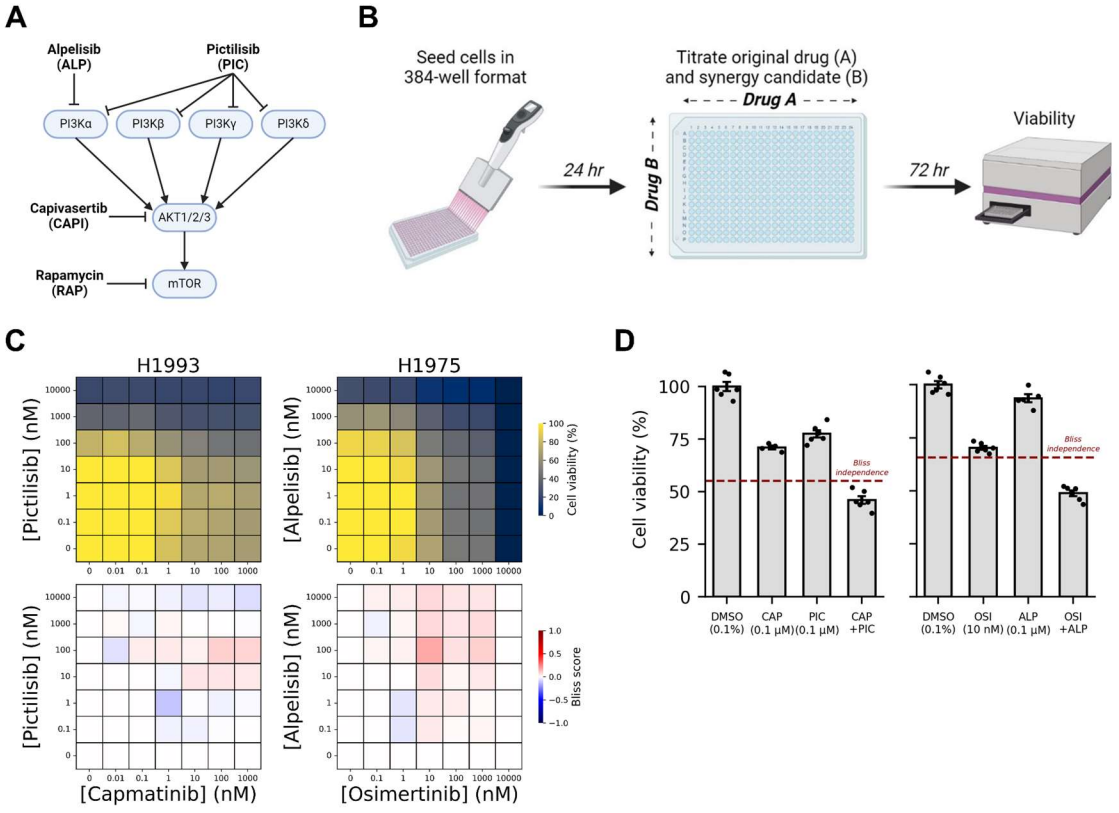

Figure 2.6. Examining the role of PI3K co-mutations in GM-TKI tolerance by drug combination experiments

A. Pathway schematic depicting the targets of inhibitors used in the experiments depicted in this figure and in Figure 2.7.
B. Experimental schematic for all checkerboard assays used in this study.
C. Dose-response matrices (top) and Bliss synergy matrices (bottom) from checkerboard assays pairing GM-TKI with PI3K inhibitors in H1993 (left) and H1975 (right) cells. Treatment duration was 72 hours.
D. Viability of H1993 (left) and H1975 (right) cells under the most synergistic combination of drugs depicted in (C).

Checkerboard assays can inform about short-term response to drug combinations but are uninformative about long-term response, since regular replacement of drugged media in 384-well format is labor-intensive. Additionally, it is impossible to distinguish between reduced growth rate and increased cell death in checkerboard assays measuring only cell viability at a fixed endpoint. To test whether PI3K inhibitors were effective in combination with GM-TKI under longer-term exposure, we performed time-resolved clonogenic assays on all three DTLs (Figure 2.7). In addition to PI3K inhibitors, we also tested co-inhibition of the serine/threonine kinases AKT1/2/3 (hereafter, AKT) and mTOR, which propagate mitogenic signals downstream of PI3K. We found that combining GM-TKI with ALP or capivasertib (CAPI), a pan-AKT inhibitor, led to durable proliferative arrest uniquely in PI3K-mutant lines, indicating that PI3K co-mutations contribute to GM-TKI tolerance. Treatment with the pan-PI3K inhibitor PIC led to growth arrest by itself in all lines, indicating the broad essentiality of PI3K signaling for proliferation, and co-treatment with GM-TKI led to substantial cell death uniquely in PI3K-mutant lines. The mTOR inhibitor rapamycin (RAP) significantly augmented GM-TKI activity in all three lines, and in some cases was effective as a single-agent, suggesting that all three depend on mTOR activity for growth. These results suggest that some degree of GM-TKI tolerance in a subset of our cell lines is explained by the presence of oncogenic co-mutations in PI3K, which confer a heightened dependency on the PI3K-AKT-mTOR axis.

Our query of the DepMap also revealed that the DTL H2228 harbors genetic deletion of *RB1*, a tumor suppressor with important regulatory roles in cell cycle progression and lineage fidelity, and loss of which has previously been linked to drug resistance (Figure 2.8A).[42,43] Recent studies have identified a synthetic lethal relationship between *RB1* and the mitotic serine/threonine kinases AURKA/B, which facilitate mitotic spindle assembly and chromosome segregation during mitosis.[44,45,46] We therefore wondered whether *RB1* deficiency might explain the reduced sensitivity of H2228 to ALK inhibition by conferring a hyperdependency for proliferation on AURKA/B (Figure 2.8B). To test this, we paired CER with the AURKA inhibitor alisertib (ALI) or the AURKB inhibitor barasertib (BAR) in a checkerboard assay format and found that co-inhibition of ALK and AURKA/B failed to show synergy except at extremely high doses of ALI, suggesting that treatment with CER does not increase the cellular dependency on AURKA/B even in an *RB1*-null background (Figures 2.8C and 2.8D). To test whether this drug combination showed efficacy in longer-term culture, we performed a time-resolved clonogenic assay pairing GM-TKI with ALI or BAR and observed considerable cytotoxicity of AURKA/B inhibition in all DTLs (Figure 2.8E). These findings suggest that AURKA/B is not a specific dependency or promoter of drug tolerance in H2228, but rather represents a pan-essential signal for cycling and survival.

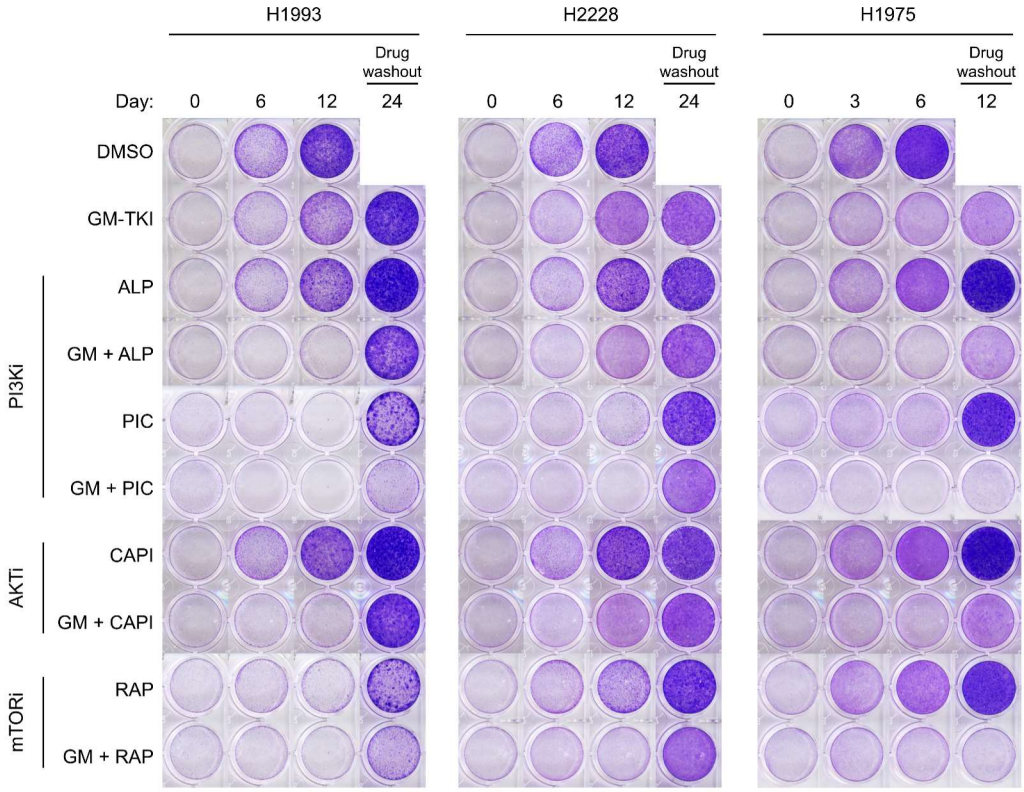

Figure 2.7. Clonogenic assays of viability response to GM-TKI combined with PI3K-AKT-mTOR pathway inhibitors

Clonogenic assay of DTLs treated with GM-TKI, PI3K/AKT/mTOR pathway inhibitors, or combinations thereof. All drugs were delivered at a dose of 1 μM. Duration of the experiment was shortened for H1975 due to its significantly faster growth, which caused poor adhesion to the plate under certain drug treatments after 10-12 days.

Quantification of cell-wide TK signaling under GM-TKI by tyrosine phosphoproteomics

Complete response to TKI therapy is highly dependent on successful drug-target engagement, durable inhibition of downstream signaling, and absence of compensatory mitogenic or pro-survival signaling. Direct analysis of TK cell signaling networks under therapeutic challenge can provide a readout of each of these important variables.[47] Given the near-binary difference in tolerance to GM-TKI within each pair of cell lines in our model system, we reasoned that a direct molecular comparison between DTLs and DSLs would likely enable the resolution of important contributors to tolerance. Since perturbing DSLs with GM-TKI for 72 hours resulted in an insufficient number of viable cells, we decided to harvest samples after 24 hours, at which point there were enough viable cells even from the most sensitive lines, such as EBC-1 and H3122 (Figure 2.9). Additionally, by choosing to examine the active signaling networks in cells at a relatively early timepoint, we increased the likelihood of detecting the earliest contributors to tolerance, which may be attractive targets for co-inhibition.[48]

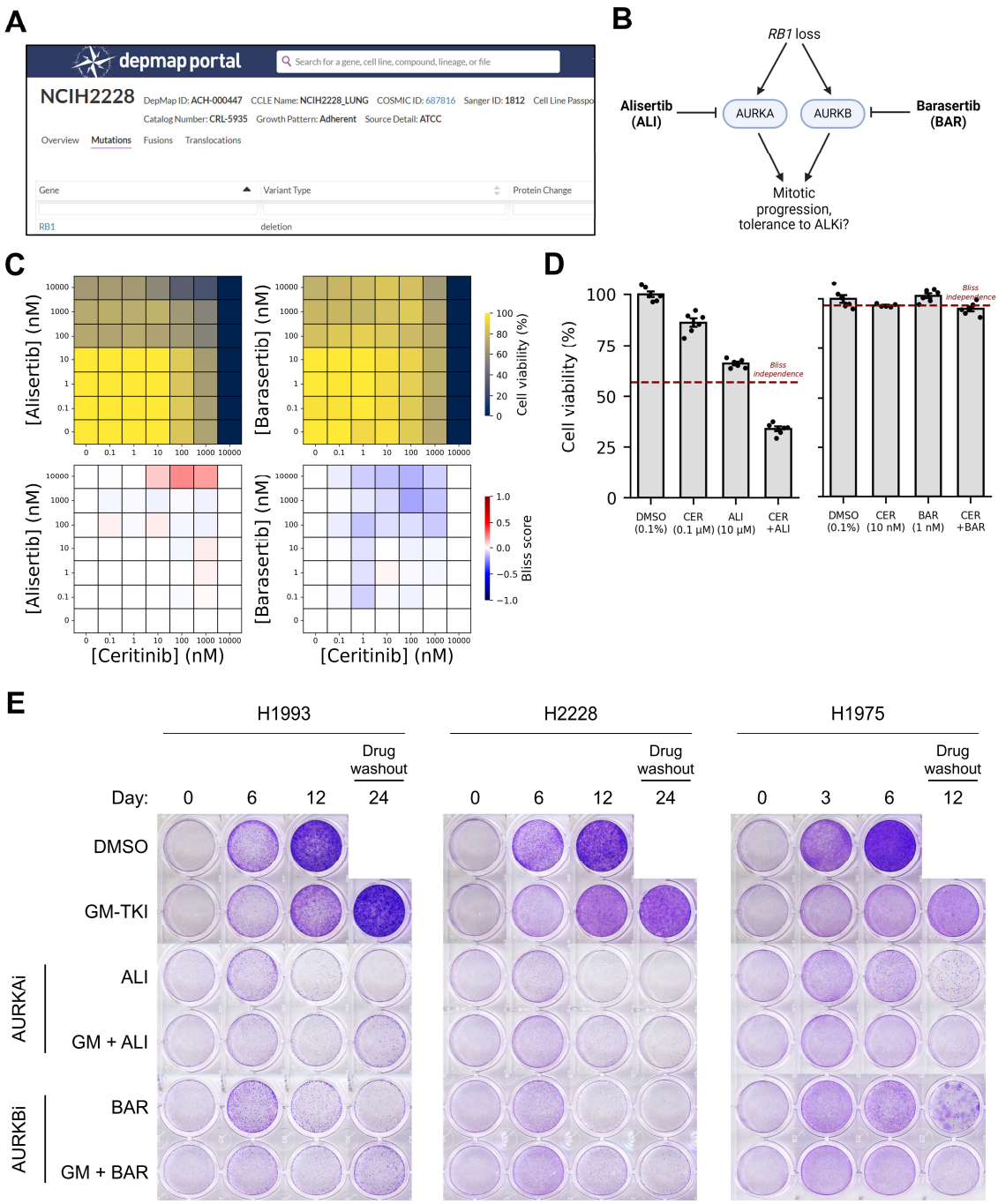

Figure 2.8. Examining the potential role of AURKA/B, synthetic lethal partners of *RB1*, in ALK inhibitor tolerance

A. *RB1* deletion reported in H2228 by the DepMap.
B. Pathway schematic depicting the targets of AURKA/B inhibitors used in this experiment and the hypothesized mechanism of ALK inhibitor tolerance.
C. Dose-response matrix (top) and Bliss synergy matrix (bottom) from checkerboard assays pairing CER with ALI (left) or BAR (right) in H2228. Treatment duration was 72 hours.
D. Viability of H2228 under the most synergistic combinations of drugs depicted in (C).
E. Clonogenic assay of DTLs treated with GM-TKI, AURKA/B inhibitors, or combinations thereof. All drugs were delivered at a dose of 1 µM.

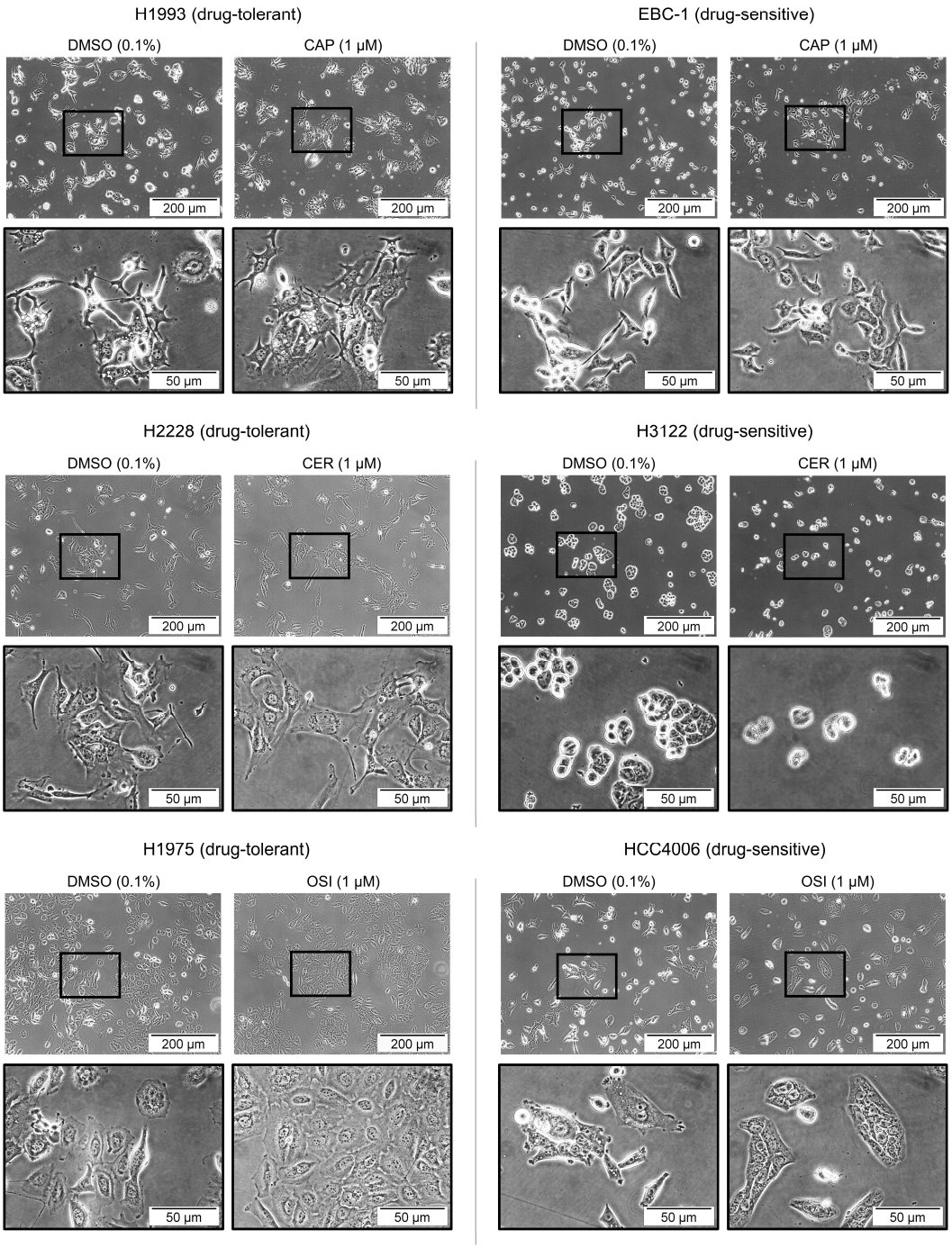

Figure 2.9. NSCLC cells under early GM-TKI treatment

Images taken of NSCLC cells exposed to GM-TKI or DMSO at the doses indicated for 24 hours.

To quantify TK signaling networks in GM-TKI-treated cells, we subjected whole cell lysates to multiplexed proteomics sample preparation and enrichment for tyrosine-phosphorylated peptides as was previously done for the targeted MS analysis, and analyzed peptides by high-

sensitivity untargeted MS (Figure 2.10A; see Appendix A for methods details). This approach, known as tyrosine phosphoproteomics (pY-MS), enables identification and quantification of large-scale (10^{2-3}) endogenous TK signaling events.

In our setting, TKI treatment is expected to lead to broad reduction of endogenous tyrosine phosphorylation, resulting in a large proportion of MS/MS spectra with missing TMT reporter ions in the channels corresponding to TKI treatment, a quantification challenge often referred to as the "missing value problem".[49] To preserve information from MS/MS scans with missing values, we developed a software solution that estimates the scan-specific noise band, below which all other co-analyzed fragments – including TMT reporter ions – are either undetected or intentionally unrecorded by the instrument to limit data transfer burden during and after acquisition (Figure 2.10B). Our computational approach uses the minimum-intensity fragment ion in each MS/MS scan to estimate this limit, then assumes that missing reporter ions have an intensity which is uniformly distributed between zero and the estimated limit. Using this approach, we were able to retain a majority of MS/MS scans which would otherwise have been discarded, and many of which were informative for analyzing the TK signaling activities occurring under heavily TK-inhibited conditions. Each of the three resulting pY-MS datasets, corresponding to the three (DTL, DSL) pairs sharing a given oncogenic TK, provided a high-dimensional quantitative map of basal and drug-altered TK signaling (Figures 2.10C – 2.10E).

Our pY-MS data enabled direct quantification of drug target activity under GM-TKI. We observed nearly complete target inhibition in all lines, confirming that drug tolerance in this system is not due to reduced drug transport into the cell, reduced drug-target interaction, or early reactivation of the target (Figure 2.11A).

Active RTKs phosphorylate tyrosine residues on adapter proteins, such as GAB1, GRB2, and SHC1, and on other important effectors of RTK signal propagation, including PLCG1 and PTPN11 (or SHP2), resulting in activation of cascades including the RAS-ERK and PI3K-AKT-mTOR pathways, among others. Due to their role as intermediate signaling molecules and as direct substrates of RTKs, tyrosine-phosphorylated adapter proteins are useful biomarkers of RTK activity. Under GM-TKI treatment, we observed significantly reduced adapter protein activity in all lines, with no consistent association between drug tolerance and adapter protein phosphorylation levels across lines (Figures 2.11B – 2.11D). MET inhibition by CAP in H1993 led to dramatic reduction in adapter protein phosphorylation at nearly all sites; a small number of sites, on SHB and SHC1, showed higher residual signal under drug compared to EBC-1. Similarly, H2228 showed greater residual or sustained phosphorylation of GAB1, SHP2, and SHC1 compared to H3122. H1975 showed higher levels of GAB1 and PLCG1 phosphorylation under EGFR inhibition by OSI compared to HCC4006. Some or all of these signals may contribute to DTLs' ability to sustain proliferative signaling under oncogenic TK inhibition.

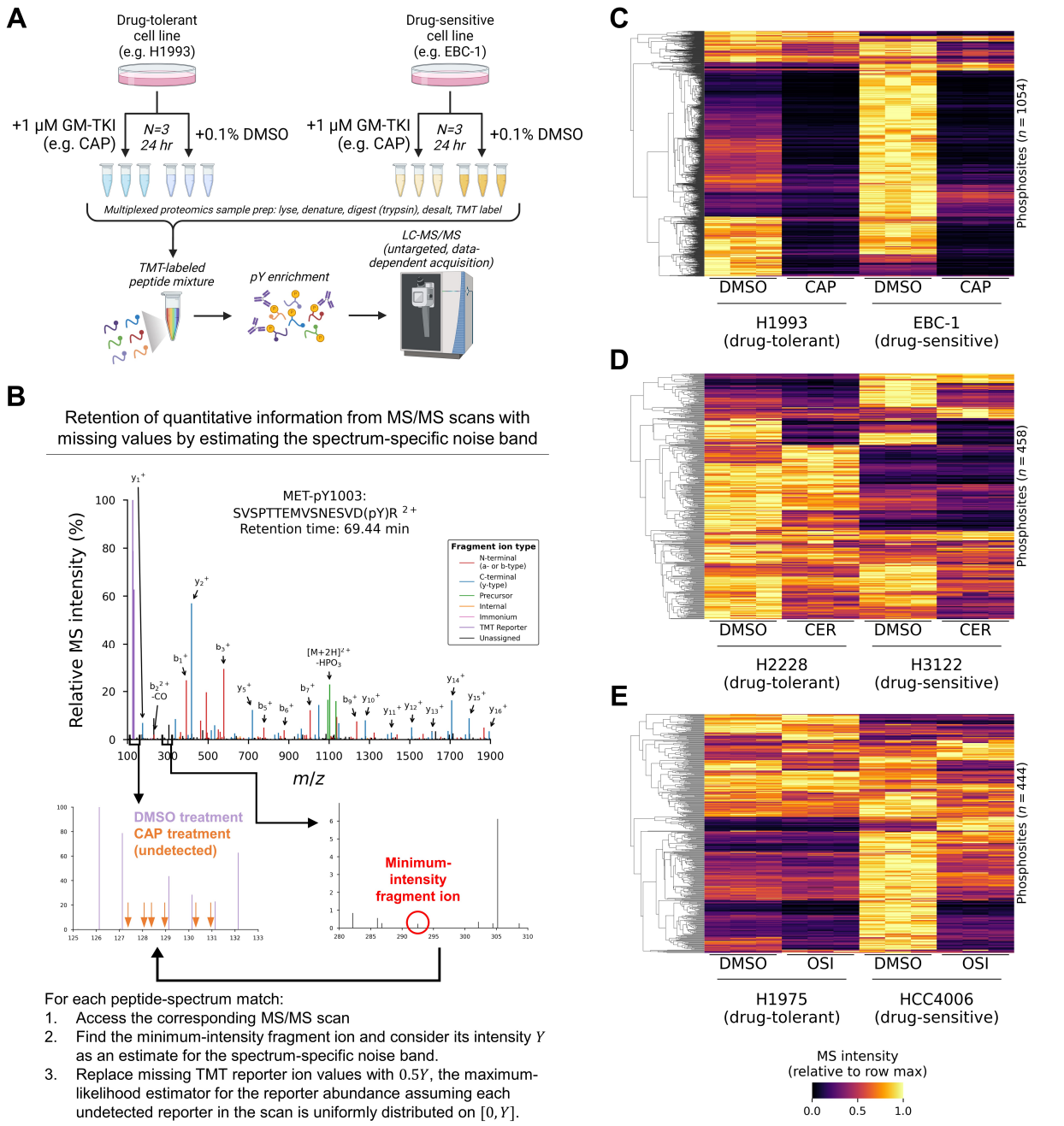

Figure 2.10. Analysis of cell-wide TK signaling under GM-TKI treatment by pY-MS

A. Experimental schematic for pY-MS analysis of active and inhibited signaling networks in DTLs and DSLs.

B. Workflow schematic detailing the pipeline of an automated software approach for construction of targeted MS acquisition methods from a user-defined set of phosphosites of interest.

C. Heatmap depiction of the abundances of tyrosine phosphosites in *MET*-amplified cell lines after 24 hours of exposure to 0.1% DMSO or 1 μM CAP, assayed by pY-MS using tandem mass tags (TMT). Abundances are normalized to the maximum value in each row.

D. Heatmap depiction of the abundances of tyrosine phosphosites in *ALK*-rearranged cell lines after 24 hours of exposure to 0.1% DMSO or 1 μM CER.

E. Heatmap depiction of the abundances of tyrosine phosphosites in *EGFR*-mutant cell lines after 24 hours of exposure to 0.1% DMSO or 1 μM OSI.

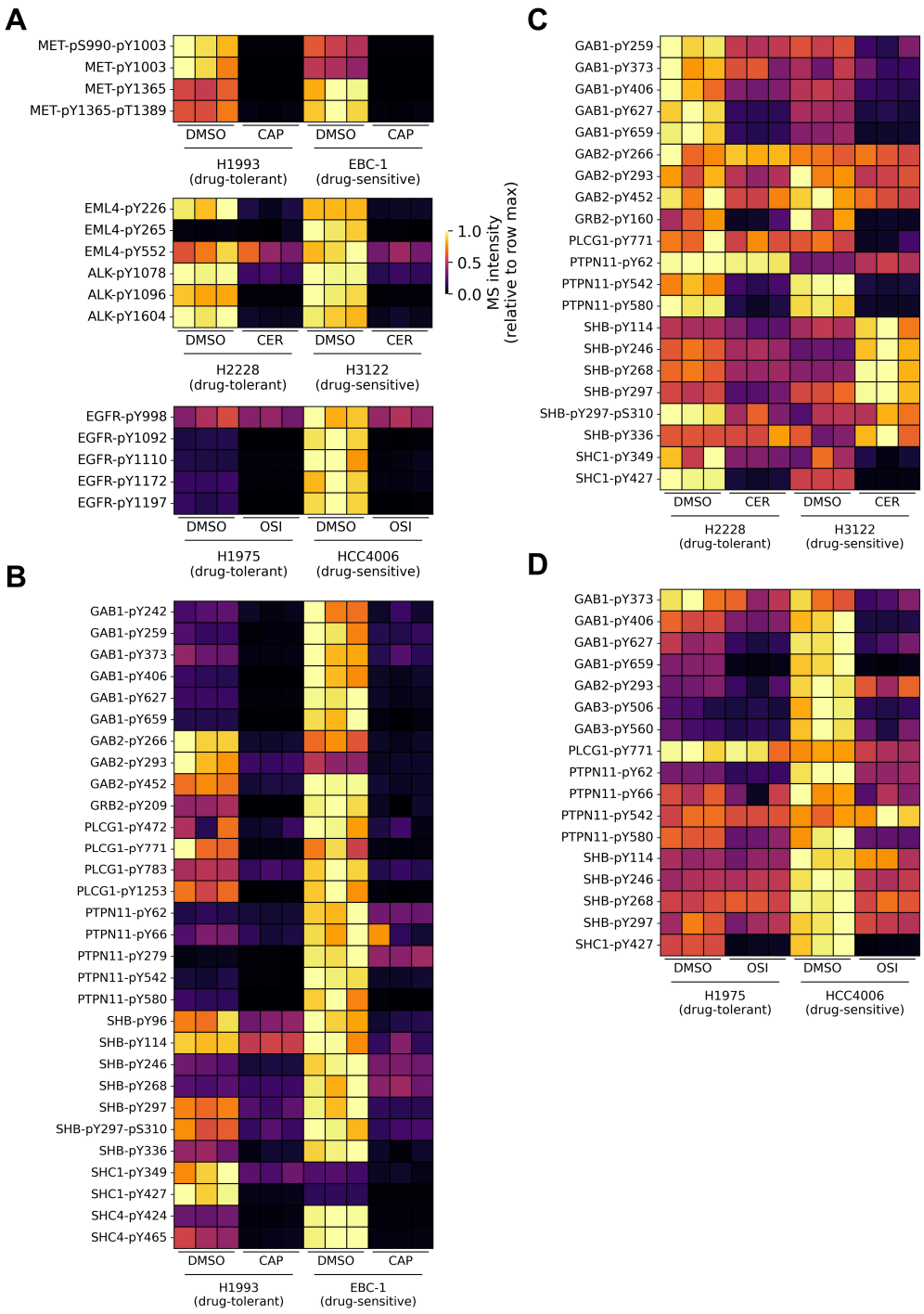

Figure 2.11. Drug target activity under GM-TKI

A. Heatmap depiction of the abundances of tyrosine phosphosites on MET, EML4-ALK, and EGFR after 24 hours of exposure to DMSO or GM-TKI. Abundances are normalized to the maximum value in each row.
B. Heatmap depiction of the abundances of tyrosine phosphosites on adapter proteins in *MET*-amplified cell lines after 24 hours of exposure to 0.1% DMSO or 1 μM CAP.
C. Heatmap depiction of the abundances of tyrosine phosphosites on adapter proteins in *ALK*-rearranged cell lines after 24 hours of exposure to 0.1% DMSO or 1 μM CER.
D. Heatmap depiction of the abundances of tyrosine phosphosites on adapter proteins in *EGFR*-mutant cell lines after 24 hours of exposure to 0.1% DMSO or 1 μM OSI.

While no significant differences in drug target activity were observed between DTLs and DSLs, we found that GM-TKI treatment led to significantly more pronounced tyrosine phosphoproteome remodeling in DSLs, suggestive of a general association between GM-TKI tolerance and robustness of TK signaling (Figure 2.12).

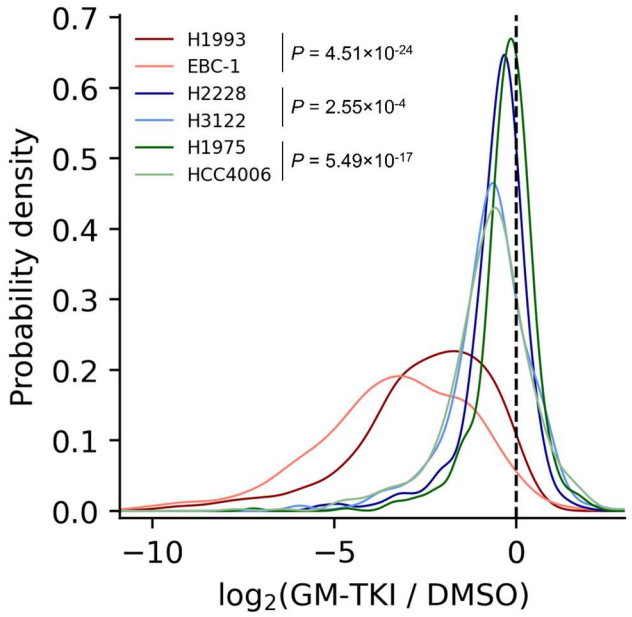

Figure 2.12. Tyrosine phosphoproteome-wide remodeling by GM-TKI
Distributions of tyrosine phosphorylation site abundance in all cell lines, expressed as a log-ratio over control (DMSO-treated) cells. *P*-values were derived by two-sided Mann-Whitney U test.

Exposure to exogenous sources of stress can cause induction of signaling events promoting cell survival; in cancer therapy, these adaptive responses can inadvertently antagonize drug mechanisms of action and promote drug tolerance.[47,50,51,52,53] We examined the drug-induced phosphotyrosine signals in each DTL and found that most signals were also induced by drug in DSLs, suggesting most of these sites are implicated in general stress-induced signaling (Figures 2.13A – 2.13C). DSLs demonstrated more pronounced drug-induced signaling in terms of average fold-increase over DMSO treatment, and in terms of total number of upregulated phosphosites in all cases but one (44 sites upregulated in HCC4006 compared to 47 in H1975). These observations suggest that drug-induced adaptive TK signaling is not sufficient to explain GM-TKI tolerance in our model system.

Signaling pathways which promote survival under drug can be potentiated to do so from the basal state of the cell prior to drug treatment. To examine the role of basal signaling in the response to GM-TKI, we performed a correlation analysis and found that for each pair of lines

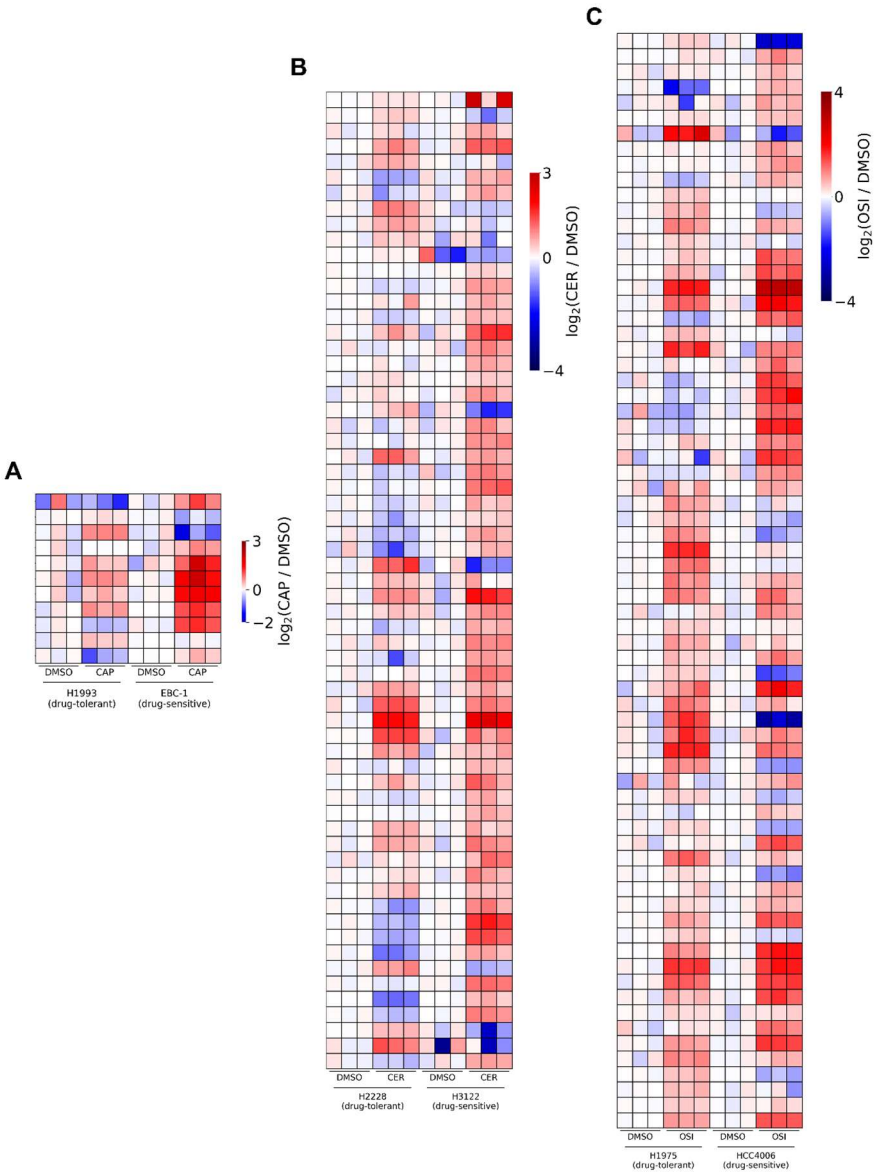

Figure 2.13. Drug-induced TK signaling in DTLs and DSLs

A. Heatmap depiction of the abundances of tyrosine phosphosites upregulated by CAP treatment in *MET*-amplified cell lines. Abundances are normalized to the average abundance in the corresponding DMSO-treated cells from the same line and $\log_2$-transformed.
B. Heatmap depiction of the abundances of tyrosine phosphosites upregulated by CER treatment in *ALK*-rearranged lines.
C. Heatmap depiction of the abundances of tyrosine phosphosites upregulated by OSI treatment in *EGFR*-mutant lines.

sharing a given oncogenic TK, there is significant correlation between differential (DTL versus DSL) phosphosite abundance under DMSO and differential abundance under GM-TKI, indicating that many TK signals which are basally higher in a given line remain higher in the same line under drug (Figures 2.14A – 2.14C). This linear relationship was especially strong in the *ALK*-rearranged

lines, where the direction and magnitude of basal signaling was usually highly preserved under drug. Other signals, however, showed greater abundance in a given line under DMSO and reduced abundance in that line under drug; this was especially true for signaling in the *MET*-amplified lines, indicating that the basal signaling state of the cell is not perfectly predictive – but is nevertheless highly informative – of the state of the cell under inhibitor treatment.

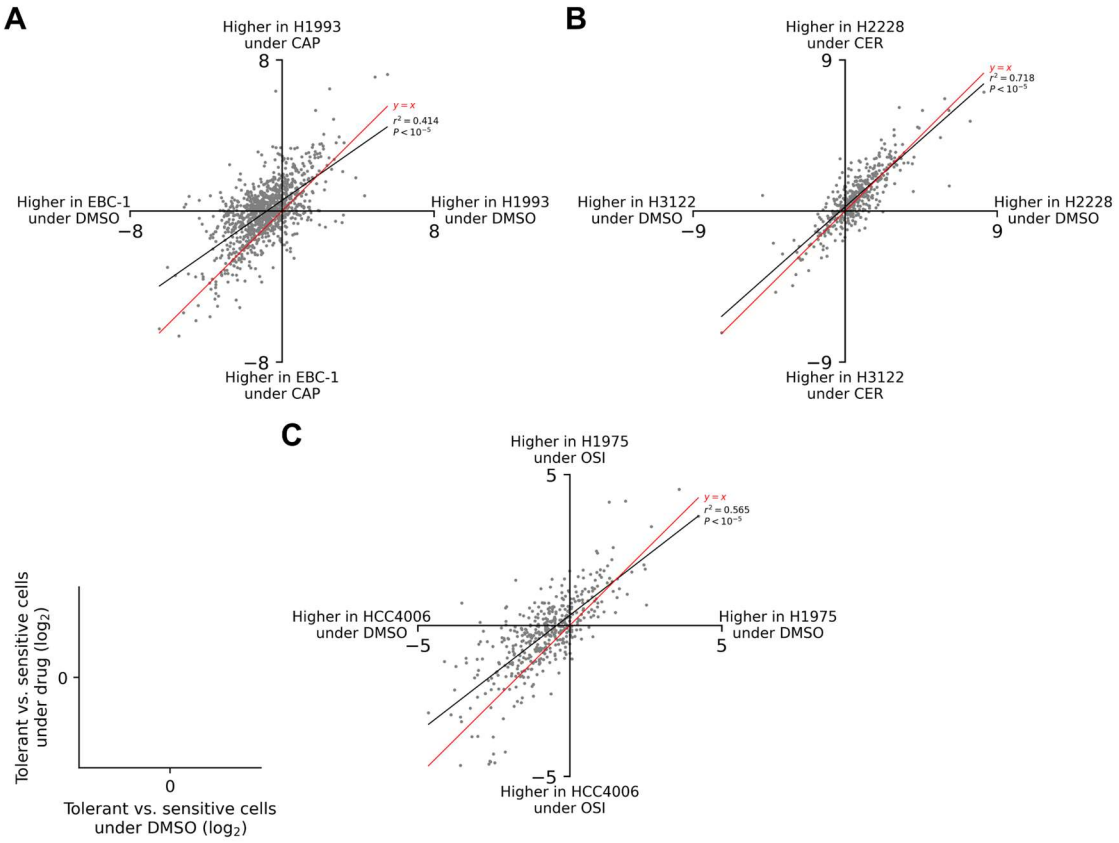

Figure 2.14. Correlation analysis of differential TK signaling under DMSO and GM-TKI

A. Scatterplot depicting tyrosine phosphorylation sites in *MET*-amplified cell lines, embedded in the following two-dimensional space: the x-axis plots differential abundance (DTL vs. DSL, $\log_2$-ratio) under DMSO treatment, and the y-axis plots differential abundance (DTL vs. DSL, $\log_2$-ratio) under CAP treatment. Phosphosites which lie on the $y = x$ line (red) represent signals whose basal differential between cell lines was exactly preserved under drug.
B. Scatterplot depicting tyrosine phosphorylation sites in *ALK*-rearranged lines.
C. Scatterplot depicting tyrosine phosphorylation sites in *EGFR*-mutant lines.

pY-MS enables detection of cell line-specific signals promoting drug tolerance

In examining phosphotyrosine signals with significantly greater abundance in DTLs compared to DSLs under GM-TKI treatment, we found three cell line-specific TK signaling events contributing to drug tolerance, which are described individually throughout the following section.

Among TK signaling events associated with any DTL, we found evidence for residual EGFR activity in H1993, and fully sustained EGFR activity in H2228 (Figure 2.15A). Consistent with our previous correlation analysis, both of these signals were preserved from greater basal EGFR activity in these lines. To determine whether EGFR contributes to GM-TKI tolerance in these lines, we treated DTLs with the EGFR inhibitor erlotinib (ERL) alongside GM-TKI in clonogenic assay format. Expectedly, ERL failed to augment OSI in H1975, but led to durable growth arrest of H1993 when combined with CAP, indicating a high degree of dependency on residual EGFR activity for sustained proliferation under MET inhibition (Figure 2.15B). In H2228, however, ERL failed to meaningfully augment CER. Consistent with our clonogenic assay result, we found by checkerboard assay that ERL was broadly synergistic with CAP in H1993 (Figures 2.15C and 2.15D). These findings indicate that residual EGFR activity is a cell line-specific contributor to drug tolerance.

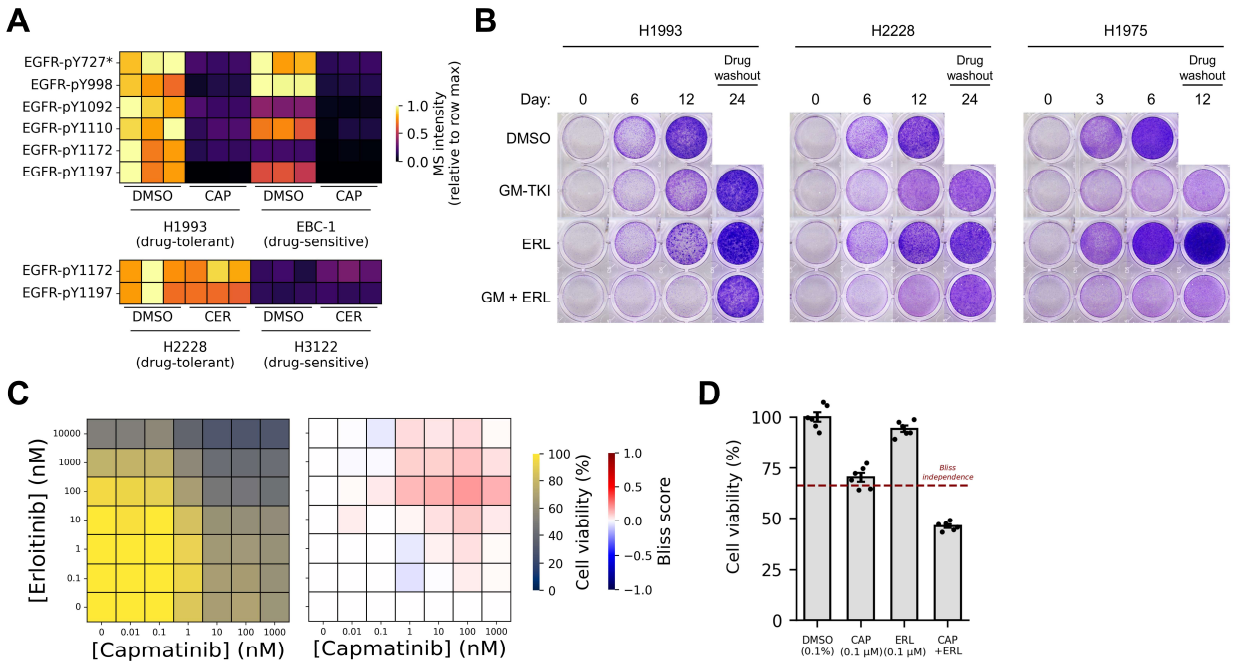

Figure 2.15. Assessing the role of residual and sustained EGFR activity in tolerance to GM-TKI

A. Heatmap depiction of the abundances of EGFR phosphosites in *MET*-amplified and *ALK*-rearranged cell lines. Abundances are normalized to the maximum value in each row.
B. Clonogenic assay of DTLs treated with GM-TKI, ERL, or combinations thereof. All drugs were delivered at a dose of 1 μM.
C. Dose-response matrix (left) and Bliss synergy matrix (right) from a checkerboard assay pairing CAP with ERL in H1993. Treatment duration was 72 hours.
D. Viability of H1993 under the most synergistic combination of drugs depicted in (C).
*The tryptic phosphopeptide supporting EGFR-pY727 also maps to two other paralogous ERBB family members (ERBB2-pY735 and ERBB4-pY733).

In addition to EGFR, we found that H2228 displayed high basal activation of AXL, an RTK which is activated by its endogenous ligand GAS6 and has been implicated in drug resistance (Figure 2.16A).[15,54] High basal activity of AXL was preserved under CER treatment, prompting us to investigate whether this signal contributed to tolerance to ALK inhibition. None of the DTLs demonstrated sensitivity to bemcentinib (BEM), a selective AXL inhibitor, and in H2228, BEM failed to meaningfully augment CER (Figure 2.16B). However, the combination of CER, BEM, and ERL led to substantial proliferative reduction (Figure 2.16C), indicating that maintenance of both EGFR and AXL activity sustains cycling of H2228 under ALK inhibition.

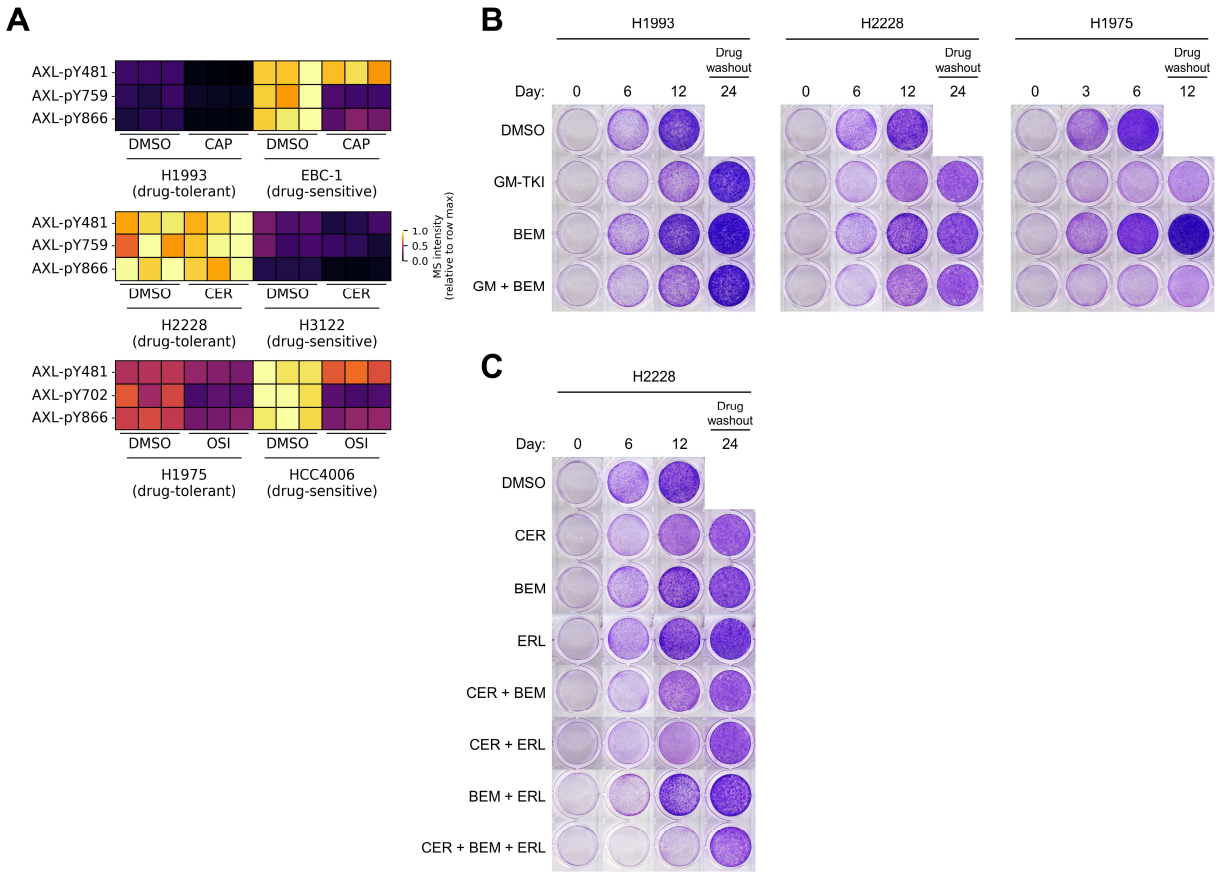

Figure 2.16. Assessing the role of sustained AXL activity in tolerance to GM-TKI

A. Heatmap depiction of the abundances of AXL phosphosites in DTLs. Abundances are normalized to the maximum value in each row.
B. Clonogenic assay of DTLs treated with GM-TKI, BEM, or combinations thereof. All drugs were delivered at a dose of 1 μM.
C. Clonogenic assay of H2228 treated with CER, BEM, ERL, or combinations thereof. All drugs were delivered at a dose of 1 μM.

The RAS-ERK pathway (also known as the MAP kinase or MAPK pathway) is an important cascade that transduces signals from MET, ALK, EGFR, and many other receptors to coordinate cell proliferation, differentiation, migration, and other cellular processes.[55] High levels of phosphorylated activation loops of ERK1/2, canonically by the dual specificity kinases MEK1/2, are reliable indicators of pathway activity. In H1975, we observed near-complete RAS-ERK pathway inhibition by OSI treatment, whereas in H1993 and H2228, we observed residual and sustained pathway activation under GM-TKI, respectively (Figure 2.17A). Intriguingly, these phosphorylation patterns closely resemble those of the upstream kinases EGFR and AXL, suggesting that residual EGFR activity may promote residual RAS-ERK pathway activity in H1993, and that sustained EGFR and AXL activity may jointly maintain flux through RAS-ERK in H2228. Consistent with this model, MEK1/2 inhibition by trametinib (TRAM) led to durable proliferative arrest of H1993, phenocopying the effect of dual MET/EGFR inhibition (Figure 2.17B). TRAM was potently cytotoxic as a single-agent in H2228, indicating a high degree of survival dependency on the RAS-ERK pathway even when bypassing EML4-ALK altogether.

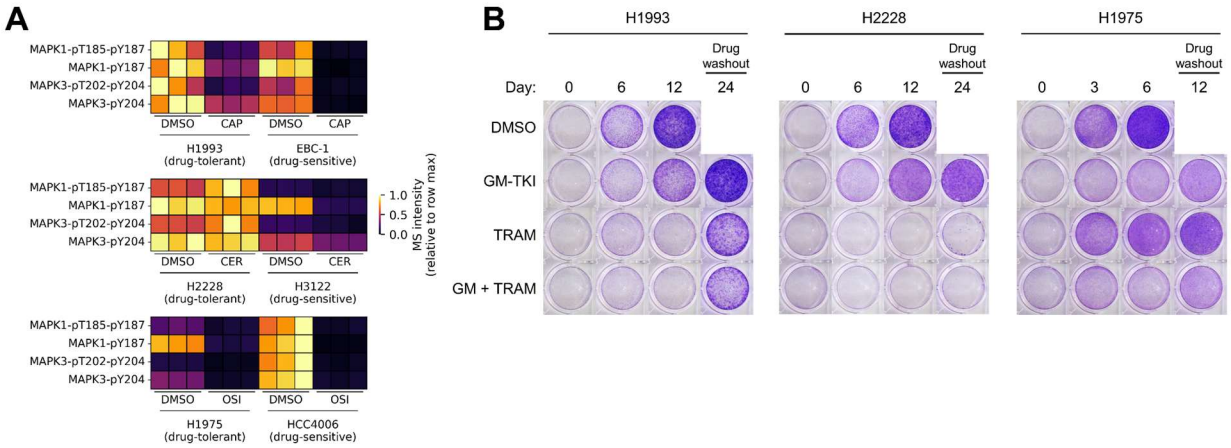

Figure 2.17. Assessing the role of residual and sustained MEK1/2 activity in tolerance to GM-TKI

A. Heatmap depiction of the abundances of MAPK1/3 (ERK2/1) phosphosites in DTLs. Abundances are normalized to the maximum value in each row.
B. Clonogenic assay of DTLs treated with GM-TKI, TRAM, or combinations thereof. All drugs were delivered at a dose of 1 μM.

Fold change-normalized quantification results in loss of basal signaling information leading to false-positive and false-negative drug target predictions

In perturbation studies such as ours, it is conventional to express quantitative molecular data in terms of fold-change over a control condition (often log-transformed). We retrospectively

examined our pY-MS data and found that we likely would have made several critical misinterpretations had we strictly examined the data under a "log fold-change over DMSO" (logFC) transformation. Specifically, we found that logFC-normalizing the abundances of ERK1/2 phosphosites led us to the spurious conclusion that MEK1/2 was incompletely inhibited in H1975 under OSI (Figure 2.18A). Our original row-max normalization clearly shows that this discrepancy comes from significantly greater basal phosphorylation of ERK1/2 in HCC4006; indeed, these cells undergo greater MEK1/2 inhibition by OSI when inhibition is expressed as a percentage of basal activity. However, we previously showed that MEK1/2 inhibition by TRAM failed to augment the effect of OSI in H1975 (Figure 2.17B), suggesting that fractional (logFC-normalized) activity may be a misleading measure of mitogenic or survival dependency. Additionally, we found that by logFC-normalizing the abundances of EGFR phosphosites in *MET*-amplified cells, dramatic differences in basal EGFR phosphorylation caused us to arrive at the incorrect conclusion that EGFR is equally inhibited by CAP in both lines (Figure 2.18B). Our observation that ERL significantly augmented CAP in H1993 provides post-hoc conformation that the residual EGFR activity (observed under row-max normalization) in H1993 is consequential for proliferation. These results together suggest that absolute TK activity, rather than fractional activity, may better inform drug target selection, and that caution should be exercised in choosing normalization strategies in comparative perturbation studies.

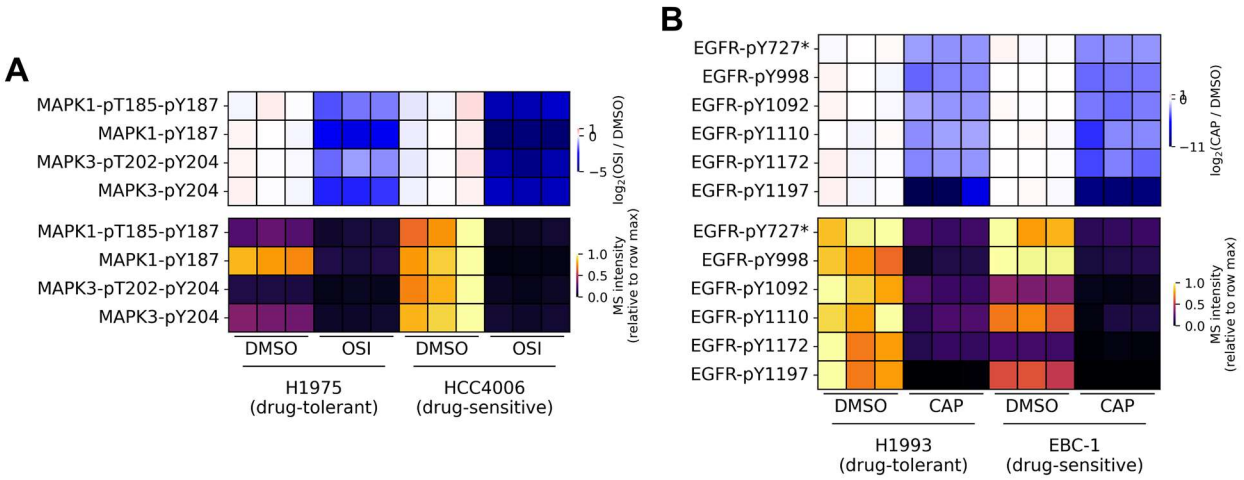

Figure 2.18. Retrospective examination of the effect of data normalization on drug target selection

A. Heatmap depiction of the abundances of MAPK1/3 (ERK2/1) phosphosites in *EGFR*-mutant cell lines. Abundances are normalized to the average abundance in the corresponding DMSO-treated cells from the same line and $\log_2$-transformed (top), or normalized to the maximum value in each row (bottom).

B. Heatmap depiction of the abundances of EGFR phosphosites in *MET*-amplified cell lines.
*The tryptic phosphopeptide supporting EGFR-pY727 also maps to two other paralogous ERBB family members (ERBB2-pY735 and ERBB4-pY733).

pY-MS reveals basal and sustained SFK/ABL signaling as a consensus promoter of drug tolerance

Cell line-specific mechanisms of drug tolerance are informative for tailoring effective combination therapies for each model system uniquely. Consensus mechanisms, however, may represent a highly attractive opportunity to mitigate drug tolerance with a single combination strategy which generalizes across models with distinct (epi)genetic backgrounds. To search for consensus signaling events promoting drug tolerance, we examined phosphosites showing consistently greater abundance in each DTL compared to its corresponding DSL, both under DMSO and GM-TKI (Figures 2.19A and 2.19B). Providing validation of this approach, CDK1/2/3-pY15 was significantly more abundant in all DTLs compared to DSLs under GM-TKI, consistent with heightened cell cycle progression under drug.[56]

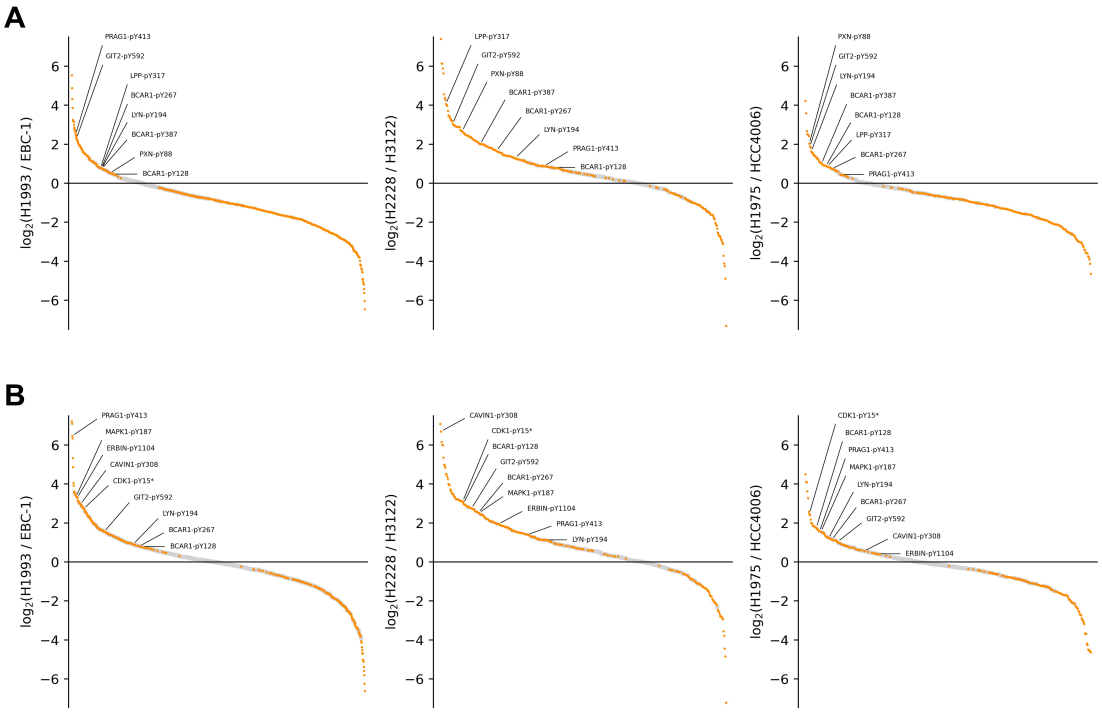

Figure 2.19. SFK substrate phosphorylation in DTLs under GM-TKI

A. Tyrosine phosphosites rank-ordered by their relative abundance under DMSO treatment in *MET*-amplified lines (left), *ALK*-rearranged lines (center), and *EGFR*-mutant lines (right). Orange indicates significantly differential abundance between lines ($P < 0.05$ by two-sided *t*-test with multiple hypothesis correction by the Benjamini-Hochberg procedure). Sites with significantly greater abundance in all DTLs compared to corresponding DSLs are annotated.

B. Tyrosine phosphosites rank-ordered by their relative abundance under drug treatment in *MET*-amplified lines (left), *ALK*-rearranged lines (center), and *EGFR*-mutant lines (right). Orange indicates significantly differential abundance between lines ($P < 0.05$ by two-sided *t*-test with multiple hypothesis correction by the Benjamini-Hochberg procedure). Sites with significantly greater abundance in all DTLs compared to corresponding DSLs are annotated.

*The tryptic phosphopeptide supporting CDK1-pY15 also maps to two other paralogous CDKs (CDK2-pY15 and CDK3-pY15).

Among the sites consistently greater in abundance in DTLs compared to DSLs, we found that several – including sites on BCAR1, LPP, and PXN – are derived from known substrates of the mitogenic and survival-promoting SRC family kinases (SFK).[57,58,59,60,61] Additionally, one other such site (LYN-pY194) is on an SFK itself and likely promotes activity.[62] These observations suggest that SFK signaling may be heightened in DTLs relative to the corresponding DSLs.

Since we also observed that some putative SFK substrates were more abundant in DSLs, we wondered whether there was evidence for statistically significant SFK signaling in DTLs, or if putative SFK substrates are simply uniformly distributed throughout the tyrosine phosphoproteome. Since most kinase-substrate relationships have yet to be discovered at phosphosite-specific resolution, we used published protein-protein interaction data from BioGRID[63] to test for significant overrepresentation of known SFK interactors among phosphosites which showed significantly greater abundance in DTLs compared to DSLs. We included the SRC-like kinases ABL1/2, which are known to share substrates with the SRC family and regulate many of the same downstream processes.[64,65] We observed significant overrepresentation of SFK/ABL interactors in each DTL under DMSO (Figure 2.20, upper). Strikingly, we found no significant overrepresentation of SFK or ABL1/2 interactors among any DSLs. Under GM-TKI exposure, the effect sizes and significance values for SFKs and ABL1/2 were reduced, but there remained at least one kinase with significant enrichment for each DTL, and no kinases in any of the DSLs (Figure 2.20, lower). These results provide statistical support to the observation that high SFK/ABL signaling is associated with drug tolerance.

Motivated by our finding that basal and sustained SFK/ABL signaling is a common feature among DTLs, we wondered whether SFK/ABL inhibition might augment GM-TKI in DTLs. To test this, we paired each GM-TKI with the SFK/ABL inhibitors bosutinib (BOS), dasatinib (DAS), ponatinib (PON), or saracatinib (SAR) in checkerboard assay format for each DTL. Notably, we observed synergy between GM-TKI and SFK/ABL inhibition across all lines, indicating that GM-TKI treatment generally confers a heightened sensitivity to SFK/ABL inhibition (Figures 2.21A – 2.21D). The most synergistic combinations in H2228 (CER + PON at 1 μM each) and H1975 (OSI + DAS at 100 nM each) led to profound cell death, suggesting that GM-TKI promotes a strong survival dependency on SFK/ABL signaling in these lines (Figure 2.21E). In complementary clonogenic assays, we found that co-treatment with SFK/ABL inhibitors, especially DAS and PON, substantially augmented GM-TKI activity in all DTLs, leading to durable cell cycle arrest or cell death (Figure 2.22). BOS and SAR both exerted a significant effect in combination with GM-TKI but not in all lines, suggesting distinct target profiles of these agents and distinct dependencies on particular SFK/ABL members in each line. Together, these findings indicate that heightened basal SFK/ABL signaling, which is sustained under GM-TKI exposure, is a consensus mechanism underlying drug tolerance.

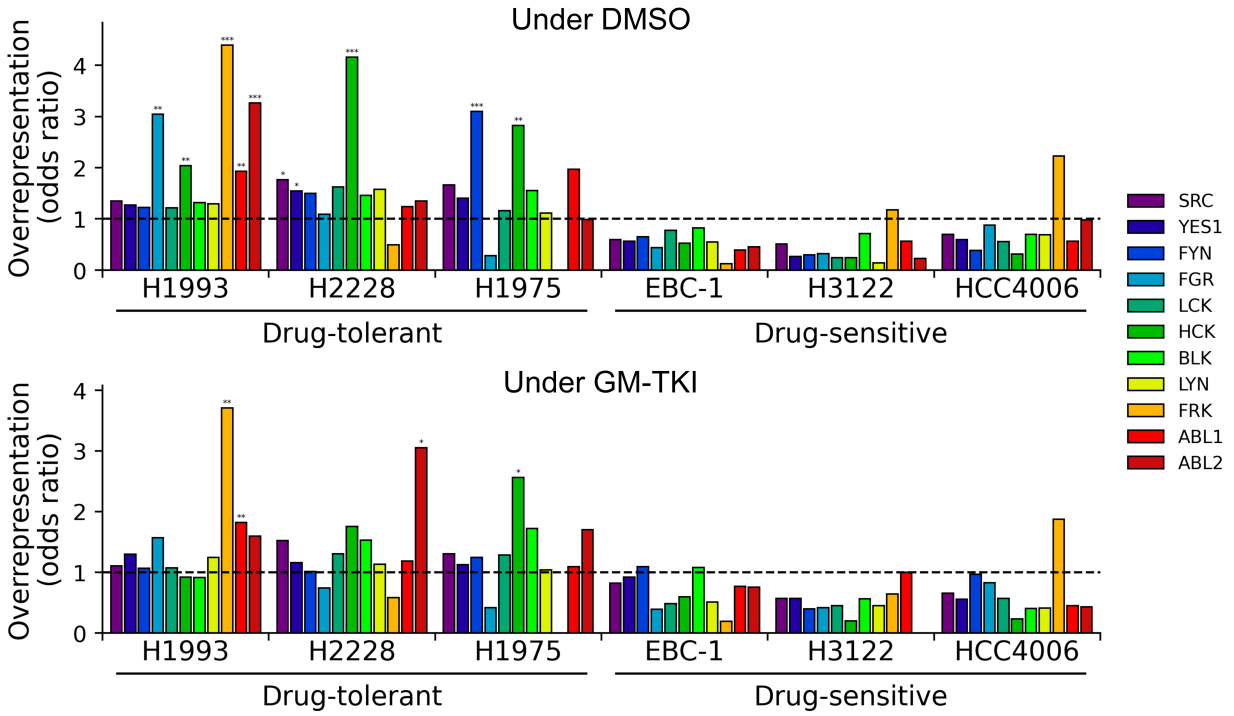

Figure 2.20. Overrepresentation analysis of known SFK/ABL interactors among differential TK signals

Bar graphs depicting the degree of overrepresentation of proteins known to interact with SFKs or ABL1/2 among phosphosites with greater abundance in each DTL compared to its corresponding DSL, and vice versa. * : $P < 0.1$; ** : $P < 0.05$; *** : $P < 0.01$ by one-sided Fisher's exact test with multiple hypothesis correction by the Benjamini-Hochberg procedure.

Finally, we wondered about the relative contribution of ABL1/2 to the efficacy of SFK/ABL inhibitors combined with GM-TKI. To isolate the effects of SFK inhibition and ABL1/2 inhibition, we treated cells in checkerboard assay format with imatinib (IMAT), which is selective for ABL1/2 over SFKs, and found that IMAT was modestly synergistic with GM-TKI in H2228 (Figures 2.23A and 2.23B), consistent with our earlier observation of heightened ABL2 signaling in H2228 under GM-TKI (Figure 2.20). In clonogenic experiments, IMAT co-treatment led to reduced growth uniquely in H1993 (Figure 2.23C), consistent with our earlier observation of heightened ABL1/2 signaling in H1993 (Figure 2.20). Altogether, these results support a model where high basal and sustained SFK/ABL signaling, the relative contributions of which (SFK versus ABL1/2) are cell line-specific, is a unifying driver of proliferative and survival signaling in cancer cells undergoing oncogenic TK inhibition.

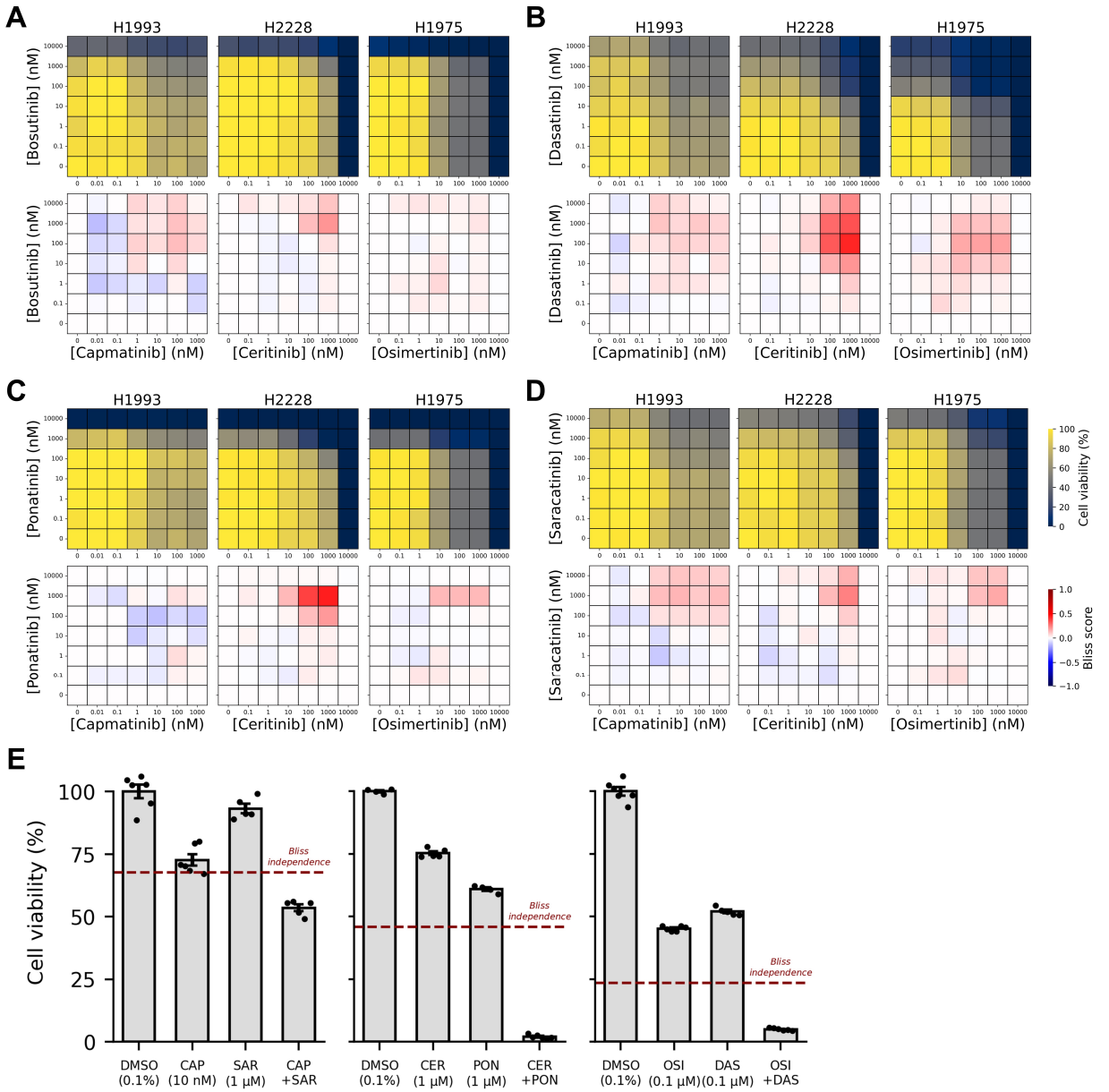

Figure 2.21. Synergy landscape between GM-TKI and SFK/ABL inhibition

A. Dose-response matrix (top) and Bliss synergy matrix (bottom) from checkerboard assays pairing GM-TKI with BOS. Treatment duration was 72 hours.

B. Dose-response matrix (top) and Bliss synergy matrix (bottom) from checkerboard assays pairing GM-TKI with DAS.

C. Dose-response matrix (top) and Bliss synergy matrix (bottom) from checkerboard assays pairing GM-TKI with PON.

D. Dose-response matrix (top) and Bliss synergy matrix (bottom) from checkerboard assays pairing GM-TKI with SAR.

E. Viability of H1993 (left), H2228 (center), and H1975 (right) cells under the most synergistic combination of drugs depicted in (A-D).

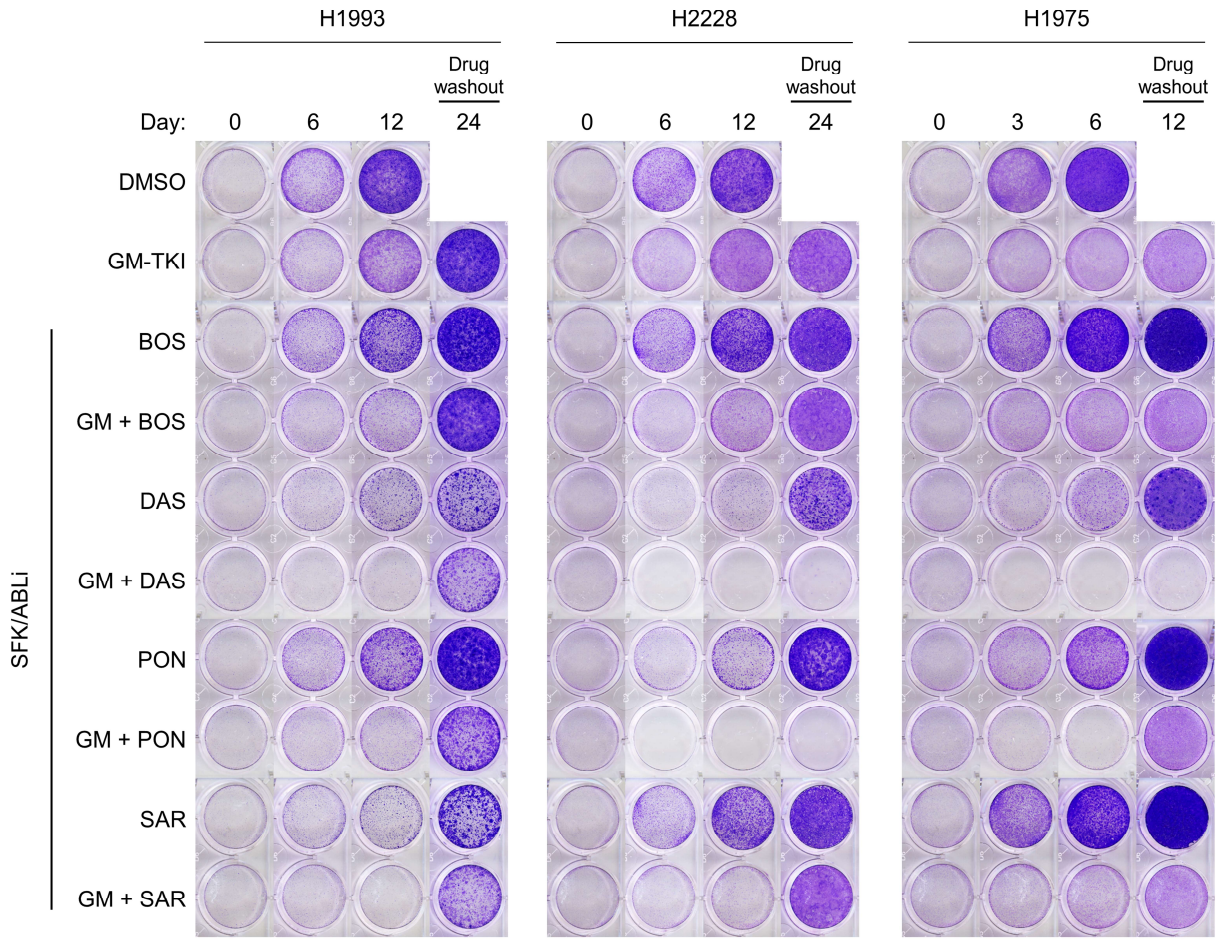

Figure 2.22. Clonogenic assays of viability response to GM-TKI combined with SFK/ABL inhibitors

Clonogenic assay of DTLs treated with GM-TKI, BOS, DAS, PON, SAR, or combinations thereof. All drugs were delivered at a dose of 1 μM.

Discussion

In this work, we interrogate the tumor cell-intrinsic signals contributing to tolerance to oncogenic kinase inhibition, with a focus on MET, ALK, and EGFR. Many previous studies have examined the molecular and mechanistic basis for TKI response, especially as it relates to intrinsic resistance,[66] subclonal drug tolerance (DTPs),[67] drug-induced adaptive signaling,[68] and acquired resistance.[69] Less emphasis has been placed on establishing and profiling model systems which demonstrate failure of therapy to restrain proliferation from the immediate onset of drug exposure. Additionally, fewer studies have examined this phenomenon in the context of MET and ALK

inhibition compared to EGFR inhibition, likely due to their lower alteration frequency in NSCLC and other cancers, and to the more recent clinical use of MET- and ALK-directed TKIs.[12,70]

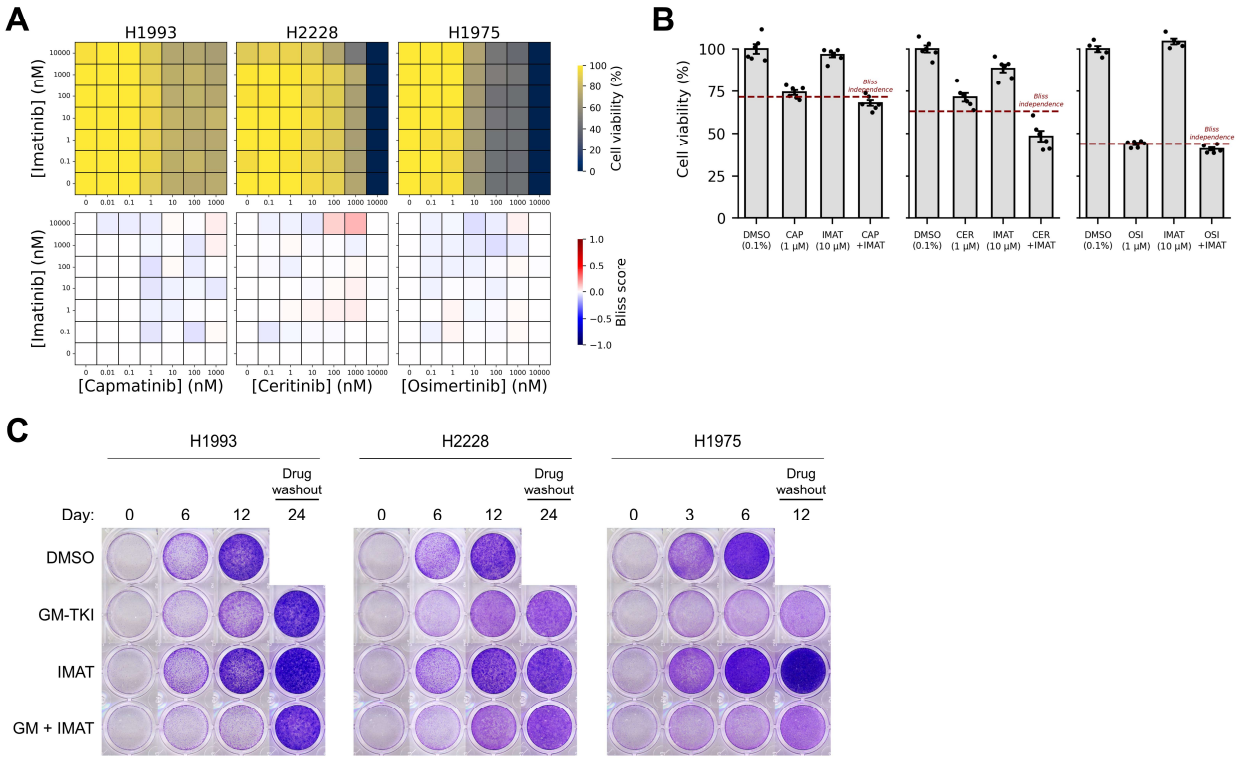

Figure 2.23. Isolating the role of ABL1/2 in tolerance to GM-TKI

A. Dose-response matrix (top) and Bliss synergy matrix (bottom) from checkerboard assays pairing GM-TKI with IMAT. Treatment duration was 72 hours.
B. Viability of H1993 (left), H2228 (center), and H1975 (right) cells under the most synergistic combination of drugs depicted in (A).
C. Clonogenic assay of DTLs treated with GM-TKI, IMAT, or combinations thereof. All drugs were delivered at a dose of 1 μM, except IMAT (10 μM) due to its reduced potency against ABL1/2.

A trivial explanation for insensitivity to targeted therapy is a lack of dependency on the intended target; for example, if a cell expresses MET at a high level, but is not reliant on increased MET signaling for maintaining its basal proliferation rate, then it is expected that MET inhibition would show no effect on the fitness of the cell. In our model system, each DTL showed reduced growth rate under GM-TKI, confirming that the expressed oncogenic TK in each line contributes positively to fitness and thereby invalidating this hypothesis.

A limitation of our model system is the inherent simplicity of cancer cell lines, which are unable to recapitulate the complexity of *in vivo* tumor biology; tumor cell-extrinsic signals from the tumor microenvironment and engagement of the host immune response are recognized to play an outsized role in response to targeted therapy.[71,72] However, some of our observations of

differential sensitivity of cell lines to GM-TKI are corroborated by clinical evidence: several studies have reported reduced response rates to ALK inhibitors among NSCLC patients expressing EML4-ALK variant 3 (present in H2228) compared to patients expressing variant 1 (present in H3122).[37,73,74] Additionally, signaling analyses performed on more complex *in vivo* model systems and on human tumor biopsies support our key finding of the important role of SFK/ABL signaling in therapy response.[75,76,77,78,79,80,81] We therefore assert that our model system, though unsuitable for exploring many of the complex properties of tumor biology, still provides a powerful model to explore the fundamental principles governing oncogenic signaling and growth dependency in cancer cells.

Oncogenic co-mutations are a widely accepted model for tolerance to targeted therapy directed against an oncogenic TK; by sustaining signaling independently of the targeted TK, or otherwise dampening the dependency of the cell on the targeted TK for cycling or survival, co-mutated oncogenic events pose a significant barrier to therapeutic success in the clinic.[38] We show that co-mutations can contribute to GM-TKI tolerance in NSCLC cell lines but in a cell line-specific manner, and that in some cases – such as H2228, which harbors *RB1* loss – co-targeting the alternate oncogenic event is not productive or possible. According to the DepMap, DTLs in our system harbored additional co-mutations we did not pursue, including loss-of-function mutations in STK11 (in H1993) and in CDKN2A (in H1975), both of which are tumor suppressors. The complex and cell-specific role of the tumor mutational background in therapeutic response motivated us to search for more general mechanisms of drug tolerance, with high priority placed on those which could be exploited therapeutically.

A key finding of our work is that SFK/ABL signaling is a shared dependency in DTLs treated with GM-TKI. The experiments establishing this result were motivated by the observation that each DTL showed high levels of phosphorylation of putative SFK substrates under drug compared to the paired DSL. We note that each DTL showed phosphorylation of a unique set of SFK/ABL substrates, likely a consequence of cell line-specific SFK expression, activity, or subcellular localization. SFKs, ABL1/2, and other SRC-like kinases collectively phosphorylate hundreds of confirmed substrates, and the particular phosphorylation patterns of these substrates is highly context- and cell type-dependent.[60,82,83] The complexity of SFK signaling motivated the use of a statistically-grounded enrichment approach to test whether our pY-MS data held sufficient evidence in support of the hypothesis of heightened SFK signaling among DTLs. Due to the lack of comprehensive prior knowledge of kinase-substrate pairs at phosphosite-specific resolution, we were limited to the use of published protein-protein interaction data to test for overrepresentation of known SFK interactors. However, given that physical interaction is a prerequisite for protein phosphorylation, and that our pY-MS data confirms tyrosine phosphorylation of the supposed

interactor, we believe this approach is useful for nominating kinases with potential phenotypic consequence.

Our co-treatment experiments pairing GM-TKI with SFK/ABL inhibitors showed that DAS and PON effectively prevented outgrowth in all three DTLs, and drove complete cell death in a subset of lines. BOS, however, did not show similar efficacy, only slowing growth in H1993 and to a lesser extent in H2228. We reason this may be due to the distinct polypharmacology of these drugs, which are not equally effective across all SFKs; in particular, at least one SFK (LCK) is a confirmed target of DAS and PON but not BOS according to DrugBank,[84] and the detection of LCK-specific phosphopeptides in our pY-MS data confirmed that each cell line in our model system expresses LCK. Though this finding is insufficient to confidently explain the reduced effect of BOS combined with GM-TKI, our data are consistent with the accepted notion that different targeted agents have distinct target profiles.

Our study demonstrates the capability of pY-MS to resolve proliferative and survival dependencies within the tyrosine kinome and sheds light on the consensus signaling events dictating limited sensitivity to GM-TKI therapy.

References

1. Czernilofsky A.P., Levinson A.D., Varmus H.E., Bishop J.M., Tischer E., Goodman H.M. (1980). Nucleotide sequence of an avian sarcoma virus oncogene (src) and proposed amino acid sequence for gene product. Nature *287*, 198-203.
2. Sefton B.M., Hunter T., Beemon K., Eckhart W. (1980). Evidence that the phosphorylation of tyrosine is essential for cellular transformation by Rous sarcoma virus. Cell *20*, 807-16.
3. Konopka J.B., Watanabe S.M., Witte O.N. (1984). An alteration of the human c-abl protein in K562 leukemia cells unmasks associated tyrosine kinase activity. Cell *37*, 1035-42.
4. Lugo T.G., Pendergast A.M., Muller A.J., Witte O.N. (1990). Tyrosine kinase activity and transformation potency of bcr-abl oncogene products. Science *247*, 1079-82.
5. Druker B.J., Tamura S., Buchdunger E., Ohno S., Segal G.M., Fanning S., Zimmermann J., Lydon N.B. (1996). Effects of a selective inhibitor of the Abl tyrosine kinase on the growth of Bcr-Abl positive cells. Nat Med *2*, 561-6.
6. Druker B.J., Talpaz M., Resta D.J., Peng B., Buchdunger E., Ford J.M., Lydon N.B., Kantarjian H., Capdeville R., Ohno-Jones S., et al. (2001). Efficacy and safety of a specific inhibitor of the BCR-ABL tyrosine kinase in chronic myeloid leukemia. N Engl J Med *344*, 1031-7.
7. Cohen P., Cross D., Jänne P.A. (2021). Kinase drug discovery 20 years after imatinib: progress and future directions. Nat Rev Drug Discov *20*, 551-569.
8. Soria J.C., Ohe Y., Vansteenkiste J., Reungwetwattana T., Chewaskulyong B., Lee K.H., Dechaphunkul A., Imamura F., Nogami N., Kurata T., et al. (2018). Osimertinib in Untreated EGFR-Mutated Advanced Non-Small-Cell Lung Cancer. N Engl J Med *378*, 113-125.
9. Paik P.K., Felip E., Veillon R., Sakai H., Cortot A.B., Garassino M.C., Mazieres J., Viteri S., Senellart H., Van Meerbeeck J., et al. (2020). Tepotinib in Non-Small-Cell Lung Cancer with MET Exon 14 Skipping Mutations. N Engl J Med *383*, 931-943.
10. Shaw A.T., Kim D.W., Mehra R., Tan D.S., Felip E., Chow L.Q., Camidge D.R., Vansteenkiste J., Sharma S., De Pas T., et al. (2014). Ceritinib in ALK-rearranged non-small-cell lung cancer. N Engl J Med *370*, 1189-97.
11. Soria J.C., Felip E., Cobo M., Lu S., Syrigos K., Lee K.H., Göker E., Georgoulias V., Li W., Isla D., et al. (2015). Afatinib versus erlotinib as second-line treatment of patients with advanced squamous cell carcinoma of the lung (LUX-Lung 8): an open-label randomised controlled phase 3 trial. Lancet Oncol *16*, 897-907.
12. Wolf J., Seto T., Han J.Y., Reguart N., Garon E.B., Groen H.J.M., Tan D.S.W., Hida T., de Jonge M., Orlov S.V., et al. (2020). Capmatinib in MET Exon 14-Mutated or MET-Amplified Non-Small-Cell Lung Cancer. N Engl J Med *383*, 944-957.
13. Shaw A.T., Bauer T.M., de Marinis F., Felip E., Goto Y., Liu G., Mazieres J., Kim D.W., Mok T., Polli A., et al. (2020). First-Line Lorlatinib or Crizotinib in Advanced ALK-Positive Lung Cancer. N Engl J Med *383*, 2018-2029.
14. Niederst M.J., Engelman J.A. (2013). Bypass mechanisms of resistance to receptor tyrosine kinase inhibition in lung cancer. Sci Signal *6*, re6.
15. Noronha A., Belugali Nataraj N., Lee J.S., Zhitomirsky B., Oren Y., Oster S., Lindzen M., Mukherjee S., Will R., Ghosh S., et al. (2022). AXL and Error-Prone DNA Replication Confer

Drug Resistance and Offer Strategies to Treat EGFR-Mutant Lung Cancer. Cancer Discov *12*, 2666-2683.

16. Isozaki H., Sakhtemani R., Abbasi A., Nikpour N., Stanzione M., Oh S., Langenbucher A., Monroe S., Su W., Cabanos H.F., et al. (2023). Therapy-induced APOBEC3A drives evolution of persistent cancer cells. Nature *620*, 393-401.
17. Pao W., Miller V., Zakowski M., Doherty J., Politi K., Sarkaria I., Singh B., Heelan R., Rusch V., Fulton L., et al. (2004). EGF receptor gene mutations are common in lung cancers from "never smokers" and are associated with sensitivity of tumors to gefitinib and erlotinib. Proc Natl Acad Sci U S A *101*, 13306-11.
18. Lynch T.J., Bell D.W., Sordella R., Gurubhagavatula S., Okimoto R.A., Brannigan B.W., Harris P.L., Haserlat S.M., Supko J.G., Haluska F.G., et al. (2004). Activating mutations in the epidermal growth factor receptor underlying responsiveness of non-small-cell lung cancer to gefitinib. N Engl J Med *350*, 2129-39.
19. Kwak E.L., Bang Y.J., Camidge D.R., Shaw A.T., Solomon B., Maki R.G., Ou S.H., Dezube B.J., Jänne P.A., Costa D.B., et al. (2010). Anaplastic lymphoma kinase inhibition in non-small-cell lung cancer. N Engl J Med *363*, 1693-703.
20. Oren Y., Tsabar M., Cuoco M.S., Amir-Zilberstein L., Cabanos H.F., Hütter J.C., Hu B., Thakore P.I., Tabaka M., Fulco C.P., et al. (2021). Cycling cancer persister cells arise from lineages with distinct programs. Nature *596*, 576-582.
21. Socinski M.A., Pennell N.A., Davies K.D. (2021). MET Exon 14 Skipping Mutations in Non-Small-Cell Lung Cancer: An Overview of Biology, Clinical Outcomes, and Testing Considerations. JCO Precis Oncol *5*, ePO.20.00516.
22. Soda M., Choi Y.L., Enomoto M., Takada S., Yamashita Y., Ishikawa S., Fujiwara S., Watanabe H., Kurashina K., Hatanaka H., et al. (2007). Identification of the transforming EML4-ALK fusion gene in non-small-cell lung cancer. Nature *448*, 561-6.
23. Qin Z., Sun H., Yue M., Pan X., Chen L., Feng X., Yan X., Zhu X., Ji H. (2021). Phase separation of EML4-ALK in firing downstream signaling and promoting lung tumorigenesis. Cell Discov *7*, 33.
24. Cerami E., Gao J., Dogrusoz U., Gross B.E., Sumer S.O., Aksoy B.A., Jacobsen A., Byrne C.J., Heuer M.L., Larsson E., et al. (2012). The cBio cancer genomics portal: an open platform for exploring multidimensional cancer genomics data. Cancer Discov *2*, 401-4.
25. da Cunha Santos G., Shepherd F.A., Tsao M.S. (2011). EGFR mutations and lung cancer. Annu Rev Pathol *6*, 49-69.
26. Tsherniak A., Vazquez F., Montgomery P.G., Weir B.A., Kryukov G., Cowley G.S., Gill S., Harrington W.F., Pantel S., Krill-Burger J.M., et al. (2017). Defining a Cancer Dependency Map. Cell *170*, 564-576.e16.
27. Li D., Ambrogio L., Shimamura T., Kubo S., Takahashi M., Chirieac L.R., Padera R.F., Shapiro G.I., Baum A., Himmelsbach F., et al. (2008). BIBW2992, an irreversible EGFR/HER2 inhibitor highly effective in preclinical lung cancer models. Oncogene *27*, 4702-11.
28. Hafner M., Niepel M., Chung M., Sorger P.K. (2016). Growth rate inhibition metrics correct for confounders in measuring sensitivity to cancer drugs. Nat Methods *13*, 521-7.

29. Sharma S.V., Lee D.Y., Li B., Quinlan M.P., Takahashi F., Maheswaran S., McDermott U., Azizian N., Zou L., Fischbach M.A., et al. (2010). A chromatin-mediated reversible drug-tolerant state in cancer cell subpopulations. Cell *141*, 69-80.
30. Dhanyamraju P.K., Schell T.D., Amin S., Robertson G.P. (2022). Drug-Tolerant Persister Cells in Cancer Therapy Resistance. Cancer Res *82*, 2503-2514.
31. Wolf-Yadlin A., Hautaniemi S., Lauffenburger D.A., White F.M. (2007). Multiple reaction monitoring for robust quantitative proteomic analysis of cellular signaling networks. Proc Natl Acad Sci U S A *104*, 5860-5.
32. UniProt Consortium. (2023). UniProt: the Universal Protein Knowledgebase in 2023. Nucleic Acids Res *51*, D523-D531.
33. Lutterbach B., Zeng Q., Davis L.J., Hatch H., Hang G., Kohl N.E., Gibbs J.B., Pan B.S. (2007). Lung cancer cell lines harboring MET gene amplification are dependent on Met for growth and survival. Cancer Res *67*, 2081-8.
34. Johnson H., Lescarbeau R.S., Gutierrez J.A., White F.M. (2013). Phosphotyrosine profiling of NSCLC cells in response to EGF and HGF reveals network specific mediators of invasion. J Proteome Res *12*, 1856-67.
35. Olsen J.V., Blagoev B., Gnad F., Macek B., Kumar C., Mortensen P., Mann M. (2006). Global, in vivo, and site-specific phosphorylation dynamics in signaling networks. Cell *127*, 635-48.
36. Ochoa D., Jarnuczak A.F., Viéitez C., Gehre M., Soucheray M., Mateus A., Kleefeldt A.A., Hill A., Garcia-Alonso L., Stein F., et al. (2020). The functional landscape of the human phosphoproteome. Nat Biotechnol *38*, 365-373.
37. Koivunen J.P., Mermel C., Zejnullahu K., Murphy C., Lifshits E., Holmes A.J., Choi H.G., Kim J., Chiang D., Thomas R., et al. (2008). EML4-ALK fusion gene and efficacy of an ALK kinase inhibitor in lung cancer. Clin Cancer Res *14*, 4275-83.
38. Skoulidis F., Heymach J.V. (2019). Co-occurring genomic alterations in non-small-cell lung cancer biology and therapy. Nat Rev Cancer *19*, 495-509.
39. Chakravarty D., Gao J., Phillips S.M., Kundra R., Zhang H., Wang J., Rudolph J.E., Yaeger R., Soumerai T., Nissan M.H., et al. (2017). OncoKB: A Precision Oncology Knowledge Base. JCO Precis Oncol *2017*, PO.17.00011.
40. Furet P., Guagnano V., Fairhurst R.A., Imbach-Weese P., Bruce I., Knapp M., Fritsch C., Blasco F., Blanz J., Aichholz R., et al. (2013). Discovery of NVP-BYL719 a potent and selective phosphatidylinositol-3 kinase alpha inhibitor selected for clinical evaluation. Bioorg Med Chem Lett *23*, 3741-8.
41. Folkes A.J., Ahmadi K., Alderton W.K., Alix S., Baker S.J., Box G., Chuckowree I.S., Clarke P.A., Depledge P., Eccles S.A., et al. (2008). The identification of 2-(1H-indazol-4-yl)-6-(4-methanesulfonyl-piperazin-1-ylmethyl)-4-morpholin-4-yl-thieno[3,2-d]pyrimidine (GDC-0941) as a potent, selective, orally bioavailable inhibitor of class I PI3 kinase for the treatment of cancer . J Med Chem *51*, 5522-32.
42. Niederst M.J., Sequist L.V., Poirier J.T., Mermel C.H., Lockerman E.L., Garcia A.R., Katayama R., Costa C., Ross K.N., Moran T., et al. (2015). RB loss in resistant EGFR mutant lung adenocarcinomas that transform to small-cell lung cancer. Nat Commun *6*, 6377.

43. Condorelli R., Spring L., O'Shaughnessy J., Lacroix L., Bailleux C., Scott V., Dubois J., Nagy R.J., Lanman R.B., Iafrate A.J., et al. (2018). Polyclonal RB1 mutations and acquired resistance to CDK 4/6 inhibitors in patients with metastatic breast cancer. Ann Oncol *29*, 640-645.
44. Gong X., Du J., Parsons S.H., Merzoug F.F., Webster Y., Iversen P.W., Chio L.C., Van Horn R.D., Lin X., Blosser W., et al. (2019). Aurora A Kinase Inhibition Is Synthetic Lethal with Loss of the RB1 Tumor Suppressor Gene. Cancer Discov *9*, 248-263.
45. Oser M.G., Fonseca R., Chakraborty A.A., Brough R., Spektor A., Jennings R.B., Flaifel A., Novak J.S., Gulati A., Buss E., et al. (2019). Cells Lacking the RB1 Tumor Suppressor Gene Are Hyperdependent on Aurora B Kinase for Survival. Cancer Discov *9*, 230-247.
46. Lyu J., Yang E.J., Zhang B., Wu C., Pardeshi L., Shi C., Mou P.K., Liu Y., Tan K., Shim J.S. (2020). Synthetic lethality of RB1 and aurora A is driven by stathmin-mediated disruption of microtubule dynamics. Nat Commun *11*, 5105.
47. Flower C.T., Liu C., Chuang H., Ye X., Cheng H., Heath J.R., Wei W., White F.M. (2024). Signaling and transcriptional dynamics underlying early adaptation to oncogenic BRAF inhibition. Preprint at bioRxiv, 2024.02.19.581004.
48. Jin H., Wang L., Bernards R. (2023). Rational combinations of targeted cancer therapies: background, advances and challenges. Nat Rev Drug Discov *22*, 213-234.
49. Jin L., Bi Y., Hu C., Qu J., Shen S., Wang X., Tian Y. (2021). A comparative study of evaluating missing value imputation methods in label-free proteomics. Sci Rep *11*, 1760.
50. O'Reilly K.E., Rojo F., She Q.B., Solit D., Mills G.B., Smith D., Lane H., Hofmann F., Hicklin D.J., Ludwig D.L., et al. (2006). mTOR inhibition induces upstream receptor tyrosine kinase signaling and activates Akt. Cancer Res *66*, 1500-8.
51. Shaffer S.M., Dunagin M.C., Torborg S.R., Torre E.A., Emert B., Krepler C., Beqiri M., Sproesser K., Brafford P.A., Xiao M., et al. (2017). Rare cell variability and drug-induced reprogramming as a mode of cancer drug resistance. Nature *546*, 431-435.
52. Yang C., Tian C., Hoffman T.E., Jacobsen N.K., Spencer S.L. (2021). Melanoma subpopulations that rapidly escape MAPK pathway inhibition incur DNA damage and rely on stress signalling. Nat Commun *12*, 1747.
53. Ercan D., Xu C., Yanagita M., Monast C.S., Pratilas C.A., Montero J., Butaney M., Shimamura T., Sholl L., Ivanova E.V., et al. (2012). Reactivation of ERK signaling causes resistance to EGFR kinase inhibitors. Cancer Discov *2*, 934-47.
54. Meyer A.S., Miller M.A., Gertler F.B., Lauffenburger D.A. (2013). The receptor AXL diversifies EGFR signaling and limits the response to EGFR-targeted inhibitors in triple-negative breast cancer cells. Sci Signal *6*, ra66.
55. Bahar M.E., Kim H.J., Kim D.R. (2023). Targeting the RAS/RAF/MAPK pathway for cancer therapy: from mechanism to clinical studies. Signal Transduct Target Ther *8*, 455.
56. Parker L.L., Atherton-Fessler S., Lee M.S., Ogg S., Falk J.L., Swenson K.I., Piwnica-Worms H. (1991). Cyclin promotes the tyrosine phosphorylation of p34cdc2 in a wee1^{+} dependent manner. EMBO J *10*, 1255-63.
57. Reynolds A.B., Kanner S.B., Wang H.C., Parsons J.T. (1989). Stable association of activated pp60src with two tyrosine-phosphorylated cellular proteins. Mol Cell Biol *9*, 3951-8.

58. Ngan E., Stoletov K., Smith H.W., Common J., Muller W.J., Lewis J.D., Siegel P.M. (2017). LPP is a Src substrate required for invadopodia formation and efficient breast cancer lung metastasis. Nat Commun *8*, 15059.
59. Zhao Y., Scott A., Zhang P., Hao Y., Feng X., Somasundaram S., Khalil A.M., Willis J., Wang Z. (2017). Regulation of paxillin-p130-PI3K-AKT signaling axis by Src and PTPRT impacts colon tumorigenesis. Oncotarget *8*, 48782-48793.
60. Thomas S.M., Brugge J.S. (1997). Cellular functions regulated by Src family kinases. Annu Rev Cell Dev Biol *13*, 513-609.
61. Roskoski R. (2015). Src protein-tyrosine kinase structure, mechanism, and small molecule inhibitors. Pharmacol Res *94*, 9-25.
62. Jin L.L., Wybenga-Groot L.E., Tong J., Taylor P., Minden M.D., Trudel S., McGlade C.J., Moran M.F. (2015). Tyrosine phosphorylation of the Lyn Src homology 2 (SH2) domain modulates its binding affinity and specificity. Mol Cell Proteomics *14*, 695-706.
63. Oughtred R., Rust J., Chang C., Breitkreutz B.J., Stark C., Willems A., Boucher L., Leung G., Kolas N., Zhang F., et al. (2021). The BioGRID database: A comprehensive biomedical resource of curated protein, genetic, and chemical interactions. Protein Sci *30*, 187-200.
64. Colicelli J. (2010). ABL tyrosine kinases: evolution of function, regulation, and specificity. Sci Signal *3*, re6.
65. Baruzzi A., Iacobucci I., Soverini S., Lowell C.A., Martinelli G., Berton G. (2010). c-Abl and Src-family kinases cross-talk in regulation of myeloid cell migration. FEBS Lett *584*, 15-21.
66. Wang J., Wang B., Chu H., Yao Y. (2016). Intrinsic resistance to EGFR tyrosine kinase inhibitors in advanced non-small-cell lung cancer with activating EGFR mutations. Onco Targets Ther *9*, 3711-26.
67. Mikubo M., Inoue Y., Liu G., Tsao M.S. (2021). Mechanism of Drug Tolerant Persister Cancer Cells: The Landscape and Clinical Implication for Therapy. J Thorac Oncol *16*, 1798-1809.
68. Labrie M., Brugge J.S., Mills G.B., Zervantonakis I.K. (2022). Therapy resistance: opportunities created by adaptive responses to targeted therapies in cancer. Nat Rev Cancer *22*, 323-339.
69. Camidge D.R., Pao W., Sequist L.V. (2014). Acquired resistance to TKIs in solid tumours: learning from lung cancer. Nat Rev Clin Oncol *11*, 473-81.
70. Shaw A.T., Kim D.W., Nakagawa K., Seto T., Crinó L., Ahn M.J., De Pas T., Besse B., Solomon B.J., Blackhall F., et al. (2013). Crizotinib versus chemotherapy in advanced ALK-positive lung cancer. N Engl J Med *368*, 2385-94.
71. Fedele C., Li S., Teng K.W., Foster C.J.R., Peng D., Ran H., Mita P., Geer M.J., Hattori T., Koide A., et al. (2021). SHP2 inhibition diminishes KRASG12C cycling and promotes tumor microenvironment remodeling. J Exp Med *218*, e211451.
72. Tian J., Chen J.H., Chao S.X., Pelka K., Giannakis M., Hess J., Burke K., Jorgji V., Sindurakar P., Braverman J., et al. (2023). Combined PD-1, BRAF and MEK inhibition in $BRAF^{V600E}$ colorectal cancer: a phase 2 trial. Nat Med *29*, 458-466.
73. Woo C.G., Seo S., Kim S.W., Jang S.J., Park K.S., Song J.Y., Lee B., Richards M.W., Bayliss R., Lee D.H., et al. (2017). Differential protein stability and clinical responses of EML4-ALK fusion variants to various ALK inhibitors in advanced ALK-rearranged non-small cell lung cancer. Ann Oncol *28*, 791-797.

74. Christopoulos P., Endris V., Bozorgmehr F., Elsayed M., Kirchner M., Ristau J., Buchhalter I., Penzel R., Herth F.J., Heussel C.P., et al. (2018). EML4-ALK fusion variant V3 is a high-risk feature conferring accelerated metastatic spread, early treatment failure and worse overall survival in ALK^+ non-small cell lung cancer. Int J Cancer *142*, 2589-2598.
75. Snyder J.R., Serianni A.S. (1988). Furanose ring anomerization: a kinetic study of the 5-deoxypentoses and 5-O-methylpentoses. Carbohydr Res *184*, 13-25.
76. Fallahi-Sichani M., Becker V., Izar B., Baker G.J., Lin J.R., Boswell S.A., Shah P., Rotem A., Garraway L.A., Sorger P.K. (2017). Adaptive resistance of melanoma cells to RAF inhibition via reversible induction of a slowly dividing de-differentiated state. Mol Syst Biol *13*, 905.
77. Emdal K.B., Dittmann A., Reddy R.J., Lescarbeau R.S., Moores S.L., Laquerre S., White F.M. (2017). Characterization of In Vivo Resistance to Osimertinib and JNJ-61186372, an EGFR/Met Bispecific Antibody, Reveals Unique and Consensus Mechanisms of Resistance. Mol Cancer Ther *16*, 2572-2585.
78. Hirata E., Girotti M.R., Viros A., Hooper S., Spencer-Dene B., Matsuda M., Larkin J., Marais R., Sahai E. (2015). Intravital imaging reveals how BRAF inhibition generates drug-tolerant microenvironments with high integrin β1/FAK signaling. Cancer Cell *27*, 574-88.
79. Kohale I.N., Yu J., Zhuang Y., Fan X., Reddy R.J., Sinnwell J., Kalari K.R., Boughey J.C., Carter J.M., Goetz M.P., et al. (2022). Identification of Src Family Kinases as Potential Therapeutic Targets for Chemotherapy-Resistant Triple Negative Breast Cancer. Cancers (Basel) *14*, ecancers14174220.
80. Zhu E.Y., Riordan J.D., Vanneste M., Henry M.D., Stipp C.S., Dupuy A.J. (2022). SRC-RAC1 signaling drives drug resistance to BRAF inhibition in de-differentiated cutaneous melanomas. NPJ Precis Oncol *6*, 74.
81. Alkhatib H., Conage-Pough J., Roy Chowdhury S., Shian D., Zaid D., Rubinstein A.M., Sonnenblick A., Peretz-Yablonsky T., Granit A., Carmon E., et al. (2024). Patient-specific signaling signatures predict optimal therapeutic combinations for triple negative breast cancer. Mol Cancer *23*, 17.
82. Takeda H., Kawamura Y., Miura A., Mori M., Wakamatsu A., Yamamoto J., Isogai T., Matsumoto M., Nakayama K.I., Natsume T., et al. (2010). Comparative analysis of human SRC-family kinase substrate specificity in vitro. J Proteome Res *9*, 5982-93.
83. Arrington J., Xue L., Wang W.H., Geahlen R.L., Tao W.A. (2019). Identification of the Direct Substrates of the ABL Kinase via Kinase Assay Linked Phosphoproteomics with Multiple Drug Treatments. J Proteome Res *18*, 1679-1690.
84. Knox C., Wilson M., Klinger C.M., Franklin M., Oler E., Wilson A., Pon A., Cox J., Chin N.E.L., Strawbridge S.A., et al. (2024). DrugBank 6.0: the DrugBank Knowledgebase for 2024. Nucleic Acids Res *52*, D1265-D1275.

Chapter 3:
Signaling and transcriptional dynamics underlying early adaptation to oncogenic BRAF inhibition

A major contributor to poor sensitivity to anti-cancer kinase inhibitor therapy is drug-induced cellular adaptation, whereby remodeling of signaling and gene regulatory networks permits a drug-tolerant phenotype. Here, we resolve the scale and kinetics of critical subcellular events following oncogenic kinase inhibition and preceding cell cycle re-entry, using mass spectrometry-based phosphoproteomics and RNA sequencing to monitor the dynamics of thousands of growth- and survival-related signals over the first minutes, hours, and days of oncogenc BRAF inhibition in human melanoma cells. We observed sustained inhibition of the BRAF-ERK axis, gradual downregulation of cell cycle signaling, and three distinct and reversible phase transitions toward quiescence. Statistical inference of kinetically-defined regulatory modules revealed a dominant compensatory induction of SRC family kinase (SFK) signaling promoted by reactive oxygen species, which rendered cells sensitive to co-treatment with an SFK inhibitor *in vitro* and *in vivo*, underscoring the translational potential for assessing early drug-induced adaptive signaling.

The work presented in this chapter constitutes a research article which, as of the writing of this thesis, is under peer review and is freely available on *bioRxiv* (along with Supplementary Tables S1-S4) at the following DOI: 10.1101/2024.02.19.581004. This work was a collaborative effort between the following authors:

Cameron T. Flower[1,2,3,*], Chunmei Liu[4,*], Hui-Yu Chuang[4], Xiaoyang Ye[4], Hanjun Cheng[4], James R. Heath[4,†], Wei Wei[4,†], Forest M. White[1,2,3,†]

[1]Center for Precision Cancer Medicine, Koch Institute for Integrative Cancer Research, Massachusetts Institute of Technology, Cambridge, MA

[2]Department of Biological Engineering, Massachusetts Institute of Technology, Cambridge, MA

[3]Program in Computational and Systems Biology, Massachusetts Institute of Technology, Cambridge, MA

[4]Institute for Systems Biology, Seattle, WA

*These authors contributed equally to this study.

[†]These authors jointly supervised this study.

Chapter 3

Introduction

Cellular adaptation to exogenous sources of stress is driven by coordinated changes in cell state, often involving interactions between hundreds of distinct genes and proteins over diverse timescales. In the case of oncoprotein inhibition in cancer by targeted therapy treatment, such responses can promote rapid adaptation to drug, enabling survival of tumor cells and treatment failure.[1,2,3,4] A well-studied example of this phenomenon is the response to receptor tyrosine kinase (RTK)-RAS-ERK pathway inhibitors in certain cancers, where decreased activity of the target kinase can potentiate other mitogenic signaling proteins due to reduced negative-regulatory feedback.[5,6] Notably, such adaptive processes often unfold on timescales that are inconsistent with selection of (epi)genetically resistant subclones, but can influence eventual selection by defining new heritable cell states or promoting endogenous hypermutagenic processes, thereby promoting long-term acquired resistance.[7,8] Understanding early adaptive responses to therapy can yield promising new combination therapies which block compensatory signaling axes, preventing tumor cells from persisting and driving disease progression.[9]

Examinations of the signaling responses to targeted therapy have yielded valuable insights into the biochemical drivers of drug tolerance and cancer cell persistence. However, many efforts to date have focused on interrogating particular pathways of interest based on prior knowledge, further emphasizing these pathways' importance in drug adaptation but leaving most adaptive signaling mechanisms underexplored. In principle, adaptation to exogenous perturbation may involve the remodeling of multiple complex signaling networks over unpredictable timescales; capturing such network remodeling requires methods for time-resolved quantitation of systems-level signaling networks.[10,11] While large-scale 'hypothesis-free' efforts have gained traction in recent years with the falling costs of next-generation sequencing and mass spectrometry (MS)-based proteomics, the dynamics associated with early adaptation to targeted therapy have remained poorly resolved, as most reported hypothesis-free studies to date have profiled with low temporal granularity under drug treatment or have focused on the events following cell cycle re-entry. Here, we performed a time-resolved analysis of early adaptive signaling using a patient-derived cell line of *BRAF*^{V600E}-mutant melanoma, which is characterized by an incomplete response to BRAF inhibitor therapy and therefore serves as a prototypical model system to chart the early molecular events that permit cancer cell survival following oncogenic signaling blockade. Prior work has established the propensity of these cells to undergo substantial transcriptional, epigenetic, and metabolic remodeling under continued BRAF inhibition, promoting survival and eventual slow re-cycling under drug.[12,13,14,15,16] However, the links between these events and loss of BRAF kinase activity, as well as the intricacies of how cell-wide signaling networks contribute to the onset of drug adaptation within the initial days of exposure, remain unclear. To address this knowledge

gap, we used quantitative MS to monitor the temporal dynamics of thousands of protein phosphorylation sites over a three-day period of BRAF inhibition, followed by a six-day drug washout, to assemble and explore a highly detailed map of cellular signaling kinetics under targeted therapy treatment.

Results

Profiling signaling network dynamics in a patient-derived melanoma model of adaptive BRAF inhibitor resistance

To examine the early adaptive response to targeted therapy exposure, we studied a patient-derived melanoma cell line, M397, that has previously been shown to exhibit tolerance to BRAF inhibition despite harboring the *BRAF*^{V600E} oncogenic mutation.[12,13,14,15,16] We confirmed M397 cells exhibit a biphasic viability response to the BRAF inhibitor vemurafenib (VEM) after 72 hours; within the first response phase, the concentration of VEM necessary to attain half-maximal viability (EC_{50}, 98.37 ± 5.41 nM, mean ± standard deviation) was within range of the reported IC_{50} of VEM for BRAF (32 nM and 100 nM against mutant- and wild-type BRAF, respectively[17]), consistent with an on-target response (Figure 3.1A). Significantly higher doses of VEM (>30 μM) drove cell death presumably through substantial off-target activity, and significantly lower doses (<10 nM) induced a hormetic effect that has previously been linked to paradoxical activation of BRAF.[18] At a dose centered between the two response phases (3 μM), cells fail to apoptose and instead show a growth-arrested phenotype beginning at 30 hours (Figures 3.1B and 3.2A), indicating the suitability of M397 as a model system for studying the mechanisms of survival and early adaptation to oncogenic kinase inhibition.

Treatment of *BRAF*-mutant cells with high-dose VEM is expected to rapidly ablate the BRAF-ERK axis and drive widespread remodeling of subcellular signaling networks. To examine this response, we treated M397 cells with VEM at 3 μM in biological triplicate and harvested from culture at seven early timepoints, spanning 15 minutes to 72 hours (Figure 3.1C and Supplementary Table S1). A separate group of cells were treated with 0.1% (v/v) of drug solvent dimethyl sulfoxide (DMSO) and harvested at a subset of the timepoints. After cells had been exposed to VEM for 72 hours, drugged media was replaced with drug-free media for six additional days; this drug washout period allowed us to assess the reversibility of adaptation. All lysates were then subjected to multiplexed quantitative phosphoproteomics by MS using tandem mass tags (see Appendix B for methods details). We chose to prioritize particular kinase families known to mediate survival, cycling, and adaptation to stress including tyrosine kinases, DNA damage-sensing kinases, mitogen-activated protein kinases (MAPKs), and cyclin-dependent kinases (CDKs). To increase the probability of detection and accurate quantitation of the substrates of

these kinases by MS, their corresponding phospho-motifs were serially immunoprecipitated from the pool of TMT-labeled tryptic peptides prior to MS analysis (Figure 3.2B). A total of 4,160 phosphopeptides covering 4,088 phosphorylation sites were confidently identified and quantified, and 1,461 sites were detected in all three independent replicates (1,273 sites when counting multi-phosphorylated and non-unique peptide mappings as single sites).

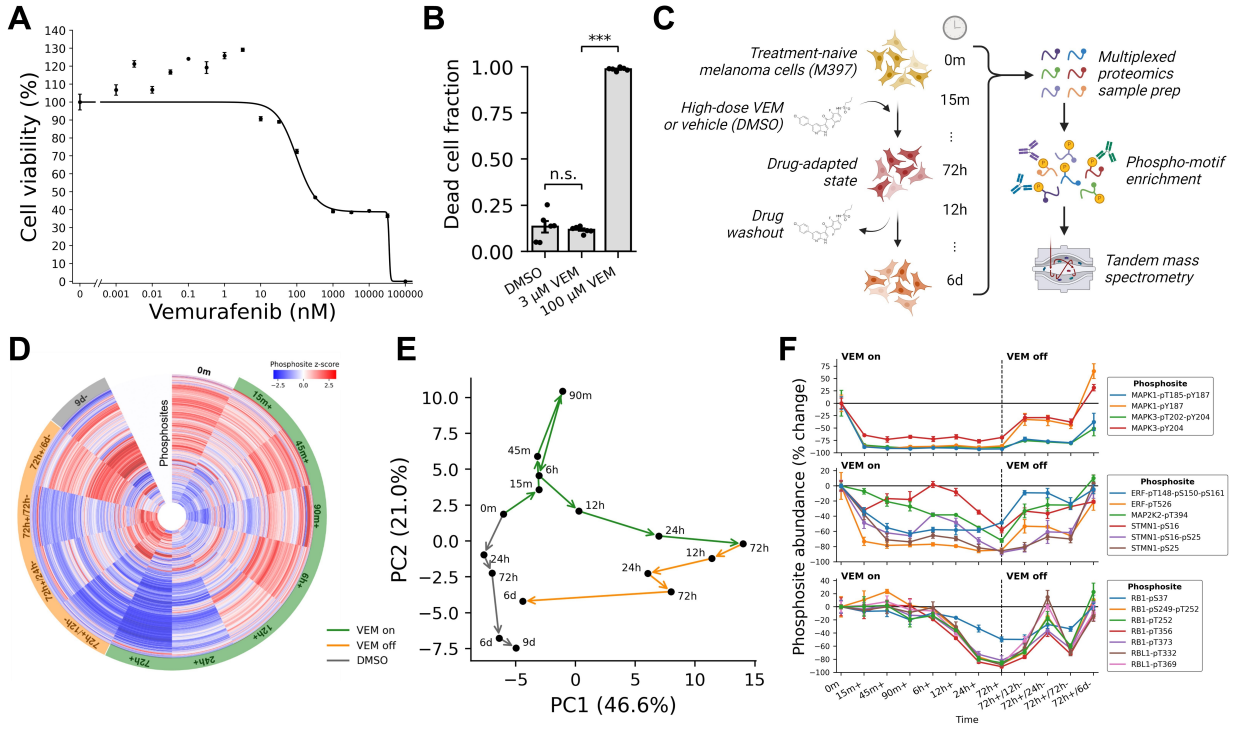

Figure 3.1. Early signaling dynamics of oncogenic BRAF inhibition in melanoma cells

A. Viability dose-response of a patient-derived *BRAF*-mutant melanoma cell line, M397, against BRAF inhibitor vemurafenib (VEM). Error bars depict standard error of the mean across three replicates.
B. Fraction of dead cells (staining positive for trypan blue) under high doses of VEM. Measurements were collected 72 hours after drug treatment. Error bars depict standard error of the mean across three replicates. *** : $P < 0.005$ by two-sided *t*-test.
C. Time-resolved phosphoproteomics workflow schematic.
D. Protein phosphorylation dynamics under BRAF inhibition by high-dose VEM (3 μM). Abundance values were derived from the mean across three biological replicates followed by z-score normalization. Phosphosites with no change throughout the time course (<10% coefficient of variation across timepoints, 108 total) are absent from this visual.
E. Principal components analysis (PCA) of phosphoproteome dynamics.
F. Phosphosite dynamics of MAPK1 and MAPK3 (ERK2 and ERK1, respectively) (top), canonical ERK1/2 substrates (middle), and RB1/L1 (bottom). Error bars depict standard error of the mean across three replicates.

The time-resolved phosphoproteome showed a rapid response to BRAF inhibition within 15 minutes followed by waves of distinct signaling network remodeling and recovery (Figure 3.1D). Principal components analysis (PCA) of the phosphoproteomics data revealed an early (0

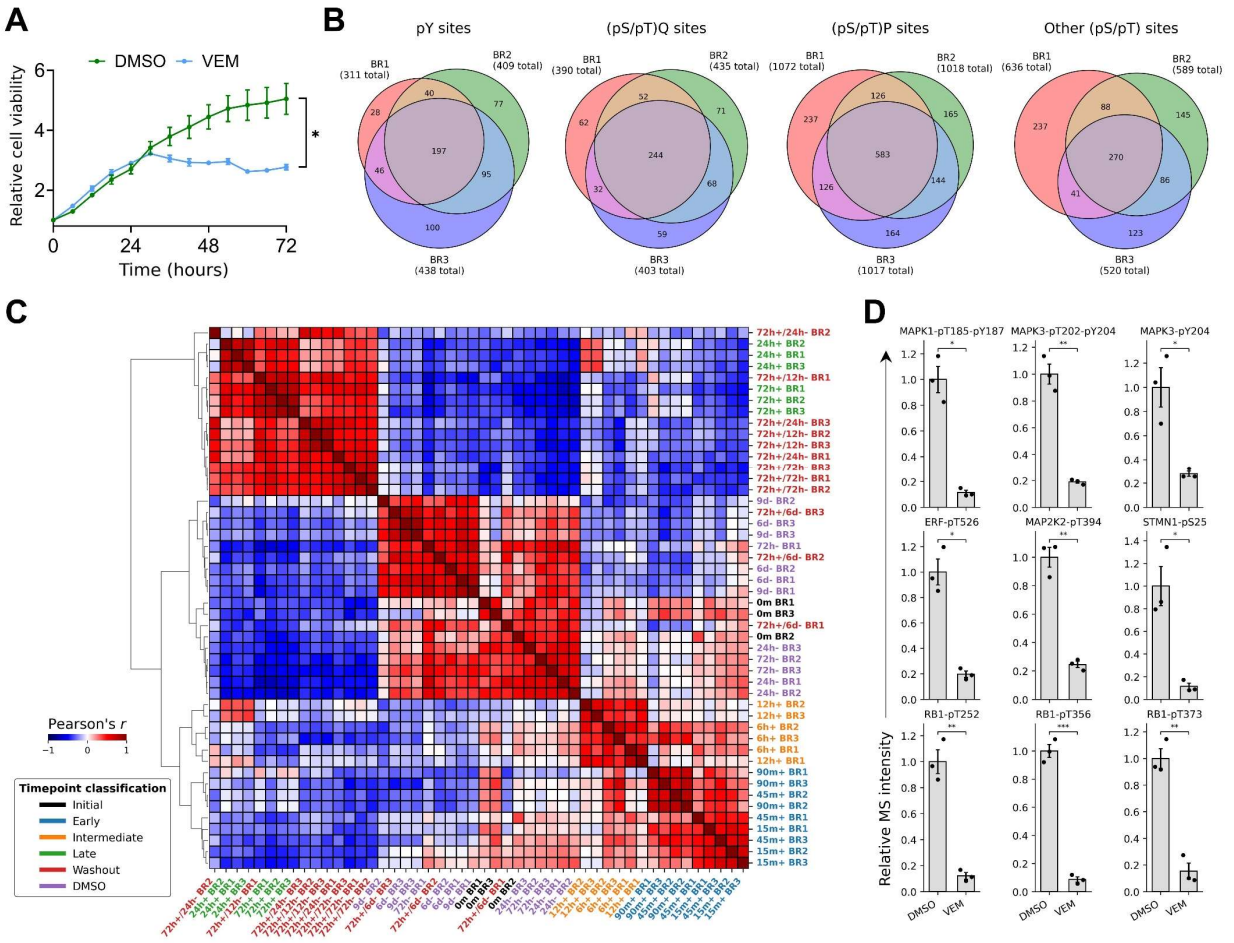

Figure 3.2. Growth and signaling characteristics of M397 melanoma cells under BRAF inhibition, related to Figure 3.1

A. Viability of melanoma cells under 0.1% DMSO or 3 μM VEM over a three-day time course. Error bars depict standard error across three replicates. * : $P < 0.05$ by two-sided Welch's *t*-test.
B. Number of high-confidence phosphosite identifications by phosphoproteomics. Values are reported for each biological replicate, each of which constitutes a single multiplexed MS analysis, and are segregated by each serially-enriched phospho-motif.
C. Pairwise sample correlation and hierarchical clustering derived from phosphoproteomic data.
D. Abundances of phosphosites on MAPK1 and MAPK3 (ERK2 and ERK1, respectively) (top), canonical ERK1/2 substrates (middle), and RB1 (bottom) at 72 hours under VEM or DMSO. Error bars depict standard error of the mean across three replicates. * : $P < 0.05$; ** : $P < 0.01$; *** : $P < 0.005$; by two-sided *t*-test with multiple hypothesis correction by the Benjamini-Hochberg procedure.

to 90 minutes) response to VEM along principal component 2, followed by a delayed (90 minutes to 72 hours) response along principal component 1 which was almost fully reversed following six days of drug removal (Figure 3.1E). Under drug washout, cells traverse a distinct path through principal component space which terminates near the matched DMSO control samples, indicating the controls successfully captured the signaling changes associated with sustained culture and low-level DMSO exposure. Pairwise correlation analysis followed by hierarchical clustering between

all samples showed strong consistency between biological replicates and revealed three distinct timescales of drug response: 'early' (15 to 90 minutes), 'intermediate' (6 to 12 hours), and 'late' (24 to 72 hours) (Figure 3.2C). Notably, all drug washout samples co-cluster with 'late' timepoints, with the exception of the final washout timepoint (72h+/6d- BR1-3) which co-clusters with 'basal' samples, indicating a heavily delayed but nevertheless reversible signaling response.

The ERK MAPKs, MAPK1 (ERK2) and MAPK3 (ERK1), which are canonically activated downstream of active BRAF, were rapidly and durably inhibited by VEM treatment throughout the time course until drug removal, as measured by activation loop phosphorylation (Figures 3.1F and 3.2D, top) and by phosphorylation of canonical ERK1/2 substrates (Figures 3.1F and 3.2D, middle). The inhibition of ERK1/2 within 15 minutes of VEM exposure confirms successful drug-target engagement, and the durability of inhibition suggests M397 cells are not dependent on reactivation of the RAF-ERK axis to survive high-dose VEM treatment, in contrast to observations of rapid ERK1/2 reactivation in some cancers treated with RTK-RAS-ERK pathway inhibitors.[5,6,19]

Activation of CDKs, especially CDK4/6, canonically occurs downstream of ERK1/2 activation and promotes entry into S-phase in part by hyperphosphorylation of RB1.[20] We observed gradual downregulation of seven phosphosites on RB1 and the related protein RBL1 under VEM, and recovery under drug washout, consistent with reversible cell cycle arrest at G1-phase (Figures 3.1F and 3.2D, bottom). These findings confirm that our molecular snapshots capture drug-tolerant cells in a period of transient, reversible stress driven by oncogenic kinase inhibition and further support the M397 model's utility for scrutinizing the dynamics of early drug adaptation.

The time-resolved transcriptome informs dynamic gene regulatory responses to oncogenic BRAF inhibition

Changes in cellular signaling network activity often lead to widespread transcriptional remodeling. To characterize concomitant transcriptomic alterations following signaling network rewiring, we subjected VEM-treated M397 cells to bulk mRNA sequencing (RNA-seq) at select timepoints (Supplementary Table S2). PCA of the time-resolved transcriptome showed strong overall agreement with the phosphoproteome, highlighting immediate-early responses along principal component 1, delayed responses along principal component 2, and a near-complete reversal of the adaptive response during drug washout (Figure 3.3A). These transitions were characterized by changes in proliferation, metabolism, and stemness along two distinct timescales with a clear transition point at 24 hours. Notably, mRNA transcripts of canonical targets downstream of ERK1/2 signaling showed reduced abundance under VEM and recovery under drug

washout, consistent with the durable and reversible ERK1/2 inhibition observed in the phosphoproteome (Figure 3.3B).

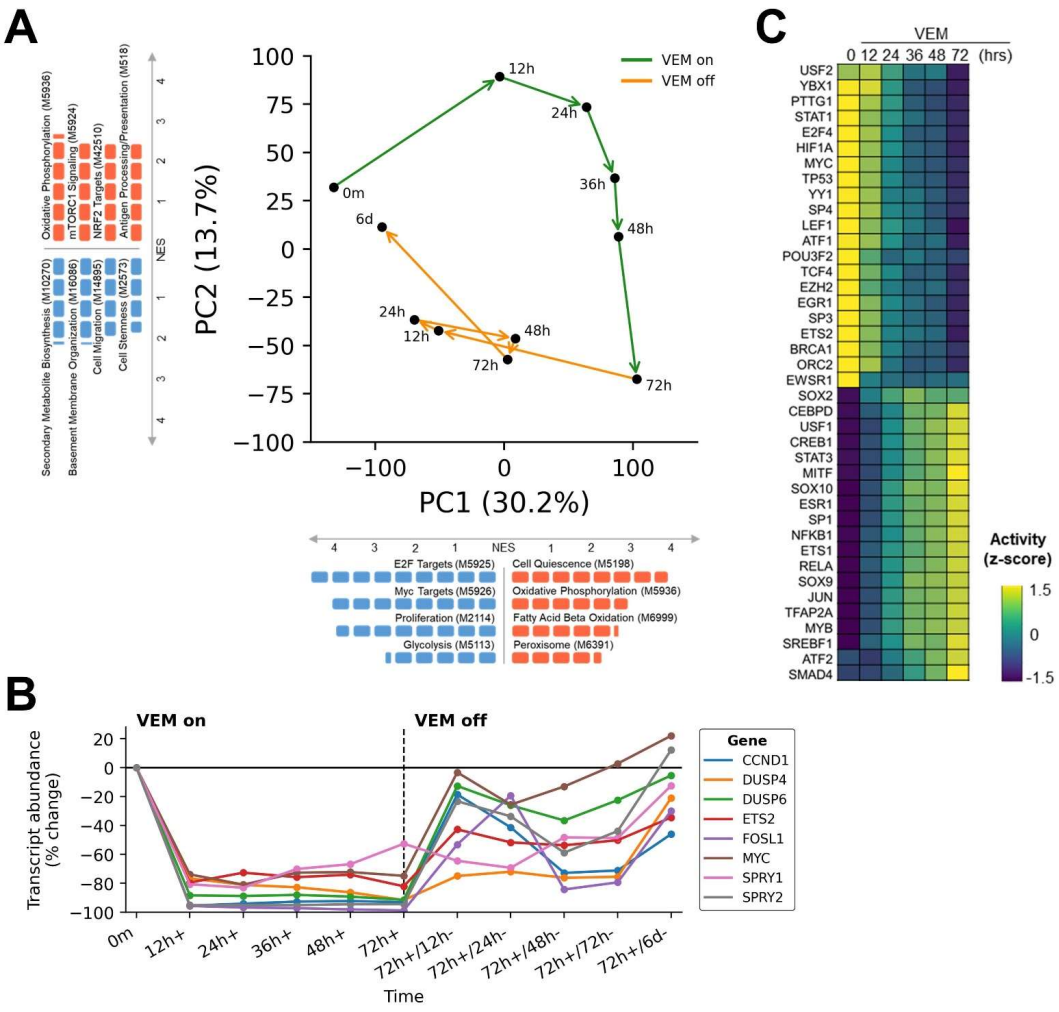

Figure 3.3. Transcriptional dynamics of oncogenic BRAF inhibition

A. Principal components analysis (PCA) of transcriptome dynamics under high-dose VEM (3 μM), and a subset of significantly enriched gene sets (FDR < 0.05) along each principal component. NES: normalized enrichment score.
B. mRNA dynamics of canonical downstream transcriptional targets of the RAS-ERK pathway.
C. Inferred transcription factor activity dynamics under VEM.

We performed computational inference of transcription factor (TF) activity to examine the dynamic gene regulatory consequences of oncogenic BRAF inhibition. Estimates of the relative activity of TFs using the time-series RNA-seq data revealed escalating activity of MITF, SOX9, and SOX10 under VEM, alongside diminishing activity of E2F4, HIF1A, MYC, TP53, and ETS2, aligning with an augmented melanocytic signature, attenuated ERK1/2 activity, and cell cycle

arrest upon short-term BRAF inhibition (Figure 3.3C).[12,21] We further discerned increased TF activities of NFκB and JUN/AP1, corroborating previous reports.[16,22,23] Construction of a TF regulatory network, using the correlative interactions among TFs whose activities changed significantly within the three days of drug exposure, spotlighted the known mutually activating interactions among the melanocytic lineage TFs MITF, SOX9, and SOX10, in addition to mutually inhibitory interactions between MYC and JUN, and between MYC and NFκB/RelA (Figure 3.4),[16,22,24,25,26] further validating our measurements of the early drug-altered transcriptome.

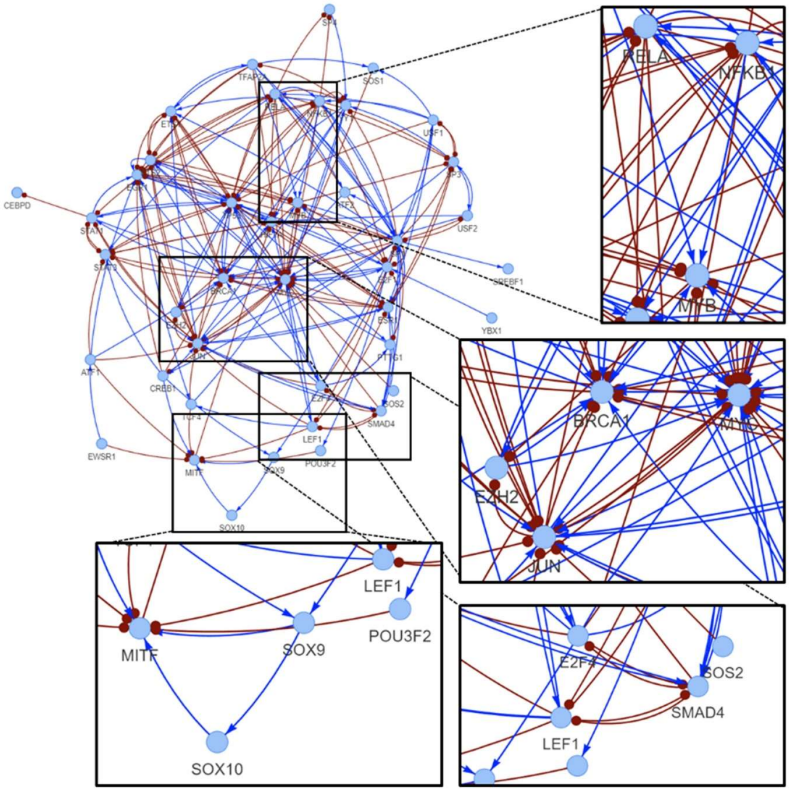

Figure 3.4. Remodeling of gene regulation by VEM, related to Figure 3.3

Inferred transcription factor regulatory network under VEM treatment for 72 hours, with representative zoomed-in sections. Blue lines and arrowheads signify gene activation; red lines and blunt heads signify gene inhibition.

Integrative analysis reveals the concerted signaling and transcriptional responses to BRAF inhibition

In general, signaling and transcription constitute tightly interconnected processes. Leveraging the time resolution of our multimodal data, we performed an integrative, correlation-based analysis to examine the coordinated network responses to BRAF inhibition. We subjected the phosphoproteomics and transcriptomics data separately to pairwise correlation analysis followed by hierarchical clustering, resulting in data-driven groupings of phosphosites (Figure

3.5A) and genes (Figure 3.5B). As each module consists of dozens to hundreds of features which share a kinetically similar response to VEM treatment and removal (Figures 3.6A and 3.6B), this analysis served as a form of dimensionality reduction, projecting both datasets into an interpretable kinetically-defined space. Upon examining meta-correlations between inferred signaling and transcriptional modules (Figure 3.6C), we found our approach detected known ground-truth associations between signaling and transcription; for instance, signaling module A (hereafter, SM-A), which contained phosphosites important for ERK1/2 signaling, was significantly correlated with transcriptional module L (hereafter, TM-L), a growth-enriched module with significant overrepresentation of downstream effectors of canonical RAS-ERK signaling (Figure 3.5C). SM-A was also significantly anticorrelated with transcription module E (TM-E), which was gradually induced by VEM and overwhelmingly represented genes associated with metabolic rewiring, especially fatty acid and lipid metabolism, consistent with the established role of ERK1/2 in repressing expression of fatty acid β-oxidation genes.[27,28] Another pair of independently inferred modules, SM-I and TM-J, were downregulated by VEM with near-identical kinetics and were both strongly associated with cell cycle progression and RNA processing (Figure 3.6D). These findings collectively validate our statistical framework for detecting positive and negative functional links between signaling networks and gene regulation.

While many of the proteins in the observed phosphoproteome are known to play important functional roles in processes enriched within the correlated transcriptome, most of their phosphorylation sites are poorly characterized. For example, EIF3B is a translation initiation factor that engages the 40S ribosome and is thought to be required for several of the initial steps of protein synthesis, but the precise functional role of the phosphorylation site quantified in SM-I (pS95) is unknown. As the vast majority of the phosphoproteome still lacks confidently annotated functional roles,[29] this time-resolved map between signaling dynamics and transcriptional remodeling under a well-controlled perturbation may serve as an information-rich resource to nominate mechanistic hypotheses with phosphosite-specific resolution.

BRAF inhibition induces early tyrosine kinase signaling and cytoskeletal remodeling

While most of the detected protein phosphorylation sites were downregulated by VEM, we found two signaling modules, SM-J and SM-K, which were reversibly induced rather than inhibited by VEM treatment (Figure 3.7A). Among all phosphosites in these modules, we observed significant depletion of the (pS/pT)P phospho-motif, consistent with reduced MAPK and CDK activity, and significant overrepresentation of phosphotyrosine, suggesting a net increase in tyrosine kinase activity under VEM (Figures 3.7B and 3.7C).

Upon inspection of the tyrosine-phosphorylated members of SM-J and SM-K, we found that many are known substrates of one or more SRC family kinases (SFKs) (Figure 3.7D and Sup-

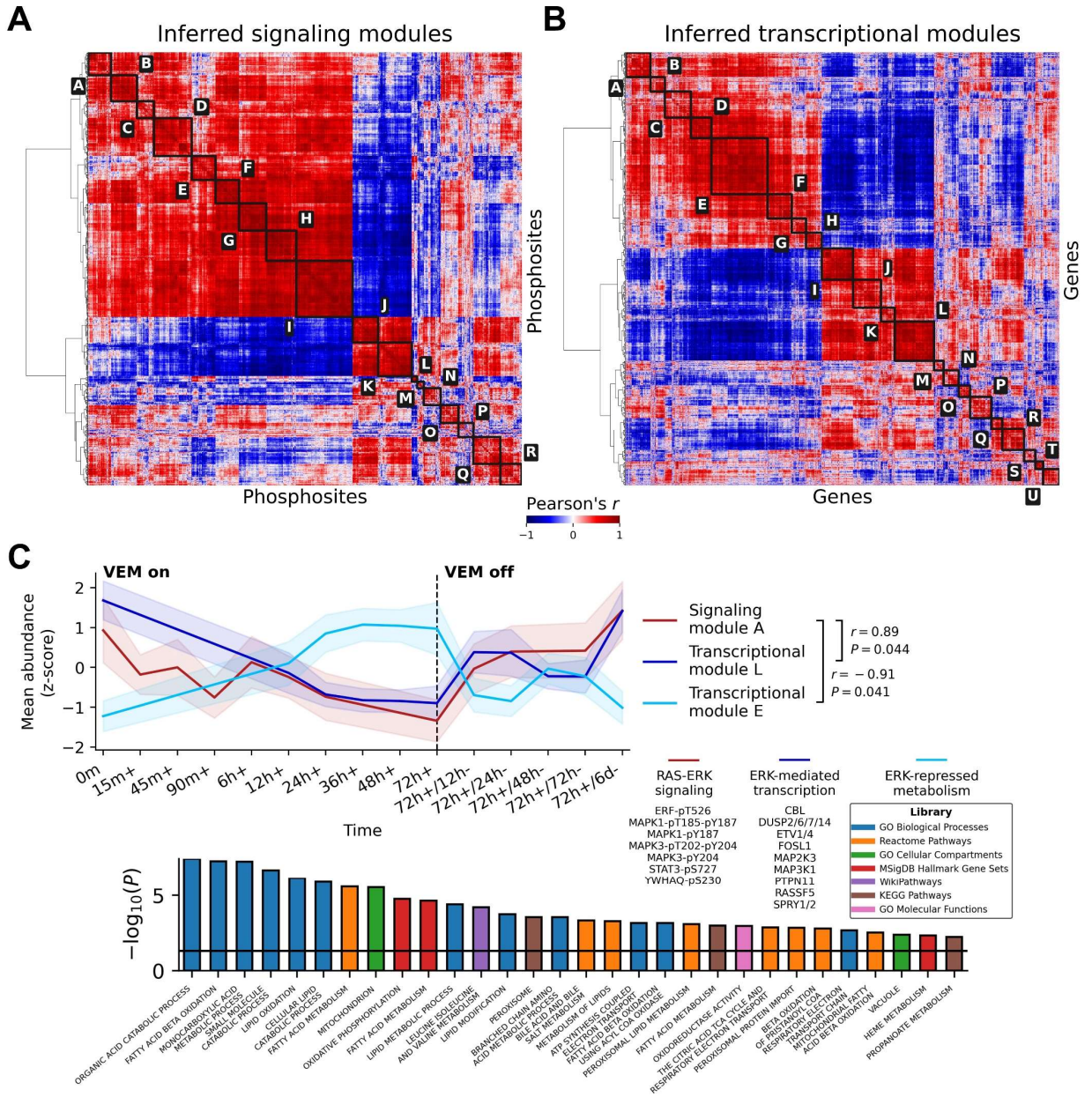

Figure 3.5. Integrative analysis reveals the concerted molecular response to VEM

A. Inference of kinetically distinct signaling modules from time-series phosphoproteomics data by pairwise correlation analysis and hierarchical clustering.

B. Inference of kinetically distinct transcription modules from time-series transcriptomics data by pairwise correlation analysis and hierarchical clustering.

C. Consensus dynamics of signaling module I and transcription module J under VEM (top left); phosphosites in signaling module I related to cell cycle progression and RNA processing (top right); overrepresented gene sets in transcription module J related to cell cycle progression and RNA processing (bottom). Shaded regions depict standard deviation across all members of the depicted module. *P*-values were derived from two-sided Fisher's exact test with multiple hypothesis correction by the Benjamini-Hochberg procedure.

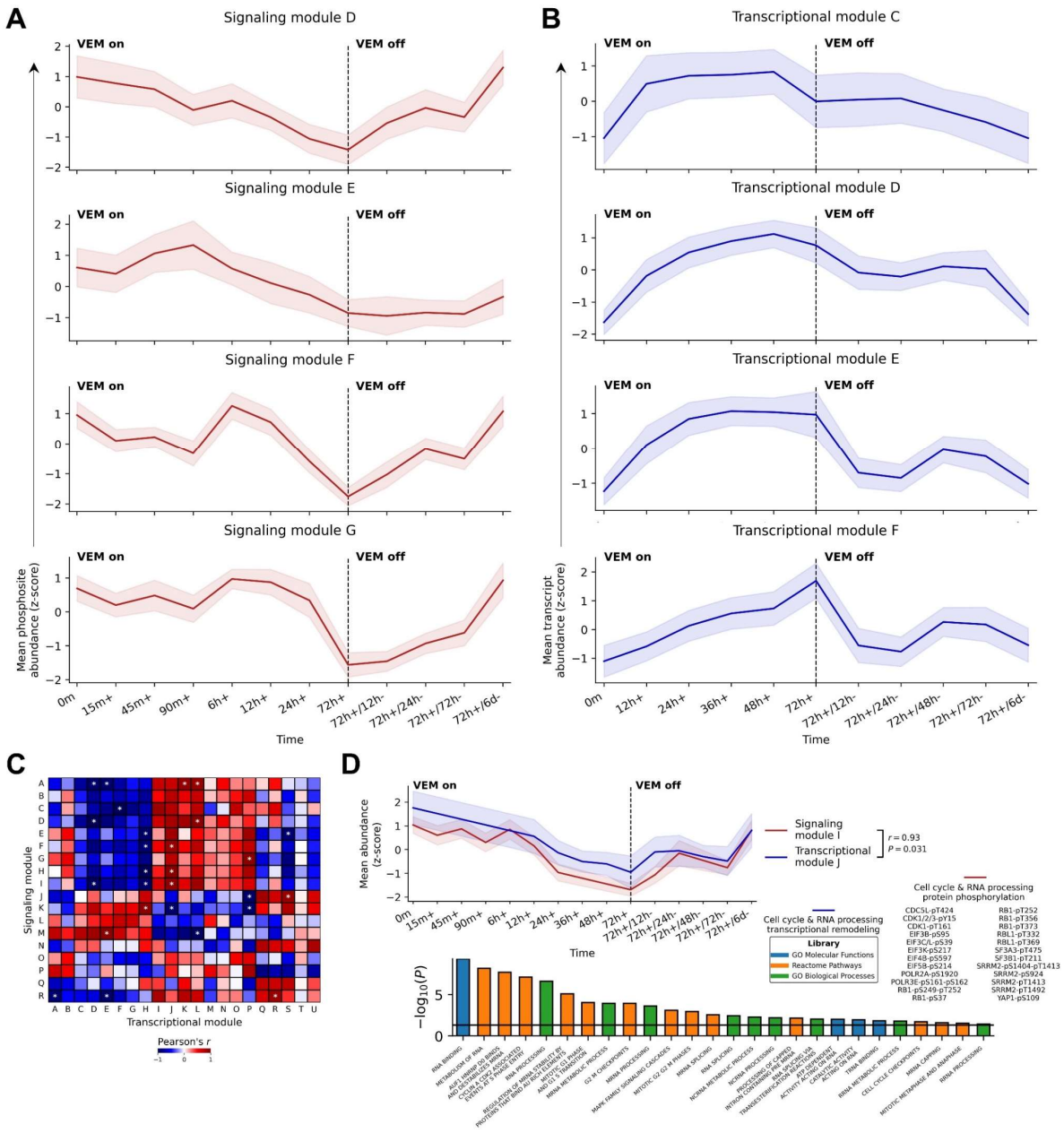

Figure 3.6. Integrative analysis of signaling and transcriptional response to BRAF inhibition, related to Figure 3.5

A. Consensus dynamics of qualitatively similar but kinetically distinct signaling modules D-G under VEM. Shaded regions depict standard deviation across all members of the depicted module.

B. Consensus dynamics of qualitatively similar but kinetically distinct transcription modules C-F under VEM. Shaded regions depict standard deviation across all members of the depicted module.

C. Pairwise correlation of signaling and transcription modules. * : $P < 0.05$. *P*-values indicate the estimated probability of uncorrelated modules producing an *r* value at least as extreme as the observed value, with multiple hypothesis correction by the Benjamini-Hochberg procedure.

D. Consensus dynamics of signaling module A and transcription module E under VEM (top left); phosphosites related to ERK1/2 pathway signaling in signaling module A (top right); overrepresented gene sets in transcription module E related to metabolic rewiring and fatty acid oxidation (bottom). Shaded regions depict standard deviation across all members of the depicted module. *P*-values were derived from two-sided Fisher's exact test with multiple hypothesis correction by the Benjamini-Hochberg procedure.

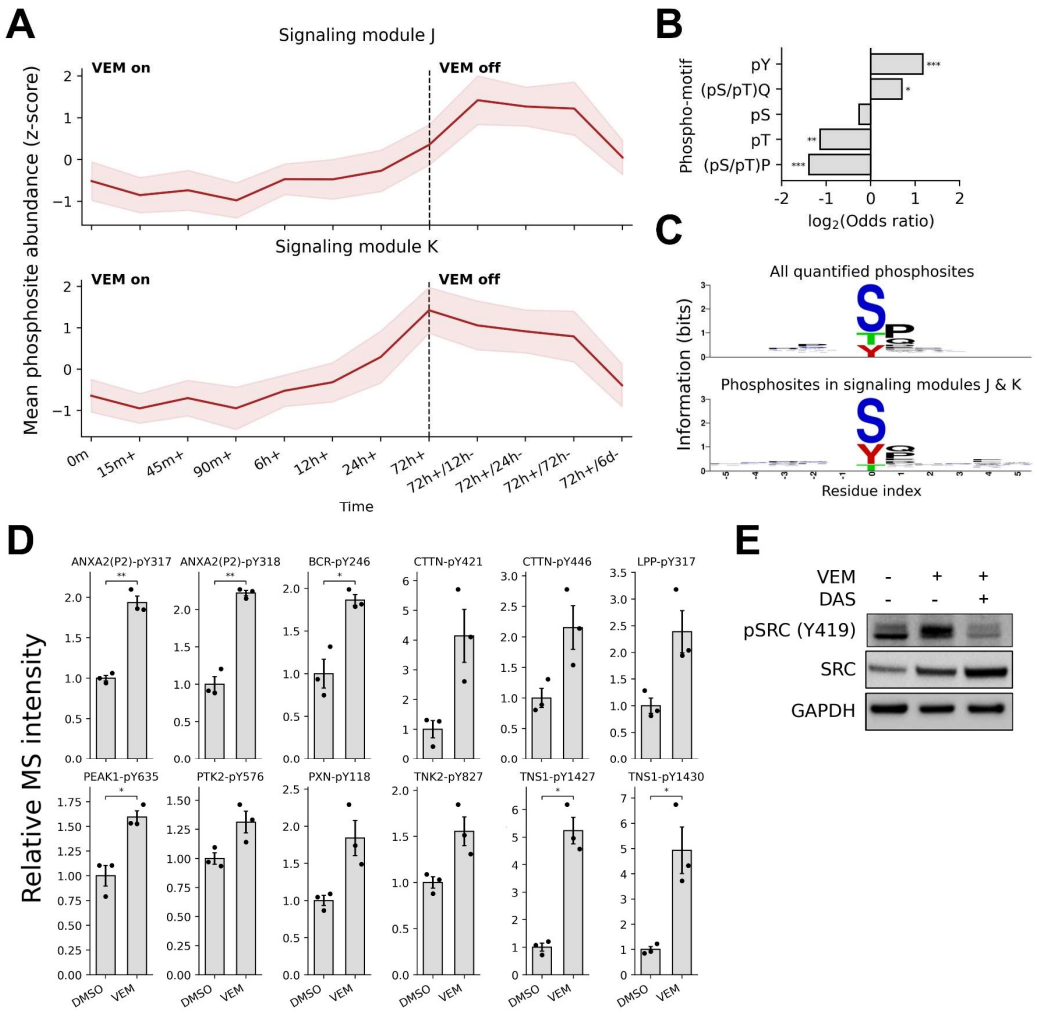

Figure 3.7. BRAF inhibition leads to an increase in tyrosine phosphorylation, SRC family kinase (SFK) signaling, and cytoskeletal remodeling

A. Consensus dynamics of VEM-induced signaling modules J (top) and K (bottom). Shaded regions depict standard deviation across all phosphosites in the depicted module.
B. Representation of each immunoprecipitated phospho-motif among phosphosites in signaling modules J and K. * : $P < 0.05$; ** : $P < 0.01$; *** : $P < 0.005$ by two-sided Fisher's exact test with multiple hypothesis correction by the Benjamini-Hochberg procedure.
C. Consensus sequence logos flanking all phosphosites in the phosphoproteomics data (top) and phosphosites in signaling modules J and K (bottom). Multi-phosphorylated peptides were excluded from the sequence logos.
D. Abundances of phosphosites on known substrates of SFKs at 72 hours under VEM or DMSO. Error bars depict standard error of the mean across three replicates. * : $P < 0.05$; ** : $P < 0.01$ by two-sided *t*-test with multiple hypothesis correction by the Benjamini-Hochberg procedure.
E. Immunoblot of phosphorylated SRC activation loop and total SRC under VEM alone and in combination with SFK inhibitor dasatinib (DAS).

plementary Table S3). SFKs constitute a group of non-receptor tyrosine kinases that coordinate important signaling events regulating cell morphology, survival, and metabolism, among many

other biological processes, and have been linked to adaptation and resistance to targeted therapy.[30,31,32,33] Many of these phosphosites, in addition to other known SFK substrates which were not in SM-J or SM-K, were upregulated under VEM treatment after 72 hours compared to DMSO-treated cells, suggesting their induction was not a consequence of sustained culture. Notably, some of these sites did not show corresponding increases in transcript abundance, indicating that VEM treatment modulates SFK signaling by mechanisms that are at least partly uncoupled from transcriptional upregulation (Figure 3.8A).

By western blot, we observed increased phosphorylation of the SRC activation loop at Y419 after treatment with VEM (3 μM) for 72 hours, which was prevented by co-treatment with the SFK inhibitor dasatinib (DAS) (Figure 3.7E). Consistent with the critical role of SFK signaling in regulation of the cytoskeleton and focal adhesions, cells showed marked changes in morphology under VEM treatment (Figure 3.8B). These results, together with our observation of SFK substrate kinetics, suggest that VEM treatment drives a gradual increase in SFK activity within the first three days of treatment.

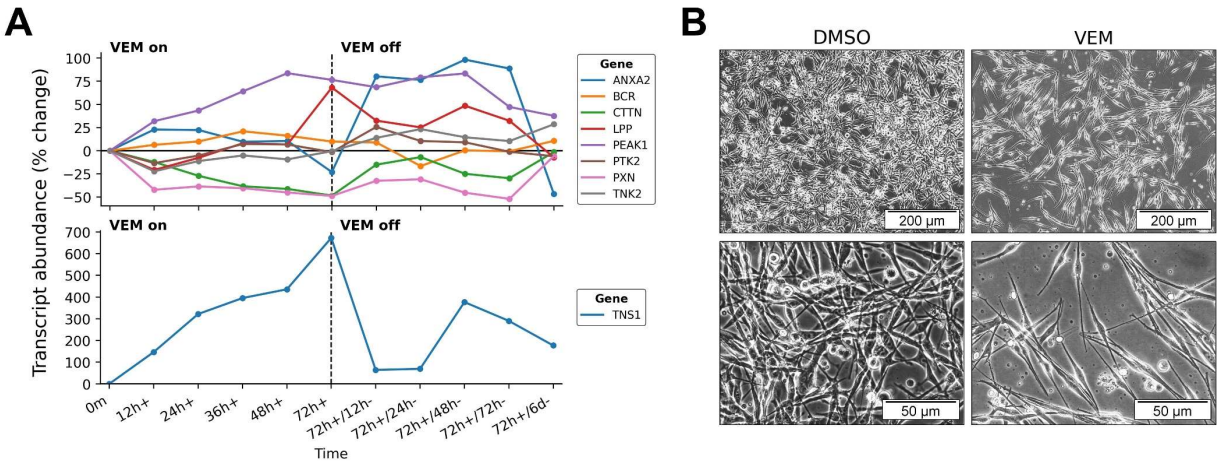

Figure 3.8. Transcriptional dynamics of SFK substrates and morphological characteristics under BRAF inhibition, related to Figure 3.7

A. mRNA dynamics of SFK substrate genes shown in Figure 3.7D.
B. Morphology of M397 cells under DMSO or VEM for 72 hours.

Accumulation of reactive oxygen species under BRAF inhibition promotes SFK signaling

Signaling through SFKs is complex and is known to be driven by many possible cell-intrinsic and extrinsic factors. One known mechanism for SFK activation under cell stress is through accumulation of reactive oxygen species (ROS), such as hydrogen peroxide (H2O2), which can oxidize catalytic cysteine residues in tyrosine kinase domains, resulting in increased kinase activity.[34,35,36] ROS can also alter cysteine residues on protein tyrosine phosphatases

(PTPs), leading to inactivation of PTPs and a net increase in phosphotyrosine signaling.[37,38] Targeted therapies often promote intracellular accumulation of ROS due to the disruption of redox homeostasis;[39,40] the resulting oxidative stress can be detrimental to cellular function and thereby contribute to the efficacy of therapy, but when maintained at sub-lethal levels ROS can serve as a second messenger to promote cellular adaptation in the face of external stressors by activating survival-promoting pathways. Within the inferred transcriptional module TM-J, which was significantly anticorrelated with the SFK-associated signaling module SM-K, we found significant overrepresentation of genes associated with NRF2 (NFE2L2), NRF1 (NFE2L1), and maintenance of oxidative stress, suggesting cells had undergone a reduced antioxidant response under VEM (Figure 3.9A). NRF2 is a TF that promotes cytoprotection from ROS by binding to antioxidant response elements (AREs) in the promoters of target genes including those encoding oxidoreductases and other detoxifying enzymes.[41] Direct examination of NRF2 transcript levels showed reduced expression under VEM and recovery with VEM removal, and nearly identical transcriptional kinetics of the NRF2 binding partner MAFG (Figure 3.9B). Additionally, VEM treatment prompted a concomitant gradual increase in expression of the E3 ubiquitin ligase β-TrCP (BTRC), which promotes NRF2 turnover,[42] and of MAF, a transcriptional repressor that targets AREs for suppression,[43] throughout the time course. These nearly-synchronized transcriptional events suggest VEM-treated cells undergo gradual dysregulation of redox homeostasis over the first three days of treatment.

We next subjected cells to direct measurement of intracellular ROS levels. In concordance with the observed transcriptional signature suggesting gradual oxidative stress, VEM-treated cells showed nearly 2.5-fold higher levels of ROS after 72 hours compared to control cells, and 1.5-fold higher levels compared to cells treated directly with 30 μM exogenous H_2O_2 (Figure 3.9C). ROS levels were restored to baseline or sub-baseline levels by one-hour treatment with N-acetylcysteine (NAC), an antioxidant prodrug and ROS scavenger. These results confirm that BRAF inhibition by VEM promotes significant yet sub-cytotoxic ROS accumulation.

To probe the relationship between VEM treatment, SFK signaling, and ROS accumulation, we treated cells with VEM, DAS, or the combination for 72 hours, with or without addition of NAC for one hour prior to harvesting, and subjected lysates to targeted MS, specifically aiming to quantify SFK phosphorylation and well-characterized SFK substrates (Figure 3.9D and Supplementary Table S4). We also quantified phosphorylated ERK1/2 to confirm successful VEM target engagement. The identity and quantitation of each phosphopeptide target was manually validated (Figures 3.10A and 3.10B). Targeted MS showed increased tyrosine phosphorylation on the SFK activation loop and on established SFK substrates under VEM treatment, which was reduced or fully prevented by addition of DAS (Figure 3.9E). Most substrates were downregulated by NAC treatment alone but to a lesser extent in combination with VEM, suggesting one hour of

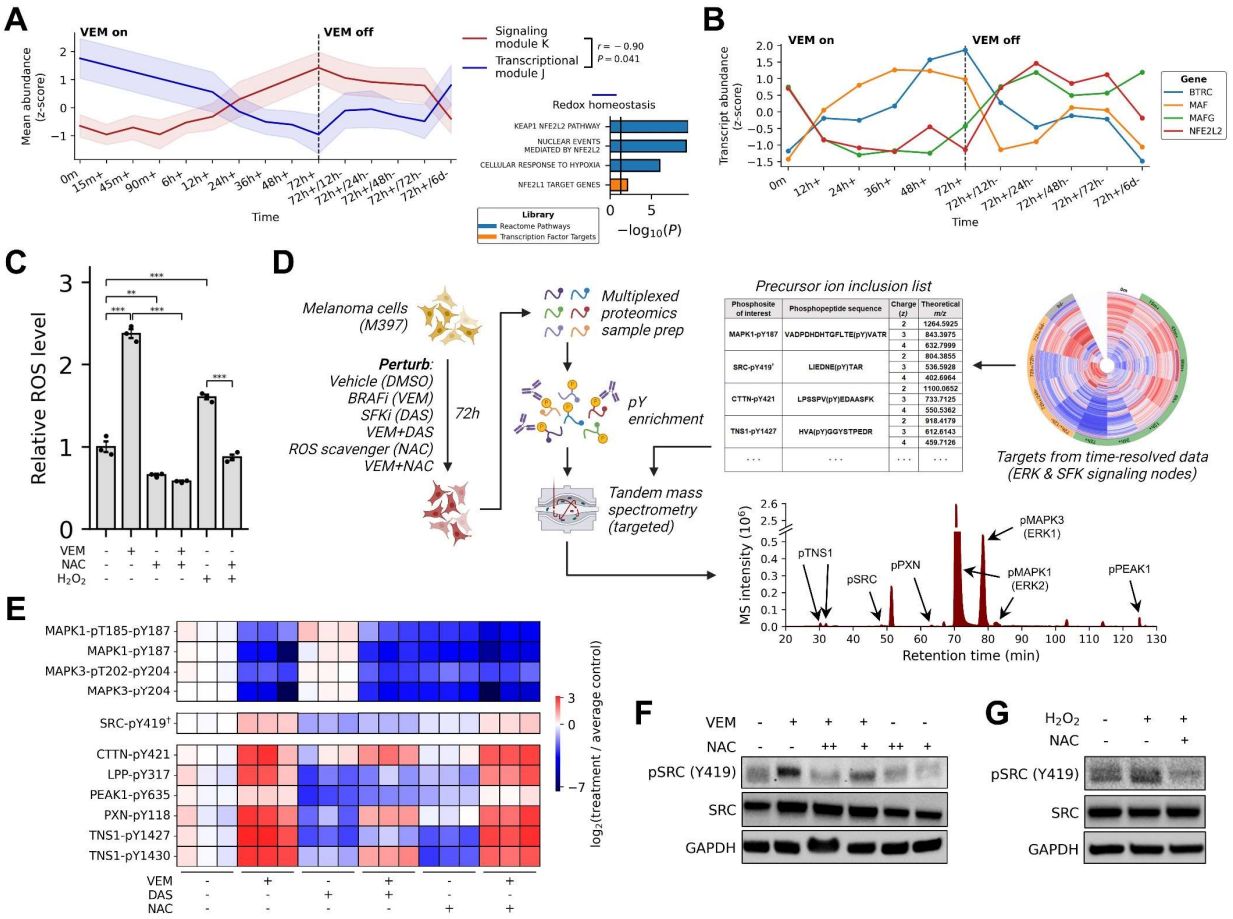

Figure 3.9. Reactive oxygen species (ROS) accumulation under BRAF inhibition promotes SFK signaling

A. Consensus dynamics of signaling module K (SM-K) and transcription module J (TM-J) (left); overrepresented gene sets in TM-J related to maintenance of oxidative stress (right). *P*-values were derived from two-sided Fisher's exact test with multiple hypothesis correction by the Benjamini-Hochberg procedure.

B. Transcriptional dynamics of antioxidant-promoting transcription factor NRF2 (NFE2L2) and related redox homeostasis genes.

C. Abundance of ROS in M397 cells treated with VEM (3 μM), antioxidant prodrug N-acetylcysteine (NAC) (10 mM), hydrogen peroxide (H_2O_2) (30 μM), and combinations thereof. All treatments were delivered for 72 hours except NAC, which was delivered one hour before measurement. Error bars depict standard error of the mean across three replicates. ** : $P < 0.01$; *** : $P < 0.005$ by two-sided *t*-test.

D. Workflow schematic for targeted mass spectrometry (MS) analysis of SFK signaling. The ion chromatogram depicts MS intensity of the phosphotyrosine immonium ion (fragments with $m/z = 216.04$, ±10 ppm).

E. Phosphosite abundances under VEM (3 μM), DAS (50 nM), NAC (10 mM), and combinations thereof, measured by targeted MS. All treatments were delivered for 72 hours except NAC, which was delivered one hour before cell lysis.

F. Immunoblot of phosphorylated SRC activation loop and total SRC under VEM (3 μM), NAC (5 mM, + and 10 mM, ++), and combinations thereof.

G. Immunoblot of phosphorylated SRC activation loop and total SRC under H_2O_2 (30 μM) alone and in combination with NAC (10 mM).

†The tryptic phosphopeptide supporting SRC-pY419 also maps to activation loops on three other paralogous SFKs (FYN-pY420, LCK-pY394, and YES1-pY426).

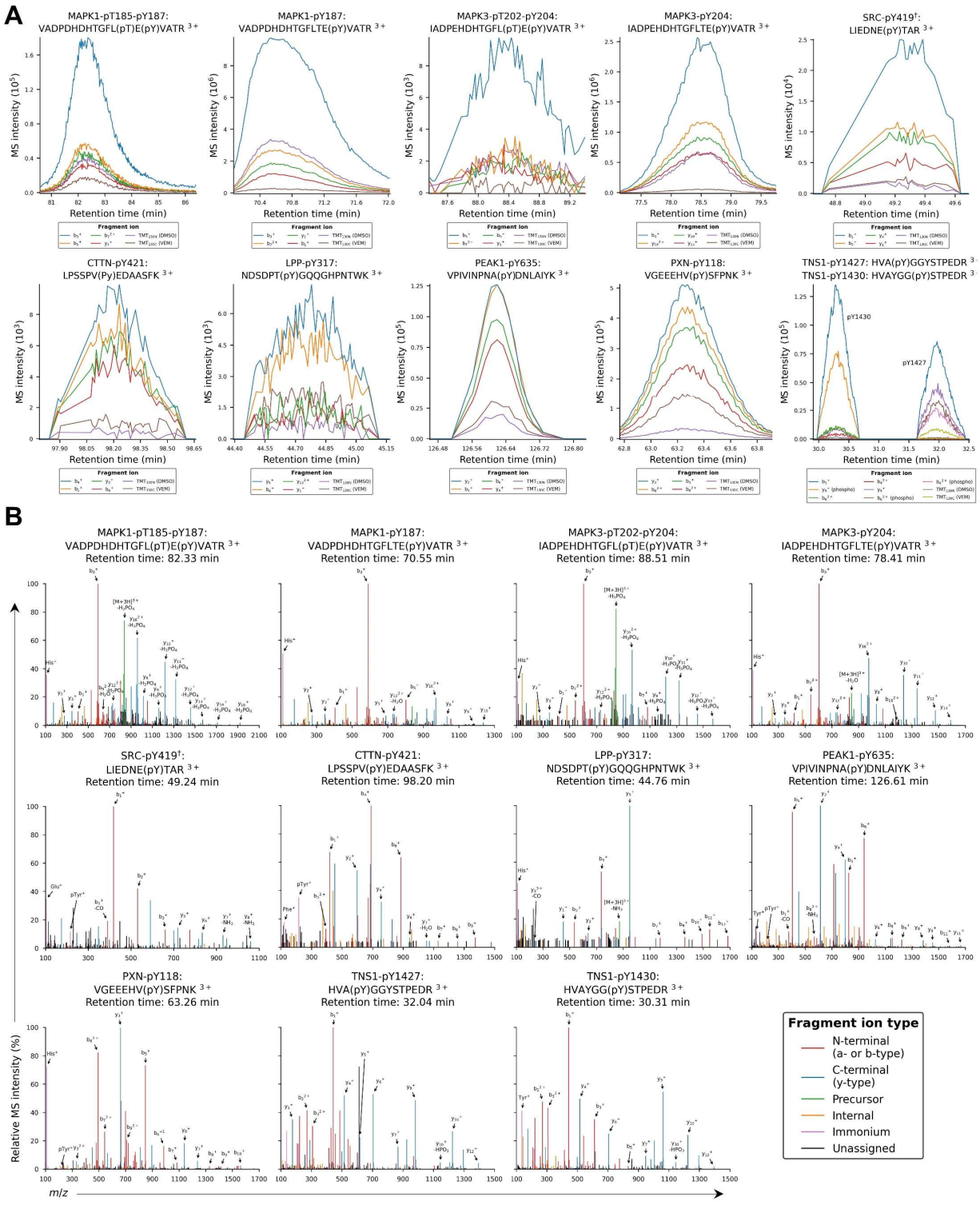

Figure 3.10. Manually validated targeted MS data, related to Figure 3.9

A. Fragment ion chromatograms of the phosphopeptides quantified in Figure 3.9E.

B. MS/MS spectra of the phosphopeptides quantified in Figure 3.9E, acquired at the elution apex where sensitivity is maximal. Tandem mass tag reporter ions used for quantitation are not shown.

†The tryptic phosphopeptide supporting SRC-pY419 also maps to activation loops on three other paralogous SFKs (FYN-pY420, LCK-pY394, and YES1-pY426).

NAC treatment may not be sufficient time for PTPs to return aberrant phosphorylation to baseline levels.

We confirmed significantly increased SRC phosphorylation under VEM by western blot, which was prevented by combination treatment with DAS and with NAC in a dose-dependent manner (Figure 3.9F). Compared to MS-based quantitation, western blot showed NAC treatment had a greater effect on SRC phosphorylation, potentially due to ambiguity introduced by the non-unique mapping of the tryptic SFK phosphopeptide (LIEDNE(pY)TAR maps to human SRC, FYN, LCK, and YES1). Finally, we observed that direct exposure of cells to exogenous H_2O_2 drove an increase in SRC phosphorylation that was prevented by NAC (Figure 3.9G). Together, these results establish a causal association between VEM treatment, intracellular ROS levels, and net SFK activity.

SFK-mediated adaptation to BRAF inhibition sensitizes cells to dasatinib

We sought to test whether early SFK induction by VEM would render cells susceptible to combination treatment with DAS. We observed pronounced and sustained cell growth inhibition under the drug combination across a panel of patient-derived *BRAF*^{V600E} melanoma cell lines, all of which eventually expanded under VEM alone (Figure 3.11A) and were unresponsive to DAS alone (Figure 3.11B). Two cell lines in particular, M233 and M381, were durably suppressed despite previous evidence of intrinsic resistance to VEM.[12] These findings suggest some degree of generality of the SFK-mediated response to BRAF inhibition and confirm that this response can confer a strong mitogenic and survival dependency.

We verified the efficacy of this combination in an orthotopic xenograft mouse model of the M397 line and observed significant tumor stasis with the drug combination compared to VEM and DAS monotherapy (Figure 3.11C and 6D). Notably, tumors were more responsive to DAS in vivo than the M397 line was in vitro; this is likely due to the higher dose of DAS delivered in vivo and also may indicate the presence of additional microenvironmental and physiological determinants of drug sensitivity that weren't captured in simpler in vitro models.[31] Taken together, our results support a time-resolved model where adaptation to BRAF inhibition leads to a gradual loss of redox homeostasis, accumulation of ROS, and resultant SFK activation, likely accompanied by PTP inhibition, and together leading to a pro-survival response that potently sensitizes cells to SFK inhibition (Figure 3.11E).

Discussion

The systems-level intracellular molecular response to oncoprotein inhibition can dictate whether an exposed tumor cell will survive or die. In pursuing improved targeted therapies and

therapy combinations for cancer, it has become crucial to map and better understand the complex and multifactorial systems that encode robustness to oncoprotein disruption. To elucidate the early temporal stages that precede and potentially lead to complete therapy resistance, we conducted a comprehensive analysis of the kinetic changes in cell signaling networks over minutes, hours, and days following the administration of vemurafenib (VEM), a $BRAF^{V600E}$ inhibitor, using a melanoma cell line with partial responsiveness to BRAF inhibition as a model system. Given the importance of tumor cell-intrinsic signaling mechanisms in mediating responses to kinase inhibitors – including feedback inhibition, pathway cross-talk, and kinase redundancy, among others – we reasoned that a hypothesis-free time-resolved characterization of signaling events that unfold early under drug treatment would provide deep insights into cellular adaptation to targeted therapy.

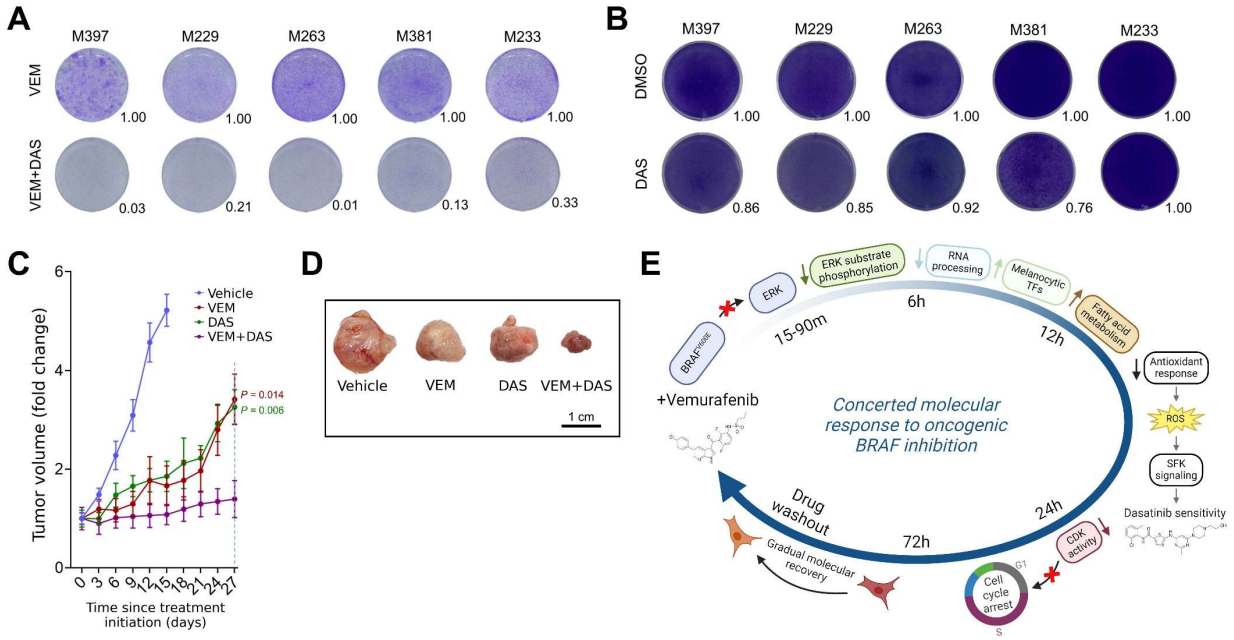

Figure 3.11. Adaptive response to BRAF inhibition confers sensitivity to SFK inhibitor dasatinib *in vitro* and *in vivo*

A. Clonogenic assays of a panel of patient-derived melanoma cell lines treated with VEM (3 μM) alone or in combination with DAS (50 nM).
B. Clonogenic assays of a panel of patient-derived melanoma cell lines treated with DMSO (0.1%) or DAS (50 nM).
C. Tumor growth curves of the M397-derived orthotopic xenograft mouse model treated with vehicle, VEM (100 mg/kg), DAS (30 mg/kg), or VEM combined with DAS. Error bars depict standard error of the mean across five replicates. P-values were calculated by two-sided Welch's *t*-test.
D. Resected tumors from cell line xenograft mouse models after 27 days of treatment with the indicated drugs.
E. Timeline schematic of the dynamics of SFK activity and other selected critical regulatory events driven by BRAF inhibition by VEM.

We observed multiple distinct stages of signaling network remodeling in the drug-altered phosphoproteome, corresponding to early, intermediate, and late pathway alterations. Treatment with VEM lead to rapid and sustained inhibition of the BRAF-ERK axis and gradual downregulation of RB1 phosphorylation. These observations indicate reduced mitotic activity and were consistent with corresponding dynamic measurements of cell viability. We observed distinct kinetics of phosphorylation loss on canonical ERK1/2 substrates in response to VEM treatment, including ERF, MAP2K2 (MEK2), and STMN1, suggesting that their phospho-regulation may be controlled by other kinases besides ERK1/2 or by distinct serine/threonine phosphatases.

The marked suppression of ERK1/2 activity during VEM treatment suggests that cell survival was not dependent on reactivation of BRAF or ERK1/2 during the measured time course. We speculate that the absence of ERK1/2 reactivation within our model system may be attributed to the efficient blockade of both mutant and wild-type BRAF by VEM at 3 μM, such that the RAF-ERK pathway is durably inhibited even in the presence of possible upstream RTK/RAS activation.

Through the kinetic profiling of mRNA transcript levels, we found strong agreement in cell state dynamics with the time-resolved phosphoproteome. Both classes of biomolecules demonstrated an early response to VEM and a near-complete reversal of remodeling following six days of VEM removal. These melanoma cells are known to exhibit significant molecular and phenotypic plasticity under BRAF inhibition;[12] our results confirm that maintenance of the early drug-adapted cell state depends on sustained BRAF inhibition.

Inference of kinetically-defined signaling and transcriptional modules recovered known associations while also revealing many examples of new signaling-gene regulatory associations. Although it is currently intractable to individually examine and experimentally test the relationships between all possible pairs of observed phosphosites and genes (>17M), we believe this time-resolved multimodal dataset serves as a valuable resource to investigate new lines of inquiry into the concerted molecular processes that follow oncoprotein inhibition and tumor cell stress within a well-characterized model system of adaptive drug response.

SFK induction during targeted therapy treatment has been described in multiple cancers, including melanoma;[30,31,32] our study sheds light on the kinetics associated with this response, revealing that signs of SFK induction can emerge as early as 3-6 hours of oncoprotein inhibition. This onset is markedly earlier than previously appreciated, suggesting a more immediate cellular adaptation to targeted therapy via this axis than previously appreciated. Intriguingly, similar to the distinct phosphorylation patterns of different canonical ERK1/2 substrates, our analysis revealed distinct patterns of phosphorylation on canonical SFK substrates – for instance, after 72 hours PXN-pY118 was upregulated 1.8-fold, CTTN-pY421 was upregulated 4.1-fold, and TNS1-pY1427 was upregulated over 5.2-fold on average compared to control cells. This variation in signaling magnitude may suggest the engagement of distinct sets of tyrosine phosphatases and

kinases, including but not limited to SFKs, in modulating the phosphorylation states of these crucial substrates.

We observed a substantial increase in intracellular ROS levels following oncogenic BRAF inhibition. By perturbing cells with ROS with or without NAC as a competitive antioxidant, we were able to isolate the effect of ROS on SFK activity and found that increased ROS level leads to increased SFK activation loop phosphorylation. In addition to their established role in directly activating SFKs by oxidizing catalytic cysteine residues,[34,35,36] ROS are known to modulate signaling networks by inhibiting the action of PTPs, similarly by oxidizing the free thiol groups on catalytically essential cysteines.[37,38,44] While our study did not directly identify PTP oxidation as an explanatory mechanism for the net increase in tyrosine phosphorylation under VEM, it is likely that PTP inhibition contributed to this observation. We note that while acute treatment of NAC was sufficient to reduce SFK phosphorylation after VEM exposure, this effect did not extend to many canonical SFK substrates when we profiled by targeted mass spectrometry (MS), perhaps indicating that one hour of NAC exposure is not enough time to fully recover the catalytic activity of PTPs.

Our observations reveal a strong degree of synergy between VEM and the SFK inhibitor dasatinib (DAS) in vitro, and we observed tumor stasis with the combination in vivo despite inability of either monotherapy to control tumor burden. The therapeutic potential of DAS as a monotherapy for melanoma has been explored in multiple clinical trials, which have generally failed to demonstrate a clinically meaningful response within a tolerable dose range.[45,46] DAS is currently approved only for the treatment of chronic myeloid leukemia and a subset of other Philadelphia chromosome-positive leukemias due to its potent activity against BCR-ABL1. Consistent with the expectation of low sensitivity to SFK inhibition alone, we observed little to no effect of DAS across a panel of five patient-derived melanoma cell lines. However, the potent and sustained inhibition of cell growth when combined with VEM suggests that induction of SFK signaling by VEM reveals an underlying synthetic lethal interaction between mutant BRAF and the SRC family, which may be exploited therapeutically. Additional preclinical studies would be needed to verify the generality of this drug combination's efficacy and to identify potential biomarkers identifying the subset of patients most likely to benefit from low-dose SFK inhibition combined with BRAF/MEK blockade.

This study underscores the significant potential of quantitatively characterizing the dynamics of early alterations in cell signaling and transcriptional networks under targeted therapy treatment. Such analysis provides powerful insights into multiple aspects of cell state: the dynamics of drug-target engagement, the downstream molecular processes regulated by the target, and the induction of compensatory pro-survival signaling pathways that should be considered for co-targeting.

References

1. O'Reilly K.E., Rojo F., She Q.B., Solit D., Mills G.B., Smith D., Lane H., Hofmann F., Hicklin D.J., Ludwig D.L., et al. (2006). mTOR inhibition induces upstream receptor tyrosine kinase signaling and activates Akt. Cancer Res *66*, 1500-8.
2. Shaffer S.M., Dunagin M.C., Torborg S.R., Torre E.A., Emert B., Krepler C., Beqiri M., Sproesser K., Brafford P.A., Xiao M., et al. (2017). Rare cell variability and drug-induced reprogramming as a mode of cancer drug resistance. Nature *546*, 431-435.
3. Yang C., Tian C., Hoffman T.E., Jacobsen N.K., Spencer S.L. (2021). Melanoma subpopulations that rapidly escape MAPK pathway inhibition incur DNA damage and rely on stress signalling. Nat Commun *12*, 1747.
4. Hoffman T.E., Nangia V., Ill C.R., Passanisi V.J., Armstrong C., Yang C., Spencer S.L. (2023). Multiple cancers escape from multiple MAPK pathway inhibitors and use DNA replication stress signaling to tolerate aberrant cell cycles. Sci Signal *16*, eade8744.
5. Ercan D., Xu C., Yanagita M., Monast C.S., Pratilas C.A., Montero J., Butaney M., Shimamura T., Sholl L., Ivanova E.V., et al. (2012). Reactivation of ERK signaling causes resistance to EGFR kinase inhibitors. Cancer Discov *2*, 934-47.
6. Corcoran R.B., André T., Atreya C.E., Schellens J.H.M., Yoshino T., Bendell J.C., Hollebecque A., McRee A.J., Siena S., Middleton G., et al. (2018). Combined BRAF, EGFR, and MEK Inhibition in Patients with $BRAF^{V600E}$-Mutant Colorectal Cancer. Cancer Discov *8*, 428-443.
7. Noronha A., Belugali Nataraj N., Lee J.S., Zhitomirsky B., Oren Y., Oster S., Lindzen M., Mukherjee S., Will R., Ghosh S., et al. (2022). AXL and Error-Prone DNA Replication Confer Drug Resistance and Offer Strategies to Treat EGFR-Mutant Lung Cancer. Cancer Discov *12*, 2666-2683.
8. Isozaki H., Sakhtemani R., Abbasi A., Nikpour N., Stanzione M., Oh S., Langenbucher A., Monroe S., Su W., Cabanos H.F., et al. (2023). Therapy-induced APOBEC3A drives evolution of persistent cancer cells. Nature *620*, 393-401.
9. Labrie M., Brugge J.S., Mills G.B., Zervantonakis I.K. (2022). Therapy resistance: opportunities created by adaptive responses to targeted therapies in cancer. Nat Rev Cancer *22*, 323-339.
10. Zhang Y., Wolf-Yadlin A., Ross P.L., Pappin D.J., Rush J., Lauffenburger D.A., White F.M. (2005). Time-resolved mass spectrometry of tyrosine phosphorylation sites in the epidermal growth factor receptor signaling network reveals dynamic modules. Mol Cell Proteomics *4*, 1240-50.
11. Reddy R.J., Gajadhar A.S., Swenson E.J., Rothenberg D.A., Curran T.G., White F.M. (2016). Early signaling dynamics of the epidermal growth factor receptor. Proc Natl Acad Sci U S A *113*, 3114-9.
12. Su Y., Wei W., Robert L., Xue M., Tsoi J., Garcia-Diaz A., Homet Moreno B., Kim J., Ng R.H., Lee J.W., et al. (2017). Single-cell analysis resolves the cell state transition and signaling dynamics associated with melanoma drug-induced resistance. Proc Natl Acad Sci U S A *114*, 13679-13684.
13. Su Y., Bintz M., Yang Y., Robert L., Ng A.H.C., Liu V., Ribas A., Heath J.R., Wei W. (2019). Phenotypic heterogeneity and evolution of melanoma cells associated with targeted therapy resistance. PLoS Comput Biol *15*, e1007034.
14. Su Y., Ko M.E., Cheng H., Zhu R., Xue M., Wang J., Lee J.W., Frankiw L., Xu A., Wong S., et al. (2020). Multi-omic single-cell snapshots reveal multiple independent trajectories to drug tolerance in a melanoma cell line. Nat Commun *11*, 2345.

15. Du J., Su Y., Qian C., Yuan D., Miao K., Lee D., Ng A.H.C., Wijker R.S., Ribas A., Levine R.D., et al. (2020). Raman-guided subcellular pharmaco-metabolomics for metastatic melanoma cells. Nat Commun *11*, 4830.
16. Su Y., Lu X., Li G., Liu C., Kong Y., Lee J.W., Ng R., Wong S., Robert L., Warden C., et al. (2019). Kinetic Inference Resolves Epigenetic Mechanism of Drug Resistance in Melanoma. Preprint at bioRxiv, 724740.
17. Bollag G., Hirth P., Tsai J., Zhang J., Ibrahim P.N., Cho H., Spevak W., Zhang C., Zhang Y., Habets G., et al. (2010). Clinical efficacy of a RAF inhibitor needs broad target blockade in BRAF-mutant melanoma. Nature *467*, 596-9.
18. Poulikakos P.I., Zhang C., Bollag G., Shokat K.M., Rosen N. (2010). RAF inhibitors transactivate RAF dimers and ERK signalling in cells with wild-type BRAF. Nature *464*, 427-30.
19. Gerosa L., Chidley C., Fröhlich F., Sanchez G., Lim S.K., Muhlich J., Chen J.Y., Vallabhaneni S., Baker G.J., Schapiro D., et al. (2020). Receptor-Driven ERK Pulses Reconfigure MAPK Signaling and Enable Persistence of Drug-Adapted BRAF-Mutant Melanoma Cells. Cell Syst *11*, 478-494.e9.
20. Harbour J.W., Luo R.X., Dei Santi A., Postigo A.A., Dean D.C. (1999). Cdk phosphorylation triggers sequential intramolecular interactions that progressively block Rb functions as cells move through G1. Cell *98*, 859-69.
21. Frederick D.T., Piris A., Cogdill A.P., Cooper Z.A., Lezcano C., Ferrone C.R., Mitra D., Boni A., Newton L.P., Liu C., et al. (2013). BRAF inhibition is associated with enhanced melanoma antigen expression and a more favorable tumor microenvironment in patients with metastatic melanoma. Clin Cancer Res *19*, 1225-31.
22. Ramsdale R., Jorissen R.N., Li F.Z., Al-Obaidi S., Ward T., Sheppard K.E., Bukczynska P.E., Young R.J., Boyle S.E., Shackleton M., et al. (2015). The transcription cofactor c-JUN mediates phenotype switching and BRAF inhibitor resistance in melanoma. Sci Signal *8*, ra82.
23. Hugo W., Shi H., Sun L., Piva M., Song C., Kong X., Moriceau G., Hong A., Dahlman K.B., Johnson D.B., et al. (2015). Non-genomic and Immune Evolution of Melanoma Acquiring MAPKi Resistance. Cell *162*, 1271-85.
24. Potterf S.B., Furumura M., Dunn K.J., Arnheiter H., Pavan W.J. (2000). Transcription factor hierarchy in Waardenburg syndrome: regulation of MITF expression by SOX10 and PAX3. Hum Genet *107*, 1-6.
25. Ennen M., Keime C., Gambi G., Kieny A., Coassolo S., Thibault-Carpentier C., Margerin-Schaller F., Davidson G., Vagne C., Lipsker D., et al. (2017). MITF-High and MITF-Low Cells and a Novel Subpopulation Expressing Genes of Both Cell States Contribute to Intra- and Intertumoral Heterogeneity of Primary Melanoma. Clin Cancer Res *23*, 7097-7107.
26. Tripathi R., Liu Z., Jain A., Lyon A., Meeks C., Richards D., Liu J., He D., Wang C., Nespi M., et al. (2020). Combating acquired resistance to MAPK inhibitors in melanoma by targeting Abl1/2-mediated reactivation of MEK/ERK/MYC signaling. Nat Commun *11*, 5463.
27. Barger P.M., Brandt J.M., Leone T.C., Weinheimer C.J., Kelly D.P. (2000). Deactivation of peroxisome proliferator-activated receptor-alpha during cardiac hypertrophic growth. J Clin Invest *105*, 1723-30.
28. Mooli R.G.R., Rodriguez J., Takahashi S., Solanki S., Gonzalez F.J., Ramakrishnan S.K., Shah Y.M. (2021). Hypoxia via ERK Signaling Inhibits Hepatic PPARα to Promote Fatty Liver. Cell Mol Gastroenterol Hepatol *12*, 585-597.

29. Needham E.J., Parker B.L., Burykin T., James D.E., Humphrey S.J. (2019). Illuminating the dark phosphoproteome. Sci Signal *12*, e12/565/eaau8645.
30. Girotti M.R., Pedersen M., Sanchez-Laorden B., Viros A., Turajlic S., Niculescu-Duvaz D., Zambon A., Sinclair J., Hayes A., Gore M., et al. (2013). Inhibiting EGF receptor or SRC family kinase signaling overcomes BRAF inhibitor resistance in melanoma. Cancer Discov *3*, 158-67.
31. Hirata E., Girotti M.R., Viros A., Hooper S., Spencer-Dene B., Matsuda M., Larkin J., Marais R., Sahai E. (2015). Intravital imaging reveals how BRAF inhibition generates drug-tolerant microenvironments with high integrin β1/FAK signaling. Cancer Cell *27*, 574-88.
32. Zhu E.Y., Riordan J.D., Vanneste M., Henry M.D., Stipp C.S., Dupuy A.J. (2022). SRC-RAC1 signaling drives drug resistance to BRAF inhibition in de-differentiated cutaneous melanomas. NPJ Precis Oncol *6*, 74.
33. Fallahi-Sichani M., Becker V., Izar B., Baker G.J., Lin J.R., Boswell S.A., Shah P., Rotem A., Garraway L.A., Sorger P.K. (2017). Adaptive resistance of melanoma cells to RAF inhibition via reversible induction of a slowly dividing de-differentiated state. Mol Syst Biol *13*, 905.
34. Giannoni E., Buricchi F., Raugei G., Ramponi G., Chiarugi P. (2005). Intracellular reactive oxygen species activate Src tyrosine kinase during cell adhesion and anchorage-dependent cell growth. Mol Cell Biol *25*, 6391-403.
35. Chan H.L., Chou H.C., Duran M., Gruenewald J., Waterfield M.D., Ridley A., Timms J.F. (2010). Major role of epidermal growth factor receptor and Src kinases in promoting oxidative stress-dependent loss of adhesion and apoptosis in epithelial cells. J Biol Chem *285*, 4307-18.
36. Heppner D.E., Dustin C.M., Liao C., Hristova M., Veith C., Little A.C., Ahlers B.A., White S.L., Deng B., Lam Y.W., et al. (2018). Direct cysteine sulfenylation drives activation of the Src kinase. Nat Commun *9*, 4522.
37. Groen A., Lemeer S., van der Wijk T., Overvoorde J., Heck A.J., Ostman A., Barford D., Slijper M., den Hertog J. (2005). Differential oxidation of protein-tyrosine phosphatases. J Biol Chem *280*, 10298-304.
38. Denu J.M., Tanner K.G. (1998). Specific and reversible inactivation of protein tyrosine phosphatases by hydrogen peroxide: evidence for a sulfenic acid intermediate and implications for redox regulation. Biochemistry *37*, 5633-42.
39. Cesi G., Walbrecq G., Zimmer A., Kreis S., Haan C. (2017). ROS production induced by BRAF inhibitor treatment rewires metabolic processes affecting cell growth of melanoma cells. Mol Cancer *16*, 102.
40. Teppo H.R., Soini Y., Karihtala P. (2017). Reactive Oxygen Species-Mediated Mechanisms of Action of Targeted Cancer Therapy. Oxid Med Cell Longev *2017*, 1485283.
41. Ma Q. (2013). Role of nrf2 in oxidative stress and toxicity. Annu Rev Pharmacol Toxicol *53*, 401-26.
42. Hayes J.D., Chowdhry S., Dinkova-Kostova A.T., Sutherland C. (2015). Dual regulation of transcription factor Nrf2 by Keap1 and by the combined actions of β-TrCP and GSK-3. Biochem Soc Trans *43*, 611-20.
43. Dhakshinamoorthy S., Jaiswal A.K. (2002). c-Maf negatively regulates ARE-mediated detoxifying enzyme genes expression and anti-oxidant induction. Oncogene *21*, 5301-12.
44. Weibrecht I., Böhmer S.A., Dagnell M., Kappert K., Ostman A., Böhmer F.D. (2007). Oxidation sensitivity of the catalytic cysteine of the protein-tyrosine phosphatases SHP-1 and SHP-2. Free Radic Biol Med *43*, 100-10.
45. Kluger H.M., Dudek A.Z., McCann C., Ritacco J., Southard N., Jilaveanu L.B., Molinaro A., Sznol M. (2011). A phase 2 trial of dasatinib in advanced melanoma. Cancer *117*, 2202-8.

46. Kalinsky K., Lee S., Rubin K.M., Lawrence D.P., Iafrarte A.J., Borger D.R., Margolin K.A., Leitao M.M., Tarhini A.A., Koon H.B., et al. (2017). A phase 2 trial of dasatinib in patients with locally advanced or stage IV mucosal, acral, or vulvovaginal melanoma: A trial of the ECOG-ACRIN Cancer Research Group (E2607). Cancer *123*, 2688-2697.

Chapter 4:
Conclusions

"The 325,000 patients with cancer who are going to die this year cannot wait; nor is it necessary, in order to make great progress in the cure of cancer, for us to have the full solution of all the problems of basic research… the history of Medicine is replete with examples of cures obtained years, decades, and even centuries before the mechanism of action was understood for these cures."

Sidney Farber, M.D., 1971

This thesis describes two efforts to further our understanding of the signaling basis for poor tumor cell sensitivity to oncogenic kinase inhibition, a key therapeutic modality in the management of cancer. In Chapter 1, I outlined some of the known fundamental biology and methodologies underlying this work. In Chapter 2, I reported a set of model-specific and consensus signals promoting tolerance to tyrosine kinase inhibitors (TKIs) in cell line models of non-small cell lung cancer. In Chapter 3, I detailed a collaborative effort to profile the signaling and transcriptional dynamics associated with drug-induced tumor cell adaptation to oncogenic BRAF inhibition. The work outlined in this thesis relied on careful selection of model systems which, though not without limitations, were shown to recapitulate clinically relevant phenomena. In addition, many of the discoveries reported here were enabled by mass spectrometry (MS)-based phosphoproteomics, a powerful analytical approach that allows for direct measurement of subcellular kinase signaling networks at proteome-scale. In this concluding chapter, I will outline some of the present challenges and opportunities researchers and clinicians face in the development, application, and evaluation of molecular targeted therapy in oncology. In particular, I will call attention to key challenges related to attaining durable responses to targeted therapy, and to the opportunities for systems-level molecular profiling and the rational use of combination therapy in cancer treatment.

To achieve durable responses to targeted therapy, proper drug target selection is critical. In nearly all clinical cases today in which targeted therapy may be appropriate, drug targets are selected either by tumor tissue histology, such as with hormone therapy or HER2-directed therapy in breast cancer, or by tumor genotyping, which is performed most commonly in the treatment of particular malignancies of the lung, skin, and blood, among others.[1] In the two to three decades since the first genotype-directed targeted therapies were approved, it is now clear that new approaches are needed to uncover actionable drug targets. Systems-level or "omics" technologies, including MS-based proteomics and phosphoproteomics, RNA sequencing, metabolomics, and epigenomic profiling, offer the promise of measuring as many potentially relevant molecules and pathways within tumor tissue as possible to identify possible points for therapeutic intervention. These approaches are agnostic to prior knowledge of the relevant tumor biology, allowing for a direct readout of biochemical pathway activity and thereby circumventing the need to infer oncogenic drivers solely from tumor genome sequence. In addition, systems-level approaches are revealing new molecular subtypes that describe tumor tissue in terms of the abundances of relevant biomolecules present, rather than of the histology or oncogenic mutations harbored;[2,3,4] these new subtyping efforts, in addition to patient-specific profiling using many of the same technologies,[5,6] may prove to hold high value for drug target selection in the oncology clinic.

As discussed earlier in this thesis, achieving a strong initial response to therapy is highly dependent on effective blockade of oncogenic pathways and signaling. Biochemical complexity endows our cells with considerable robustness to stress and the capability to adapt to new circumstances; unfortunately, this very capability often thwarts our best attempts to durably arrest or kill cancer cells. As a result, many patients may need more than one targeted therapy to effectively block multiple oncogenic pathways or to target distinct subclones of cancer cells within a tumor. This challenge has motivated the use of rational combination therapy, and there is much enthusiasm among cancer researchers in developing methods and models to find effective solutions among the combinatorially vast space of candidates. Combining targeted therapies with other modalities, such as immunotherapy, cytotoxic chemotherapy, or radiotherapy, also holds great promise.[7,8,9,10,11,12,13] Predicting which patients are most likely to benefit from any particular combination therapy is a significant challenge, but one where systems-level approaches, once again, will likely play an outsized role by stratifying patient populations or determining optimal patient-specific combinations and regimens.

Tumors are ecosystems composed of diverse populations of neoplastic and non-neoplastic cells, and as such are subject to the laws of evolution by natural selection. Indeed, evolutionary pressures are recognized to play an important role in sculpting the biology of cancer starting with the earliest (epi)genetic alteration in the cell of origin.[14,15] Anti-cancer therapy acts as a negative selective pressure, under which surviving tumor cells will continue to evolve toward the fittest

state attainable in a process called acquired resistance, often resulting in complete loss of drug sensitivity and aggressive disease. Rational combination therapy can play an important role in delaying or preventing acquired resistance; by ensuring more complete blockade of oncogenic signaling, or by targeting distinct subclones within a tumor harboring distinct dependencies, carefully selected drug combinations may leave fewer residual tumor cells behind, minimizing the size of the reservoir from which acquired resistance spills. Additionally, we now know that some targeted therapies inadvertently accelerate this evolutionary process by inducing hypermutagenic pathways that increase the probability of the emergence of resistance-driving mutations, thereby promoting the evolvability of tumors. A more complete understanding of these drug-induced molecular responses, and how they might be antagonized, may pay dividends in our ability to durably suppress tumors and maximize patient survival time.

When two drugs are paired together and show greater effect than expected given their individual effects, the drugs are said to be *synergistic*. Finding synergistic pairs of agents has been a priority in experimental cancer research for decades; however, there is debate among researchers and clinicians about whether drug synergy is a useful measure of success of any given combination therapy in the clinic. Recent retrospective analyses of clinical outcomes data has revealed that most of today's effective combination therapies in the oncology clinic are additive or even sub-additive, and derive their efficacy from independent mechanisms of action and non-overlapping toxicity profiles, or by covering a wider spectrum of possible oncogenic drivers and thereby increasing the likelihood of achieving an effect.[16,17,18] Given these findings, it is crucial to interpret drug synergy results with care. In Chapter 2 of this thesis, synergy assays are used on lung cancer cell lines, which reveal that SRC family kinase (SFK) inhibition is synergistic with oncogenic tyrosine kinase inhibition across several drug-tolerant model systems; these results are corroborated by clonogenic assays which test for the durability of these combination effects. Performing orthogonal pairs of assays, I argue, is essential in nominating effective drug combinations from work done in experimental model systems. In the effort to find optimal combination therapies for cancer treatment, our field should achieve consensus on the precise role, if any, drug synergy will play.

There is much cause to be optimistic about the future of targeted cancer therapy. New technologies are enabling new biological insight, and new therapeutic modalities are opening the doors to a more complete toolbox for the clinical management of malignancy. This thesis contributes new links between tumor cell-intrinsic signaling and sensitivity to targeted therapy, emphasizing the importance of this particular aspect of cancer biology and hopefully bringing us one step closer to durable and effective strategies for cancer treatment.

References

1. Chakravarty D., Solit D.B. (2021). Clinical cancer genomic profiling. Nat Rev Genet *22*, 483-501.
2. Zhang H., Liu T., Zhang Z., Payne S.H., Zhang B., McDermott J.E., Zhou J.Y., Petyuk V.A., Chen L., Ray D., et al. (2016). Integrated Proteogenomic Characterization of Human High-Grade Serous Ovarian Cancer. Cell *166*, 755-765.
3. Vasaikar S., Huang C., Wang X., Petyuk V.A., Savage S.R., Wen B., Dou Y., Zhang Y., Shi Z., Arshad O.A., et al. (2019). Proteogenomic Analysis of Human Colon Cancer Reveals New Therapeutic Opportunities. Cell *177*, 1035-1049.e19.
4. Krug K., Jaehnig E.J., Satpathy S., Blumenberg L., Karpova A., Anurag M., Miles G., Mertins P., Geffen Y., Tang L.C., et al. (2020). Proteogenomic Landscape of Breast Cancer Tumorigenesis and Targeted Therapy. Cell *183*, 1436-1456.e31.
5. Stopfer L.E., Flower C.T., Gajadhar A.S., Patel B., Gallien S., Lopez-Ferrer D., White F.M. (2021). High-Density, Targeted Monitoring of Tyrosine Phosphorylation Reveals Activated Signaling Networks in Human Tumors. Cancer Res *81*, 2495-2509.
6. Alkhatib H., Conage-Pough J., Roy Chowdhury S., Shian D., Zaid D., Rubinstein A.M., Sonnenblick A., Peretz-Yablonsky T., Granit A., Carmon E., et al. (2024). Patient-specific signaling signatures predict optimal therapeutic combinations for triple negative breast cancer. Mol Cancer *23*, 17.
7. Tian J., Chen J.H., Chao S.X., Pelka K., Giannakis M., Hess J., Burke K., Jorgji V., Sindurakar P., Braverman J., et al. (2023). Combined PD-1, BRAF and MEK inhibition in $BRAF^{V600E}$ colorectal cancer: a phase 2 trial. Nat Med *29*, 458-466.
8. Hattori T., Maso L., Araki K.Y., Koide A., Hayman J., Akkapeddi P., Bang I., Neel B.G., Koide S. (2023). Creating MHC-Restricted Neoantigens with Covalent Inhibitors That Can Be Targeted by Immune Therapy. Cancer Discov *13*, 132-145.
9. Zhang Z., Rohweder P.J., Ongpipattanakul C., Basu K., Bohn M.F., Dugan E.J., Steri V., Hann B., Shokat K.M., Craik C.S. (2022). A covalent inhibitor of K-Ras(G12C) induces MHC class I presentation of haptenated peptide neoepitopes targetable by immunotherapy. Cancer Cell *40*, 1060-1069.e7.
10. Tang K.H., Li S., Khodadadi-Jamayran A., Jen J., Han H., Guidry K., Chen T., Hao Y., Fedele C., Zebala J.A., et al. (2022). Combined Inhibition of SHP2 and CXCR1/2 Promotes Antitumor T-cell Response in NSCLC. Cancer Discov *12*, 47-61.
11. Stopfer L.E., Rettko N.J., Leddy O., Mesfin J.M., Brown E., Winski S., Bryson B., Wells J.A., White F.M. (2022). MEK inhibition enhances presentation of targetable MHC-I tumor antigens in mutant melanomas. Proc Natl Acad Sci U S A *119*, e2208900119.
12. Ahn R., Ursini-Siegel J. (2021). Clinical Potential of Kinase Inhibitors in Combination with Immune Checkpoint Inhibitors for the Treatment of Solid Tumors. Int J Mol Sci *22*, eijms22052608.
13. Lee M.J., Ye A.S., Gardino A.K., Heijink A.M., Sorger P.K., MacBeath G., Yaffe M.B. (2012). Sequential application of anticancer drugs enhances cell death by rewiring apoptotic signaling networks. Cell *149*, 780-94.
14. Merlo L.M., Pepper J.W., Reid B.J., Maley C.C. (2006). Cancer as an evolutionary and ecological process. Nat Rev Cancer *6*, 924-35.
15. Michor F., Iwasa Y., Nowak M.A. (2004). Dynamics of cancer progression. Nat Rev Cancer *4*, 197-205.

16. Palmer A.C., Sorger P.K. (2017). Combination Cancer Therapy Can Confer Benefit via Patient-to-Patient Variability without Drug Additivity or Synergy. Cell *171*, 1678-1691.e13.
17. Palmer A.C., Izar B., Hwangbo H., Sorger P.K. (2022). Predictable Clinical Benefits without Evidence of Synergy in Trials of Combination Therapies with Immune-Checkpoint Inhibitors. Clin Cancer Res *28*, 368-377.
18. Hwangbo H., Patterson S.C., Dai A., Plana D., Palmer A.C. (2023). Additivity predicts the efficacy of most approved combination therapies for advanced cancer. Nat Cancer *4*, 1693-1704.

Appendix A:
Methods for chapter 2

Cell lines and drug treatment

H1993, H2228, H1975, and HCC4006 cell lines were purchased from ATCC. EBC-1 cells were purchased from JCRB Cell Bank. H3122 cells were provided by the Pasi Jänne lab (DFCI). Cell lines were selected on the basis of their *MET*, *ALK*, and *EGFR* mutation status according to the Cancer Dependency Map.[1] All cell lines were cultured in RPMI-1640 supplemented with 10% FBS and were regularly tested for mycoplasma contamination. All drugs used in this study were purchased from Selleck Chemicals and were dissolved in dimethyl sulfoxide (DMSO). All experiments involving drug treatment were controlled for 0.1% DMSO exposure, and control cells were treated with 0.1% DMSO.

Cell viability dose-response assay

Cells were seeded in a 384-well plate (500 cells/well, 3 drugs/plate, n = 6 replicates per drug dose and n = 18 replicates for control cells) and incubated for 24 hours, followed by treatment with drug at the designated doses for 72 hours. Cell viability was quantified using CellTiter-Glo (Promega, catalog # G7572) according to the manufacturer protocol. All luminescence values were normalized to the average of the drug-free control wells. Outlier values were removed according to the 1.5×IQR rule. Monophasic or biphasic dose-response curves were fitted to the data according to the following viability equations:

$$V_{mono}(d) = (1-\gamma)\left(\frac{1}{1+\left(\frac{d}{EC_{50}}\right)^{\mathrm{n}}}\right)+\gamma$$

$$V_{bi}(d) = (1-\alpha)\left(\frac{1}{1+\left(\frac{d}{EC_{50,1}}\right)^{n_1}}\right)+\alpha\left(\frac{1}{1+\left(\frac{d}{EC_{50,2}}\right)^{n_2}}\right)$$

where $V(d) \in [0,1]$ is the fraction of viable cells under dose d (in nM). Under the monophasic model, EC_{50} provides an estimate of the dose at which there is a half-maximal effect, γ provides an estimate of the minimum viability, and n is a measure of the steepness of the response. Under the biphasic model, $EC_{50,1}$ and $EC_{50,2}$ are estimates of the doses at which there is a half-maximal effect for the first and second dose-response phases, respectively. α provides an estimate of the

intermediate viability of cells treated with doses between $EC_{50,1}$ and $EC_{50,2}$. n_1 and n_2 are measures of the steepness of the first and second dose-response phases, respectively. Model fitting was performed using the curve_fit function in the SciPy scientific computing python package.[2]

Clonogenic assays

Cells were seeded in 24-well plates (20,000 cells/well) and incubated for 24 hours prior to drug treatment. Drugged media was replenished every three days until drug washout, at which point all drugged media was removed and the cells were rinsed and replenished with drug-free media. From this point on, drug-free media was replenished every three days. At each indicated timepoint, plates were removed from culture and media was removed. Cells were fixed with 50% methanol in double-distilled water for 10 minutes and stained with 0.5% crystal violet in 25% methanol for 30 minutes.

Checkerboard assays

Cells were seeded in a 384-well plate (500 cells/well, n = 6 replicates per dose) and incubated for 24 hours prior, followed by treatment with drug pairs at the designated doses for 72 hours. Cell viability was quantified using CellTiter-Glo (Promega, catalog # G7572) according to the manufacturer protocol. All luminescence values were normalized to the average of the drug-free control wells. Outlier values were removed according to the 1.5×IQR rule.

For assessing drug synergy and antagonism, the Bliss independence model was used, which assumes that independent drug-drug interactions are multiplicative.[3] The model is summarized as follows: if exposure of cells to drug A at dose d_A results in effect $e_A \in [0,1]$, and exposure to drug B at dose d_B results in effect e_B, then the expected effect of combining A and B (at doses d_A and d_B, respectively) if A and B are independent is given by

$$\begin{aligned} \widehat{e_{AB}} &= 1 - (1 - e_A)(1 - e_B) \\ &= e_A + e_B - e_A e_B \end{aligned}$$

If the observed effect e_{AB} of combining A and B (at doses d_A and d_B, respectively) is greater than the expected effect, A and B are classified as synergistic; alternatively, if the observed effect is less than the expected effect, A and B are classified as antagonistic. The degree of synergy or antagonism is given by the Bliss score:

$$\begin{aligned} s_{AB} &= e_{AB} - \widehat{e_{AB}} \\ &= e_{AB} + e_A e_B - (e_A + e_B) \end{aligned}$$

In experiments where relative cell viability at a fixed endpoint is measured, drug effect e at a fixed dose is related to viability $v \in [0,1]$ as $e = 1 - v$. The Bliss score then simplifies to

$$s_{AB} = v_A v_B - v_{AB}$$

For each drug pair, Bliss scores were calculated and reported for each of 47 total combinations of doses (7×7 grid).

Phosphoproteomics sample preparation

Cells were lysed in 8M urea and total protein was quantified by bicinchoninic acid assay (Pierce, catalog # 23225). For each sample, 1 mg of protein was subjected to reduction in 10 mM dithiothreitol at 56°C for one hour, followed by cysteine alkylation in 55 mM iodoacetamide at room temperature for one hour in the dark. Samples were diluted 5X in 100 mM ammonium acetate to decrease the urea concentration prior to protein digestion, then samples were incubated with sequencing-grade modified trypsin (Promega, catalog # V5113) for 18 hours at a trypsin:protein ratio of 1:50 (w/w). Digestion was halted with 10% acetic acid, and samples were desalted by solid phase extraction using Sep-Pak C18 Plus Light cartridges (Waters, catalog # WAT023501) and eluted in 40% acetonitrile. All samples were concentrated in a vacuum centrifuge. Peptide concentration was quantified by bicinchoninic acid assay (Pierce), and 190 µg of peptide from each sample was freeze-dried by lyophilization. Samples were resuspended in 50 mM HEPES and labeled with TMTpro isobaric mass tags (Thermo Fisher Scientific, catalog # A52045) at a TMT:peptide ratio of 2.5:1 (w/w) for five hours at room temperature. Unreacted TMT was quenched with 3.2 µL of 5% hydroxylamine, then samples within each plex were pooled and dried by vacuum centrifugation.

Two-stage enrichment of tyrosine-phosphorylated peptides

TMT-labeled samples were resuspended in immunoprecipitation (IP) buffer (100 mM Tris-HCl, 1% NP-40, pH 7.4). For IP of tyrosine phosphorylated peptides, samples were incubated with 24 µg of anti-phosphotyrosine 4G10 antibody (BioXCell, catalog # BE0194) and 12 µg of anti-phosphotyrosine PT-66 antibody (Sigma-Aldrich, catalog # P3300) conjugated to protein G agarose beads (Sigma-Aldrich, catalog # IP04). Immunoprecipitation was carried out over 18-24 hours at 4°C. Peptides were eluted with 0.2% trifluoroacetic acid for 10 minutes and subjected to an additional phosphopeptide enrichment step using High-Select™ Fe-NTA spin columns (Thermo Fisher Scientific, catalog # A32992) to reduce the abundance of non-phosphorylated peptides which may have bound nonspecifically to the IP beads. Phosphopeptides were eluted

according to the manufacturer's instructions, dried by vacuum centrifugation, and resuspended in 5% acetonitrile in 0.1% formic acid.

Liquid chromatography and mass spectrometry

TMT-labeled phosphopeptides were loaded directly onto a chromatography column using a helium packing device in order to minimize sample loss. Columns were constructed in-house; fused silica capillary with inner diameter 50 μm and outer diameter 200 μm (Molex, catalog # 1068150017) was cut to a length of 25 cm and pulled using a micropipette laser puller to create an integrated emitter tip with 1-2 μm inner diameter, then was packed with 10 cm of 3 μm C18 beads (YMC Co, catalog # AM12S03) and conditioned and tested using a tryptic digest of bovine serum albumin. Liquid chromatography-tandem mass spectrometry was performed using an Agilent (1100-Series) chromatograph coupled to a Thermo Scientific™ Orbitrap Exploris™ 480 mass spectrometer. Peptides were separated using 0.2M acetic acid (solvent A) and 70% acetonitrile in 0.2M acetic acid (solvent B) over the following 140-minute gradient profile: (min:%B) 0:0, 10:11, 115:32, 125:60, 130:100, 133:100, 140:0. Electrospray ionization was carried out at 2.5 kV and at a flow rate of approximately 100 nL/min (200 μL/min through a flow splitter achieving a ~1:2000 split). The mass spectrometer was operated in data-dependent acquisition mode as follows: in each cycle, a full MS scan of precursor ions with m/z between 380-1800 was acquired with a resolution of 120,000 at 200 m/z and AGC target of 3e6, followed by a maximum of 20 MS/MS scans per cycle. For MS/MS scans, precursors with charge state between 2-5 were isolated with an isolation width of 0.4 Th and accumulated until the AGC target of 1e6 was reached, or until 247 ms had elapsed. Fragmentation was performed using a normalized collision energy of 33%, and fragment ions were scanned with a resolution of 120,000 at 200 m/z. For the targeted analysis, the mass spectrometer was restricted to selecting ions for MS/MS based on an inclusion list of mass-to-charge ratios of peptides of interest (see the text accompanying Figures 2.4A – 2.4C in Chapter 2 for details). The mass tolerance for the inclusion list was set to 5 parts per million (ppm). For untargeted analyses, each precursor was allowed to be selected for MS/MS four times before being dynamically excluded for 3 minutes.

Phosphopeptide identification and quantitation

Raw files containing phosphopeptide mass spectra were processed using Proteome Discoverer version 3.0 (Thermo Fisher Scientific) and searched using Mascot version 2.4 (Matrix Science). For the targeted analysis, spectra were searched against a custom database containing the phosphopeptide sequences that were specifically targeted for acquisition, with no enzymatic digestion, and with a precursor ion mass tolerance of 5 ppm. For the untargeted analyses, spectra were searched against the canonical human proteome (SwissProt reviewed sequences, version

2023_04) with trypsin digestion allowing for up to one missed cleavage, and with a precursor ion mass tolerance of 5 ppm. For both the targeted and untargeted analyses, MS/MS spectra were searched with a fragment ion mass tolerance of 20 mmu. Precursor ions and TMT reporter ions were removed from MS/MS spectra prior to searching using the non-fragment filter node in Proteome Discoverer. Cysteine carbamidomethylation, TMT-labeled lysine, and TMT-labeled peptide N-termini were set as static modifications; phosphorylation of tyrosine, serine, and threonine, and oxidation of methionine were set as dynamic modifications. Phosphorylation site localization was performed using ptmRS[4] within Proteome Discoverer. For peptide quantitation, TMT reporter ion intensities were extracted with an integration tolerance of 10 ppm and were isotope-corrected using Proteome Discoverer according to the manufacturer-provided batch-specific isotopic impurities of each TMT channel.

Peptide-spectrum matches (PSM) were exported from Proteome Discoverer and filtered by match quality (expectation value < 0.05) and phosphosite localization confidence (probability > 0.9 for all phosphosites on the peptide). Any PSM corresponding to a spectrum that matched to more than one amino acid sequence with equal expectation value was removed. For the targeted analysis, PSMs with more than 12 missing TMT values (out of 18 total channels) were discarded. For the untargeted analyses, PSMs with more than 6 missing TMT values (out of 12 total channels) were discarded. All remaining PSMs were subjected to replacement of missing TMT reporter ion intensities with a value equivalent to half the intensity of the least-intense fragment ion observed in the corresponding MS/MS spectrum (see the text accompanying Figure 2.10B in Chapter 2 for details). TMT reporter ion intensities were then summed across PSMs sharing a common modified peptide sequence. To correct for technical variation in the total amount of peptide labeled in each TMT channel, peptide from the phosphotyrosine IP supernatant (approximately 50 ng) was analyzed by mass spectrometry according to the procedure above, and the resulting data – containing quantitative information for peptides derived from the most abundant proteins in the cell, assumed on average to be biologically invariant – were used to derive a correction factor for each TMT channel. Phosphopeptides derived from the same source protein(s) with shared phosphorylation site pattern (for example, two phosphopeptides covering the same phosphosite but with different tryptic cleavage pattern) were aggregated to eliminate phosphosite redundancy in the resulting data matrix.

Data visualization

Results were visualized using the matplotlib and seaborn python packages. The schematics depicted in Figures 2.4A, 2.6A, 2.6B, 2.8B, and 2.10A were created using BioRender.

References

1. Tsherniak A., Vazquez F., Montgomery P.G., Weir B.A., Kryukov G., Cowley G.S., Gill S., Harrington W.F., Pantel S., Krill-Burger J.M., et al. (2017). Defining a Cancer Dependency Map. Cell *170*, 564-576.e16.
2. Virtanen P., Gommers R., Oliphant T.E., Haberland M., Reddy T., Cournapeau D., Burovski E., Peterson P., Weckesser W., Bright J., et al. (2020). SciPy 1.0: fundamental algorithms for scientific computing in Python. Nat Methods *17*, 261-272.
3. Greco W.R., Bravo G., Parsons J.C. (1995). The search for synergy: a critical review from a response surface perspective. Pharmacol Rev *47*, 331-85.
4. Taus T., Köcher T., Pichler P., Paschke C., Schmidt A., Henrich C., Mechtler K. (2011). Universal and confident phosphorylation site localization using phosphoRS. J Proteome Res *10*, 5354-62.

Appendix B:
Methods for chapter 3

Cell lines and drug treatment

M-series patient-derived cell lines were generated under UCLA institutional review board approval # 11–003254 and transferred to Institute for Systems Biology under established materials transfer agreement (MTA). Cells were cultured in a water-saturated incubator at 37 °C with 5% CO_2 in RPMI-1640 containing L-glutamine (Gibco, catalog # 11875093) supplemented with 10% fetal bovine serum (ATCC) and 0.2% MycoZap Plus-CL antibiotics (Lonza, catalog # 195261). Cell lines were routinely tested for mycoplasma and were periodically authenticated to its early passage using the GenePrint 10 System (Promega, catalog # B9510). VEM and DAS (Selleck Chemicals, catalog #s S1267 and 1021, respectively) were dissolved in DMSO at designated concentrations before applying to cell culture media at a final DMSO concentration of 0.1% (v/v). Control cells were treated with 0.1% DMSO. NAC (Sigma-Aldrich, catalog # A7250) was dissolved in phosphate-buffered saline. For phosphoproteomics and RNA-seq experiments, M397 cells were grown in 10 cm tissue culture plates, plated at 60% confluency, and treated for the specified amount of time before being harvested from culture.

Cell viability dose-response assay

M397 cells were seeded in a 96-well plate (3000 cells/well) in triplicate and incubated for 24 hours, followed by treatment with VEM in 0.1% DMSO at the designated doses for 72 hours. Cell viability was then quantified using CellTiter-Glo (Promega, catalog # G7572) according to the manufacturer protocol. All luminescence values were normalized to the average of the three drug-free control wells. Conventional monophasic dose-response models achieved poor fit to the data due to the clear biphasic nature of the M397 response to VEM; therefore, the following modified viability model was derived to accommodate the biphasic dose response:

$$V(d) = (1-\alpha)\left(\frac{1}{1+\left(\frac{d}{EC_{50,1}}\right)^{n_1}}\right) + \alpha\left(\frac{1}{1+\left(\frac{d}{EC_{50,2}}\right)^{n_2}}\right)$$

where $V(d) \in [0,1]$ is the fraction of viable cells under dose d (in nM). Under this model specification, once fitted to the data, $EC_{50,1}$ and $EC_{50,2}$ are estimates of the doses at which there is a half-maximal effect for the first and second dose-response phases, respectively. Similarly, n_1 and n_2 are measures of the steepness of the first and second dose-response phases, respectively. α

provides an estimate of the intermediate viability of cells treated with doses between $EC_{50,1}$ and $EC_{50,2}$. Model fitting was performed using the curve_fit function in the SciPy scientific computing python package.[1]

Dead cell quantitation and time-resolved viability assay

M397 cells were seeded in 6 cm plates (0.2M/plate), incubated for 24 hours, and treated with 0, 3, or 100 μM VEM in 0.1% DMSO for 72 hours. Six biological replicates were seeded per condition. 100 μM VEM was used as a positive control for cell death. Media was collected from each plate, and cells adhered to the plate were trypsinized and added to the collected media. Cells were pelleted, resuspended in PBS, and stained with trypan blue. Dead (trypan blue-positive) and live (negative) cells were quantified using a hemocytometer. For quantifying cell viability kinetics, M397 cells were plated onto six-well plates (0.1M/well), incubated for 24 hours, and treated with 3 μM VEM or 0.1% DMSO. Three biological replicates were seeded per condition. Cell viability was monitored by an Incucyte S3 Live-Cell Analysis System (Sartorius). Phase contrast images were taken every six hours throughout a 72-hour period. Cell numbers were quantified using Incucyte classic confluence analysis workflow.

Phosphoproteomics sample preparation

M397 cells were lysed in 8M urea and total protein was quantified by bicinchoninic acid assay (Pierce, catalog # 23225). For each sample, 700 μg of protein was subjected to reduction in 10 mM dithiothreitol at 56°C for one hour, followed by cysteine alkylation in 55 mM iodoacetamide at room temperature for one hour in the dark. Samples were diluted 5X in 100 mM ammonium acetate to decrease the urea concentration prior to protein digestion, then samples were incubated with sequencing-grade modified trypsin (Promega, catalog # V5113) for 18 hours at a trypsin:protein ratio of 1:50 (w/w). Digestion was halted with 10% acetic acid, and samples were desalted by solid phase extraction using Sep-Pak C18 Plus Light cartridges (Waters, catalog # WAT023501) and eluted in 40% acetonitrile. All samples were concentrated in a vacuum centrifuge. Peptide concentration was quantified by bicinchoninic acid assay (Pierce), and 120 μg of peptide from each sample was freeze-dried by lyophilization. Samples were resuspended in 50 mM HEPES and labeled with TMTpro isobaric mass tags (Thermo Fisher Scientific, catalog # A52045) at a TMT:peptide ratio of 4:1 (w/w) for five hours at room temperature. Unreacted TMT was quenched with 3.2 μL of 5% hydroxylamine, then samples within each plex were pooled and dried by vacuum centrifugation.

Phospho-motif immunoprecipitation and phosphopeptide enrichment

TMT-labeled samples were resuspended in immunoprecipitation (IP) buffer (100 mM Tris-HCl, 1% NP-40, pH 7.4). For IP of tyrosine phosphorylated peptides, samples were incubated with 24 µg of anti-phosphotyrosine 4G10 antibody (BioXCell, catalog # BE0194) and 12 µg of anti-phosphotyrosine PT-66 antibody (Sigma-Aldrich, catalog # P3300) conjugated to protein G agarose beads (Sigma-Aldrich, catalog # IP04). For IP of phosphopeptides containing the (pS/pT)Q and (pS/pT)P phospho-motifs, supernatant from the phosphotyrosine IP was incubated with 40 µL of anti-(pS/pT)Q and anti-(pS/pT)P antibody pre-conjugated to agarose beads (Cell Signaling Technologies, catalog #s 12267 and 14378S, respectively). Immunoprecipitation was carried out over 18-24 hours at 4°C. Peptides were eluted with 0.2% trifluoroacetic acid for 10 minutes and subjected to an additional phosphopeptide enrichment step using High-Select™ Fe-NTA spin columns (Thermo Fisher Scientific, catalog # A32992) to reduce the abundance of non-phosphorylated peptides which may have bound nonspecifically to the IP beads. For phosphoserine/threonine enrichment (with no phospho-motif enrichment), 2 µL of peptide from the IP supernatant was diluted in 50 µL of 0.2% trifluoroacetic acid and transferred to an Fe-NTA spin column. All phosphopeptide samples were eluted according to the manufacturer's instructions, dried by vacuum centrifugation, and resuspended in 5% acetonitrile in 0.1% formic acid.

Liquid chromatography and mass spectrometry

Each phosphopeptide mixture corresponding to a single TMT plex was loaded directly onto a chromatography column using a helium packing device in order to minimize sample loss. Columns were constructed in-house; fused silica capillary with inner diameter 50 µm and outer diameter 200 µm (Molex, catalog # 1068150017) was cut to a length of 25 cm and pulled using a micropipette laser puller to create an integrated emitter tip with 1-2 µm inner diameter, then was packed with 10 cm of 5 µm C18 beads (YMC Co, catalog # AQ12S05) and conditioned and tested using a tryptic digest of bovine serum albumin. Liquid chromatography-tandem mass spectrometry was performed using an Agilent (1100-Series) chromatograph coupled to a Thermo Scientific™ Orbitrap Exploris™ 480 mass spectrometer. Peptides were separated using 0.2M acetic acid (solvent A) and 70% acetonitrile in 0.2M acetic acid (solvent B) over the following 140-minute gradient profile: (min:%B) 0:0, 10:11, 115:32, 125:60, 130:100, 133:100, 140:0. Electrospray ionization was carried out at 2.5 kV and at a flow rate of approximately 100 nL/min (200 µL/min through a flow splitter achieving a ~1:2000 split). For the time-resolved phosphoproteomics experiment, the mass spectrometer was operated in data-dependent acquisition mode as follows: in each cycle, a full MS scan of precursor ions with m/z between 380-2000 was acquired with a resolution of 60,000 at 200 m/z and AGC target of 3e6, followed by a series of MS/MS scans for

a total cycle duration of 3 s. For MS/MS scans, precursors with charge state between 2-6 and intensity greater than 1e4 were isolated with an isolation width of 0.4 Th and accumulated until the AGC target of 1e5 was reached, or until 250 ms had elapsed. Fragmentation was performed using a normalized collision energy of 33%, and fragment ions were scanned with a resolution of 60,000 at 200 m/z. Each precursor was allowed to be selected for MS/MS twice before being dynamically excluded for 45 s. For the targeted phosphoproteomics experiment, the mass spectrometer was restricted to selecting ions for MS/MS based on an inclusion list of mass-to-charge ratios of peptides of interest from the time-resolved phosphoproteomics data (Supplementary Table S4). The mass tolerance for the inclusion list was set to 3 parts per million (ppm). Given the relatively limited set of monitored phosphopeptide targets, the acquisition sensitivity was boosted by increasing the resolution (full MS and MS/MS) to 120,000, increasing the AGC target for MS/MS to 1e6, and disabling the intensity threshold and dynamic exclusion.

Phosphopeptide identification and quantitation

Raw files containing phosphopeptide mass spectra were processed using Proteome Discoverer version 3.0 (Thermo Fisher Scientific) and searched using Mascot version 2.4 (Matrix Science). For the time-resolved phosphoproteome experiment, spectra were searched against the canonical human proteome (SwissProt reviewed sequences, version 2023_01) with trypsin digestion allowing for up to one missed cleavage, and with a precursor ion mass tolerance of 5 ppm. For the targeted phosphoproteomics experiment, spectra were searched against a custom database containing the phosphopeptide sequences that were specifically targeted for acquisition, with no enzymatic digestion, and with a precursor ion mass tolerance of 3 ppm. For both phosphoproteomics experiments, MS/MS spectra were searched with a fragment ion mass tolerance of 20 mmu. Precursor ions and TMT reporter ions were removed from MS/MS spectra prior to searching using the non-fragment filter node in Proteome Discoverer. Cysteine carbamidomethylation, TMT-labeled lysine, and TMT-labeled peptide N-termini were set as static modifications; phosphorylation of tyrosine, serine, and threonine, and oxidation of methionine were set as dynamic modifications. Phosphorylation site localization was performed using ptmRS[2] within Proteome Discoverer. For peptide quantitation, TMT reporter ion intensities were extracted with an integration tolerance of 10 ppm and were isotope-corrected using Proteome Discoverer according to the manufacturer-provided batch-specific isotopic impurities of each TMT channel.

Peptide-spectrum matches (PSM) were exported from Proteome Discoverer and filtered by match quality (expectation value < 0.05) and phosphosite localization confidence (probability > 0.9 for all phosphosites on the peptide). Any PSM corresponding to a spectrum that matched to more than one amino acid sequence with equal expectation value was removed. PSMs with more than four missing TMT values were discarded. For the remaining PSMs, missing TMT reporter

ion intensities were replaced with a value equivalent to half the intensity of the least-intense fragment ion observed in the corresponding MS/MS spectrum; this approach assumes that an absent reporter ion would have been detected and recorded into the raw file had its intensity been greater than the least-intense fragment in the spectrum. Under this assumption, the intensity of the absent reporter lies between zero ("true absence") and the intensity of the minimal fragment, with uniform probability. TMT reporter ion intensities were then summed across PSMs sharing a common modified peptide sequence. Phosphopeptides derived from the same source protein(s) with shared phosphorylation site pattern (for example, two phosphopeptides covering the same phosphosite but with different tryptic cleavage pattern) were aggregated to eliminate phosphosite redundancy in the resulting data matrix.

RNA-seq

M397 cell pellets were snap frozen at the designated timepoints after treatment with 3 μM VEM or 0.1% DMSO. Total RNA was extracted from cell pellets using AllPrep DNA/RNA kit (Qiagen, catalog # 80204). The mRNA library was constructed with TruSeq RNA Sample Preparation Kit (Illumina, catalog # RS-122-2001) and sequenced on an Illumina HiSeq 2500 System with paired-end 150-base-pair reads following the manufacturer's recommendations by Novogene.

Immunoblotting

Antibodies against phospho-SRC (Y416), total SRC, and GAPDH (Cell Signaling Technology, catalog #s 2101S, 2109T, and 5174S, respectively) were used. The Invitrogen precast gel system NuPAGE was used for running the western blot. The 4–12% Bis-Tris gels were loaded with samples. After blotting, the membranes were blocked in 5% BSA with TBS + 0.1% Tween-20 (TBST) mix for at least one hour at room temperature. Membranes were then incubated overnight with the primary antibody in 5% BSA with TBST at 4°C. The next day, membranes were washed three times for five minutes in TBST, incubated with a suitable HRP-coupled secondary antibody for one hour at room temperature, and washed three times. Proteins were visualized with SuperSignal™ West Pico PLUS Chemiluminescent Substrate (Thermo Fisher Scientific, catalog # 34577) using the ChemiDoc™ XRS+ System.

Clonogenic assay

Cells were seeded onto six-well plates at an optimal seeding density determined from each cell line's specific growth rate. For the VEM plus DAS experiment (Figure 3.11A), cells were treated with VEM monotherapy or VEM plus 50 nM DAS for the same amount of time. The dose of VEM used was 2-fold the cell line-specific EC_{50} which was previously determined.[3] The media

(with drug or DMSO) was replenished every two days. For the combinatorial treatment, the treatment was stopped followed by staining when the VEM-treated cells displayed clear regrowth. For the toxicity assessment (Figure 3.11B), cells were treated with 50 nM DAS or DMSO and the treatment was stopped followed by staining after five days. Upon the time of staining, 4% paraformaldehyde was applied onto colonies to fix the cells and 0.05% crystal violet solution was used for staining the colonies. ColonyArea, an ImageJ plugin, was used to perform standard analysis of colony formation assays.

ROS production assay

M397 cells were split into six groups and treated as follows: 0.1% DMSO; 3 μM VEM; 3 μM VEM plus 10 mM NAC; 30 μM H_2O_2; 30 μM H_2O_2 plus 10 mM NAC; 0.1% DMSO plus 10mM NAC. All treatments were given for three days except NAC, which was given one hour prior to ROS quantitation. ROS levels were quantified by ROS-Glo™ H_2O_2 Assay (Promega, catalog # G8820) according to the manufacturer's protocol. The luminescence signals were measured by the Synergy H4 Plate Reader.

Melanoma mouse xenograft experiments

Mice were maintained in a specific pathogen-free (SPF), temperature-controlled (21-23°C) animal facility on a reverse 12-hour light, 12-hour dark cycle at the University of Washington. Food and water were given ad libitum. Mice were kept under animal bio-safety level (ABSL-2) conditions and handled under protocols approved by the Institutional Animal Care and Use Committee (IACUC) of the University of Washington (PROTO201900025) in accordance with international guidelines. To generate xenograft mouse tumor models, 6 to 7-week-old NOD. Cg-Prkdc^{scid} Il2rg^{tm1Wjl}/SzJ (NSG) female mice were purchased from the Jackson Laboratory (catalog # 005557). NSG mice were inoculated with M397 cells (10^6 cells per mouse) in Matrigel mixture (Corning, catalog # 354234) via a subcutaneous injection into the right flank. When the average tumor volume reached ~200 mm^3, the mice were randomized into four groups: control, 100 mg/kg VEM, 30 mg/kg DAS, and 100 mg/kg VEM plus 30 mg/kg DAS, with five mice per group. VEM and DAS were formulated as 5% DMSO in 0.5% methyl cellulose and given once daily by oral gavage. Tumor length and width were measured once every three days using calipers. Tumor volume was calculated using the equation Volume (mm^3) = Length (mm) × Width (mm^2) / 2. Mice were euthanized and tumors were excised at day 27, except for the mice in the control group that were sacrificed earlier when the average tumor volume reached 1500 mm^3.

Statistical analysis software

Statistical testing, principal components analysis, and hierarchical clustering of the phosphoproteomics data was performed using the SciPy, scikit-learn, and seaborn python packages. For principal components analysis (Figure 3.1E) and pairwise sample correlation analysis (Figure 3.2C), phosphopeptide abundance values were mean-normalized.

RNA-seq analysis

Reads were aligned against the human genome (hg19) using STAR (v2.7.3a). Read counts were quantified using htseq-count[4] with known gene annotations from UCSC.[5] Transcript level was calculated as fragments per kilobase of transcript per million mapped reads (FPKM). Transcript levels (FPKM+1) were centralized and scaled prior to principal components analysis (Figure 3.3A) using scikit-learn. Gene-set enrichment analysis (GSEA) was conducted using GSEA v4.1.0 software with 1000 permutations and weighted enrichment statistics. Normalized enrichment score was computed across the curated Molecular Signatures Database (MSigDB) Hallmark, C2, and C5 GO:BP gene sets.

Transcription factory regulatory network analysis

The NetAct[6] R package was used for constructing the TF regulatory network using time-series transcriptome data, depicted in Figure 3.4. Specifically, each RNA-seq sample was randomly downsampled to 3 replicates by seqtk. Each replicate recapitulates 50% of the original RNA-seq reads. Read counts quantified by htseq-count were used as the input for NetAct to construct core TF regulatory networks using inferred gene activities. NetAct uniquely integrates both generic TF-target relationships from literature-based databases and context-specific gene expression data to construct an optimized TF-target gene set database. NetAct takes the following steps to construct TF networks from raw read counts: (1) A pre-processing function called preprocess_counts() was used to filter out lowly expressed genes and retrieve associated gene symbols for raw count data. (2) Pairwise comparisons were defined to extract differentially expressed genes at each time point over the 3-day drug treatment procedure, resulting in a total of 15 group comparisons across six time points: control, and post-drug treatment at 12h, 24h, 36h, 48h, and 72h. Differentially expressed genes are subsequently identified using the limma package[7] with q-value ≤ 0.05. The resulting normalized expression data is saved alongside the phenoData metadata into the standard ExpressionSet object for downstream analysis. (3) A permutation approach was adopted to select TFs with significantly altered activities across the drug treatment by using the gene set enrichment analysis against literature-based TF-target databases. The TFs are aggregated from the multiple comparisons with q-value ≤ 0.01. The activities of enriched TFs were further calculated from the standardized expression levels of their target genes with weighting

factors defined as a Hill function. (4) The TF regulatory networks were constructed by using both the TF-TF regulatory interactions from the TF-target database and the activity values. The link interactions were filtered out based on mutual information and entropy. The plot_network() function was used to interact with the network topology.

Regulatory module inference

The signaling and transcriptional module inference depicted in Figure 3.5 was performed as follows: TMT intensity values were averaged across the three replicates for each phosphosite in the time-series phosphoproteomic data, and the DMSO control samples were dropped. Data were z-score normalized (phosphosite-wise) and a pairwise Pearson correlation matrix was computed. Euclidean distances were calculated between each pair of phosphosites and used for hierarchical clustering, which was applied to the correlation matrix. A threshold on the cophenetic distance proportional to the total number of phosphosites was applied to the dendrograms, resulting in discrete clusters of phosphosites. The gene IDs within each cluster were queried for over- and under-representation of gene sets using Fisher's exact test and the following libraries of gene sets downloaded from MSigDB (all version 2023_1): BioCarta, GObp, GOcc, GOmf, Hallmarks, KEGG, PID, Reactome, TFT, WikiPathways. P-values were corrected for multiple hypotheses by the Benjamini-Hochberg procedure. These steps were also applied to the RNA-seq data, after transcripts where quantitation (FPKM) was 0 in any sample were filtered out. For each module, the consensus dynamics were calculated as the mean z-score-normalized abundance across all members of the module. Consensus dynamics were then used to calculate meta-correlations between every pair of inferred signaling and transcriptional modules, as depicted in Figure 3.5C. P-values for meta-correlation were determined based on how frequently two randomly-sampled multivariate normally-distributed random variables achieve a Pearson correlation coefficient at least as extreme as the observed meta-correlation, followed by multiple hypothesis correction by the Benjamini-Hochberg procedure.

Data visualization

Results were visualized using the following python packages: matplotlib, seaborn, holoviews. The schematics depicted in Figures 3.1C, 3.9D, and 3.11E were created using BioRender.

References

1. Virtanen P., Gommers R., Oliphant T.E., Haberland M., Reddy T., Cournapeau D., Burovski E., Peterson P., Weckesser W., Bright J., et al. (2020). SciPy 1.0: fundamental algorithms for scientific computing in Python. Nat Methods *17*, 261-272.
2. Taus T., Köcher T., Pichler P., Paschke C., Schmidt A., Henrich C., Mechtler K. (2011). Universal and confident phosphorylation site localization using phosphoRS. J Proteome Res *10*, 5354-62.
3. Su Y., Wei W., Robert L., Xue M., Tsoi J., Garcia-Diaz A., Homet Moreno B., Kim J., Ng R.H., Lee J.W., et al. (2017). Single-cell analysis resolves the cell state transition and signaling dynamics associated with melanoma drug-induced resistance. Proc Natl Acad Sci U S A *114*, 13679-13684.
4. Anders S., Pyl P.T., Huber W. (2015). HTSeq--a Python framework to work with high-throughput sequencing data. Bioinformatics *31*, 166-9.
5. Nassar L.R., Barber G.P., Benet-Pagès A., Casper J., Clawson H., Diekhans M., Fischer C., Gonzalez J.N., Hinrichs A.S., Lee B.T., et al. (2023). The UCSC Genome Browser database: 2023 update. Nucleic Acids Res *51*, D1188-D1195.
6. Su K., Katebi A., Kohar V., Clauss B., Gordin D., Qin Z.S., Karuturi R.K.M., Li S., Lu M. (2022). NetAct: a computational platform to construct core transcription factor regulatory networks using gene activity. Genome Biol *23*, 270.
7. Ritchie M.E., Phipson B., Wu D., Hu Y., Law C.W., Shi W., Smyth G.K. (2015). limma powers differential expression analyses for RNA-sequencing and microarray studies. Nucleic Acids Res *43*, e47.